PHILOSOPHICAL MAGAZINE

eBook: Landmark materials science articles

Taylor & Francis
by informa

eBook

Landmark materials science articles

Contents:

Taylor & Francis
by informa

Philosophical Magazine

ISSN: 1478-6435 (Print) 1478-6443 (Online) Journal homepage: www.tandfonline.com/journals/tphm20

The mechanical efficiency of natural materials

U. G. K. Wegst & M. F. Ashby

To cite this article: U. G. K. Wegst & M. F. Ashby (2004) The mechanical efficiency of natural materials, Philosophical Magazine, 84:21, 2167-2186, DOI: 10.1080/14786430410001680935

To link to this article: https://doi.org/10.1080/14786430410001680935

PHILOSOPHICAL MAGAZINE, 21 July 2004
VOL. 84, NO. 21, 2167–2181

Taylor & Francis
Taylor & Francis Group

The mechanical efficiency of natural materials

U. G. K. WEGST

Max-Planck-Institut für Metallforschung, Heisenbergstrasse 3,
D-70569, Stuttgart, Germany

and M. F. ASHBY†

Engineering Design Centre, Engineering Department, University of Cambridge,
Trumpington Street, Cambridge CB2 1PZ, UK

[*Received 26 November 2003 and accepted in revised form 17 February 2004*]

ABSTRACT

The materials of nature, for example cellulose, lignin, keratin, chitin, collagen and hydroxyapatite, and the structures made from them, for example bamboo, wood, antler and bone, have a remarkable range of mechanical properties. These can be compared by presenting them as *material property charts*, well known for the materials of engineering. Material indices (significant combinations of properties) can be plotted on to the charts, identifying materials with extreme values of an index, suggesting that they have evolved to carry particular modes of loading, or to sustain large tensile or flexural deformations, without failure. This paper describes a major revision and update of a set of property charts for natural material published some 8 years ago by Ashby *et al*. with examples of their use to study mechanical efficiency in nature.

§ 1. INTRODUCTION

Natural materials are remarkably efficient. By efficient we mean that they fulfil the complex requirements posed by the way that plants and animals function and that they do so using as little material as possible‡. Many of these requirements are mechanical in nature: the need to support static and dynamic loads created by the mass of the organism or by wind loading, the need to store and release elastic energy, the need to flex through large angles, and the need to resist buckling and fracture. Most natural materials are sustainable, recyclable and, when disposal is necessary, biodegradable, making them a model for environmentally conscious engineering.

Virtually all natural materials are composites (Wainwright *et al*. 1976, Vincent and Currey 1980, Vincent 1990, Thompson 1992, Sarikaya and Aksay 1995, Wegst 1996, Bappert *et al*. 1998, Beukers and Van Hinte 1998). They consist of a relatively small number of polymeric and ceramic components or building blocks, which often are composites themselves. Plant cell walls, for instance, are composites of cellulose, hemicellulose, pectin and protein and can be lignified; animal tissues consist largely

† Author for correspondence. Email: mfaz@eng.cam.ac.uk.

‡ 'As a general principle natural selection is continually trying to economise every part of the organisation', according to Charles Darwin, writing over 100 years ago.

Philosophical Magazine ISSN 1478–6435 print/ISSN 1478–6443 online
http://www.tandf.co.uk/journals
DOI: 10.1080/14786430410001680935

of collagen, elastin, keratin, chitin and minerals such as salts of calcium or silica. From these limited 'ingredients', nature fabricates a remarkable range of structured composites. Wood, bamboo and palm consist of cellulose fibres in a lignin–hemicellulose matrix, shaped to hollow prismatic cells of varying wall thickness. Hair, nail, horn, wool, reptilian scales and hooves are made of keratin while insect cuticle contains chitin in a matrix of protein. The dominant ingredient of mollusc shell is calcium carbonate, bonded with a few per cent of protein. Dentine and enamel are composed mainly of hydroxyapatite. Bone and antler are formed of hydroxyapatite and collagen. Collagen is the basic structural element for soft and hard tissues in animals, such as tendon, ligament, skin, blood vessels, muscle and cartilage; even the cornea is collagen.

From a mechanical point of view, there is nothing very special about the individual building blocks. Cellulose fibres have Young's moduli that are about the same as that of nylon fishing-line, but much less than steel, and the lignin–hemicellulose matrix that they are embedded in has properties very similar to that of epoxy resin. Hydroxyapatite has a fracture toughness comparable with that of man-made ceramics. It is thus the *structure* and *arrangement* of the components that give rise to the striking efficiency of natural materials.

§ 2. Microstructure and mechanical performance of natural materials

How large the effect of the structure can be on the mechanical performance of a material is best illustrated by taking tendon, ligament, skin, cartilage and bone as examples. All share the same main polymeric components, collagen and elastin, but the fractions and structure of each component in the material vary distinctly.

Tendon and ligament are both designed to transmit tensile forces. The distinction is morphological; tendons operate in functional units 'bone–tendon–muscle–tendon–bone' to transmit forces from muscles to bones in order to move the bones, while ligament operates in the functional unit 'bone–ligament–bone', joining bones together to form joints and to restrict movement and prevent dislocation. Both are made up of roughly parallel collagen fibres aligned to form rope-like structures, but there are important differences. Tendon contains 60–86% dry weight of collagen and less than 5% dry weight of elastin which allows it to transmit tensile forces with minimal energy loss and little stretching; strains seldom exceed 10%. Ligament, with a lower (50–70% dry weight) collagen content, has a lower stiffness. At the same time its higher elastin content (10–20% dry weight) allows it almost to double its length before it fails; strains of up to 80% are typical. The structure, too, is important. Tendon has an ordered fibre alignment while that of ligament is less regular, sometimes curved and often laid at an oblique angle to the length of the tendon to cope with off-axis loads.

Skin has a similar composition to tendon, it contains about 70–80% dry weight of collagen and about 4% dry weight of elastin but has a significantly more complex structure. The collagen fibrils, sandwiched between a basement membrane and an overlaying epidermis, are woven into a more or less rhombic parallelogram pattern forming a three-dimensional fish-net-like network in which the predominant fibre direction is parallel to the surface. The structure, in which the collagen fibres are wavy and unaligned, allows considerable, if anisotropic, deformation in all directions without requiring elongation of the individual fibres; this is particularly important in the regions of joints where the skin is required to stretch.

Cartilage has a structure that is yet more complex. Hyaline cartilage, found on joint surfaces and at the end of ribs, for example, has three layers. The superficial layer contains up to 90% dry weight of collagen fibres which are arranged in a network parallel to the surface. The middle layer has a lower collagen content of 60% dry weight, and the collagen fibres are arranged at an angle of about 45° with respect to a line normal to the cartilage surface; in the third layer, which joins cartilage and bone, the collagen fibrils are oriented perpendicular to the bone surface. At sites where flexibility and shape recovery are of prime importance (the tip of the nose for instance), elastic cartilage is found; it has a lower collagen content (53% of dry weight) and a high elastin content (20% of dry weight).

Finally, compact bone might be regarded as calcified cartilage. It is a composite consisting of collagen fibres (20–30% dry weight), about 1% dry weight of other proteinaceous material bonding about 70% of calcium phosphate in the form of hydroxyapatite which provides stiffness and strength.

§ 3. Materials property charts

Figure 1 illustrates, schematically, the idea of a material property chart (Ashby 1999). It shows one material property, in this case Young's modulus E plotted against another, the density ρ. Logarithmic scales allow the accommodation of materials from the lowest to the highest moduli and densities. Different classes of

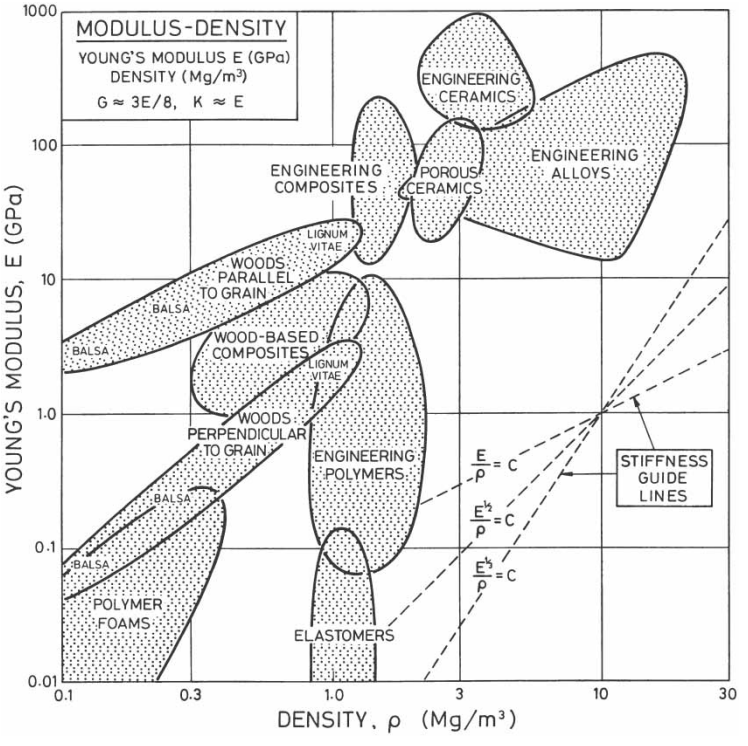

Figure 1. An example of a material property chart for engineering materials showing Young's modulus plotted against density. Guidelines show the slopes of three material indices. Their use is explained in the text.

materials (metals, polymers, ceramics, composites and natural materials) cluster; each envelope encloses all members of the material class it represents.

Individual materials (not shown in figure 1) appear as small bubbles within the characteristic field of their class. The bubble width reflects the range of the property, determined by composition and microstructure. In the case of engineering materials, these features are controlled by the manufacturing process. In the case of natural materials, it is the growth conditions and age that determine the structure. Just as the degree of crystallinity and cross-linking influence the properties of one particular polymer, the climate, the quality of the soil and the altitude determine the growth of one particular species of wood. A similar argument holds for the materials found in animals.

Property charts become more useful when combined with material indices, which measure the efficiency of a material in a given application. As an example, the efficiency of materials as a stiff tie (tensile members) is measured by the index E/ρ; the larger the value of E/ρ, the lighter is the tie for the same stiffness. The performance of a light stiff beam (a component loaded in bending) is measured not by E/ρ but by the index $E^{1/2}/\rho$. That for flat plates loaded in bending is $E^{1/3}/\rho$. The logarithmic scales allow all three to be plotted in figure 1; each appears as a set of straight parallel lines. One member of each is shown on the figure, labelled STIFFNESS GUIDE LINES; the required set can be constructed from these. One class of natural material, namely woods, appear on this chart. The guidelines show that the value of E/ρ for woods is almost the same as that for steel, but that their values of $E^{1/2}/\rho$ and $E^{1/3}/\rho$ are much larger; that is, they are more efficient (lighter for the same stiffness) than steel when used as light stiff beams or plates. There are many material indices, each measuring some aspect of efficiency in a given mode of loading.

Like engineering materials, natural materials can be grouped into classes. *Natural ceramics* and *ceramic composites* include bone, antler, enamel, dentine, shell and coral. All are made up of ceramic particles such as hydroxyapatite, calcite or aragonite in a matrix of collagen; all have densities between 1.8 and 3.0 $\mathrm{Mg\,m^{-3}}$. Their moduli are lower than those of engineering ceramics, but their tensile strengths are roughly the same and their toughnesses are greater, by a factor of ten or so.

Natural polymers and *polymer composites* include cellulose and chitin (polysaccharides) and collagen, silk and keratin (proteins). All have densities of around 1.2 $\mathrm{Mg\,m^{-3}}$. Their moduli and tensile strengths are larger than those of engineering polymers: cellulose fibrils, for instance, have moduli of about 50–130 GPa and a strength of 1 GPa, whilst silks have moduli of 2–20 GPa and strengths of 0.3–2 GPa. Of man-made polymers only Kevlar fibre has a higher stiffness (200 GPa) and strength (up to 4 GPa) which it achieves, as do natural fibres, through its highly oriented molecular structure and covalent bonding.

Natural elastomers such as elastin, resilin, abductin, skin, artery and cartilage all have densities of about 1.15 $\mathrm{Mg\,m^{-3}}$. Their moduli and densities are similar to those of engineering elastomers.

Natural cellular materials such as wood, cork, palm, bamboo and cancellous bone, all have low densities ($\rho = 0.1$–$1.2\,\mathrm{Mg\,m^{-3}}$) because of the high volume fractions of voids that they contain. They are almost always anisotropic because of the shape and orientation of the fibres that they contain and because of the shape of the cells themselves; prismatic cells of wood, for instance, give a much greater stiffness and strength along the grain than across it.

We next describe the selection charts which allow useful relationships between material properties to be explored. There are four basic charts: modulus–density, strength–density, modulus–strength and toughness–modulus. The data sources are described in appendix A and listed after the references.

3.1. *The Young's modulus–density chart*

Figure 2 shows data for Young's modulus E and density ρ. Those for the classes of natural materials are circumscribed by a heavy balloon; class members are shown as smaller bubbles within them. Three stiffness guidelines are shown, each representing the material index for a particular mode of loading. They are

$$M_1 = \frac{E}{\rho} \quad \text{(tie in tension)},$$

$$M_2 = \frac{E^{1/2}}{\rho} \quad \text{(beam in flexure)},$$

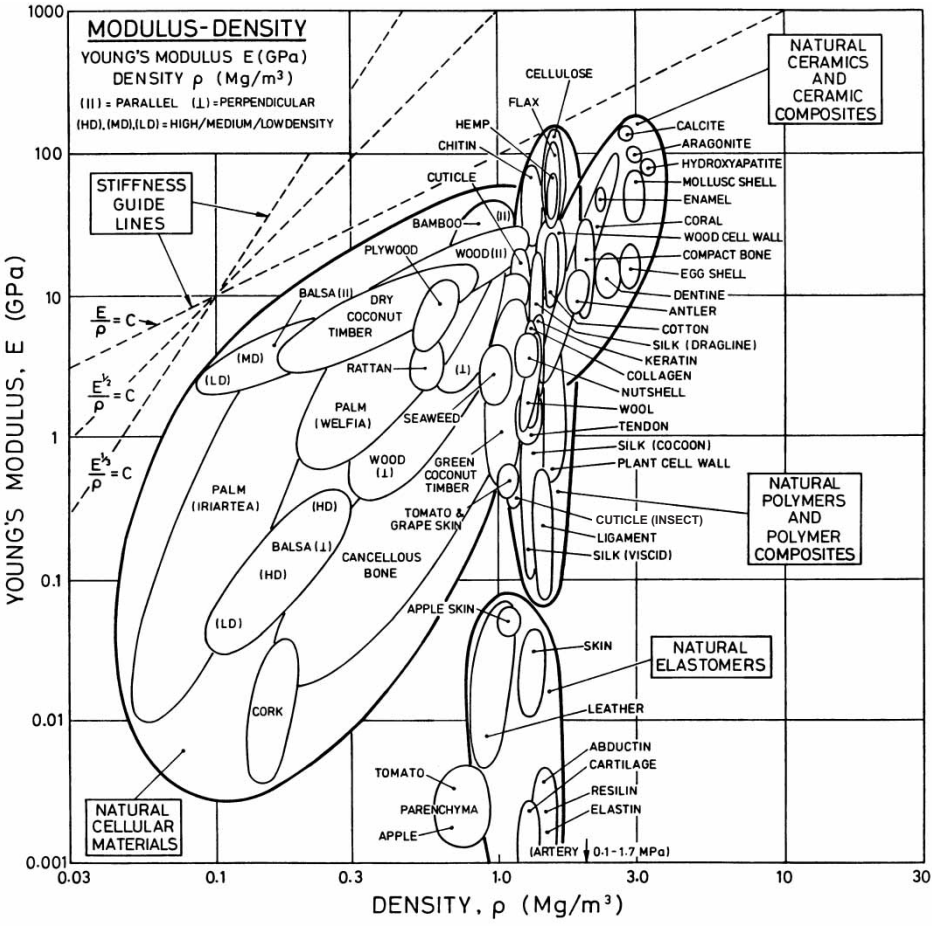

Figure 2. A material property chart for natural materials, plotting Young's modulus against density. Guidelines identify structurally efficient materials that are light and stiff.

$$M_3 = \frac{E^{1/3}}{\rho} \quad \text{(plate in flexure).}$$

The natural polymer with the highest efficiency in tension, measured by the index E/ρ, is cellulose; it exceeds that of steel by a factor of about 2.6. The high values for the fibres flax, hemp and cotton derive from this. Wood, palm and bamboo are particularly efficient in bending and resistant to buckling, as indicated by the high values of the flexure index $E^{1/2}/\rho$ when loaded parallel to the grain; that for Balsa wood, for example, can be five times greater than that of steel.

This is not surprising; the principal loads that they must carry in performing their natural function are bending (branches under their own weight and snow, and trunks under wind loads) and axial compression leading to buckling (of the trunk under its own weight and snow loads). Palm is slightly more efficient than most woods, allowing palms to grow to great heights while remaining slender. Bamboo wood is even more efficient, because the fibres that it contains are particularly well oriented along the stem, and in the plant the efficiency is increased further (as in most grasses) by the tubular shape and a gradient of modulus across the wall thickness.

3.2. *The strength–density chart*

Data for the strength σ_f and density ρ of natural materials are shown in figure 3. For natural ceramics, the compressive strength is identified by the symbol (C); the tensile strength (which is much lower) is identified with the modulus of rupture in beam bending, symbol (T). For natural polymers and elastomers, the strengths are tensile strengths. For natural cellular materials, the compressive strength is the stress plateau, symbol (C), while the tensile stress is either the stress plateau or the modulus of rupture, symbol (T), depending on the nature of the material. Where they differ, the strengths parallel (symbol $\|$) and perpendicular (symbol $\perp$) to the fibre orientation or grain have been plotted separately. Strength guidelines are shown for the material indices:

$$M_4 = \sigma_f/\rho \quad \text{(tie under uniaxial load),}$$
$$M_5 = \sigma_f^{2/3}/\rho \quad \text{(a beam in flexure),}$$
$$M_6 = \sigma_f^{1/2}/\rho \quad \text{(a plate in flexure).}$$

Evolution to provide tensile strength would, we expect, result in materials with high values of σ_f/ρ; where strength in bending or buckling is required we expect to find materials with a high $\sigma_f^{2/3}/\rho$. Silk and cellulose have the highest values of σ_f/ρ; that of silk is even higher than that of carbon fibres. The fibres flax, hemp and cotton, too, have high values of this index. Bamboo, palm and wood have high values of $\sigma_f^{2/3}/\rho$, giving resistance to flexural failure.

3.3. *The Young's modulus–strength charts*

Data for the strength σ_f and modulus E of natural materials are shown in figures 4 and 5. Guidelines are shown for the material indices:

$$M_7 = \frac{\sigma_f^2}{E} \text{ (maximum elastic strain energy per unit volume; springs of minimum volume),}$$

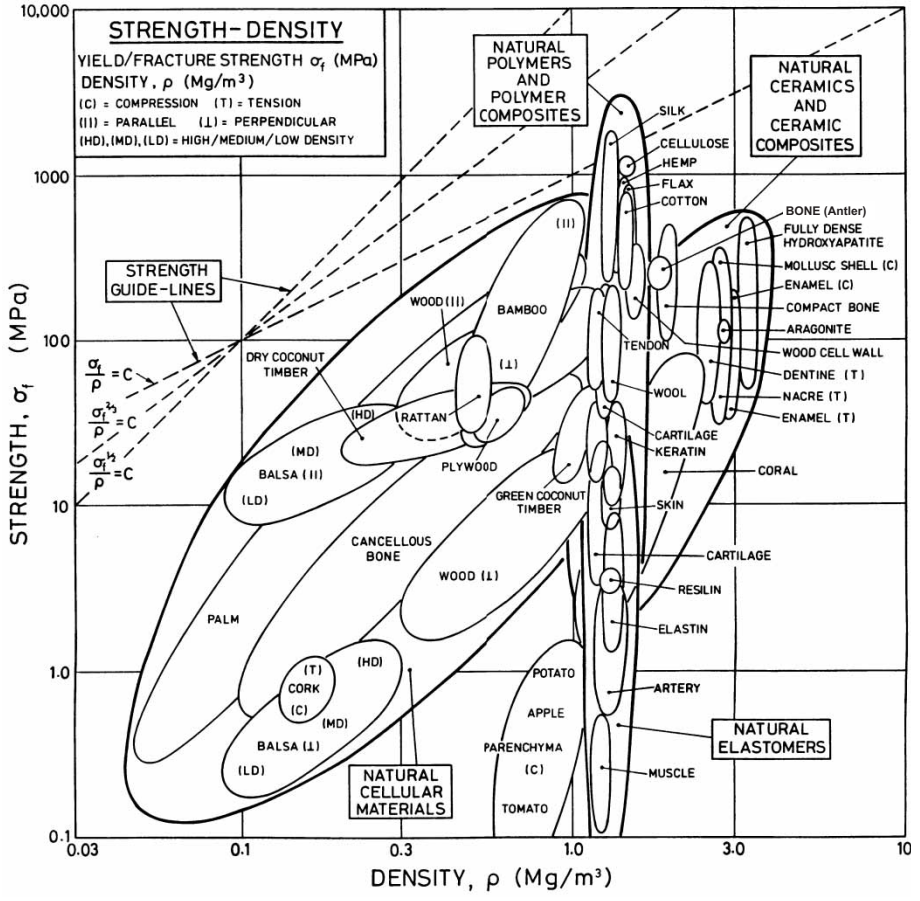

Figure 3. A material property chart for natural materials, plotting strength against density. Guidelines identify structurally efficient materials that are light and strong.

$$M_8 = \frac{\sigma_f}{E} \quad \text{(allow large, recoverable deformations; elastic hinges),}$$

$$M_9 = \frac{\sigma_f^2}{E\rho} \quad \text{(maximum elastic strain energy per unit mass; springs of minimum mass).}$$

Materials with large values of σ_f^2/E and $\sigma_f^2/E\rho$ store elastic energy and make good springs, and those with large values of σ_f/E have exceptional resilience. Silks (including the silks of spider's webs) stand out as exceptionally efficient, having values of σ_f^2/E and $\sigma_f^2/E\rho$ that exceed those of spring steel or rubber. High values of the other index, σ_f/E, mean that a material allows large recoverable deflections and, for this reason, make good elastic hinges. Nature makes much use of these; skin, leather and cartilage are all required to act as flexural and torsional hinges. Palm (coconut timber) has a particularly high value of this index, allowing it to flex in a high wind; the drag on the tree is reduced when the trunk bends to an arc, allowing the fronds to form a streamline shape.

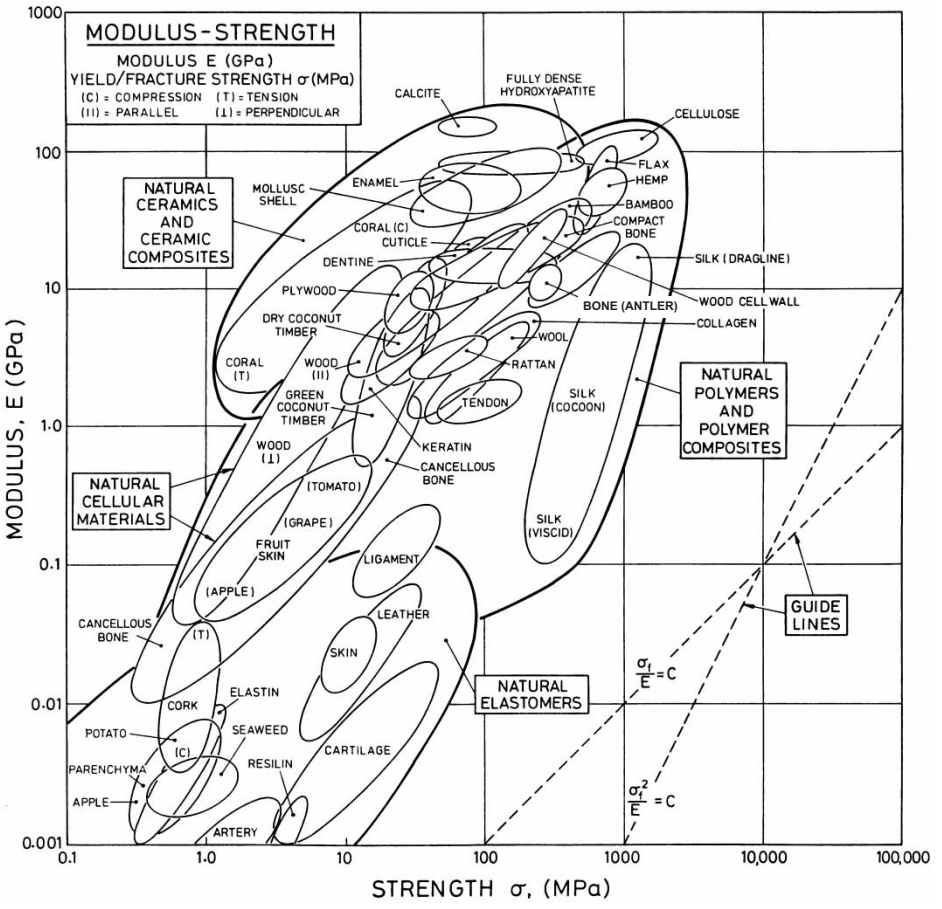

Figure 4. A material property chart for natural materials, plotting Young's modulus against strength. Guidelines identify materials that store the most elastic energy per unit volume and that make good elastic hinges.

3.4. *The toughness–Young's modulus chart*

The toughness of a material measures its resistance to the propagation of a crack. The limited data for the toughness J_c and Young's modulus E of natural materials are shown in figure 6.

The material index for fracture-safe design depends on the design goal. When the component is required to absorb a given *impact energy* without failing, the best material will have the largest value of

$$M_{10} = J_c.$$

These materials lie at the top of figure 6; antler, bamboo and wood stand out. When instead a component containing a crack must carry a given *load* without failing, the safest choice of material is that with the largest values of the fracture toughness K_{1c}:

$$M_{10} = K_{1c} \approx (EJ_c)^{1/2}.$$

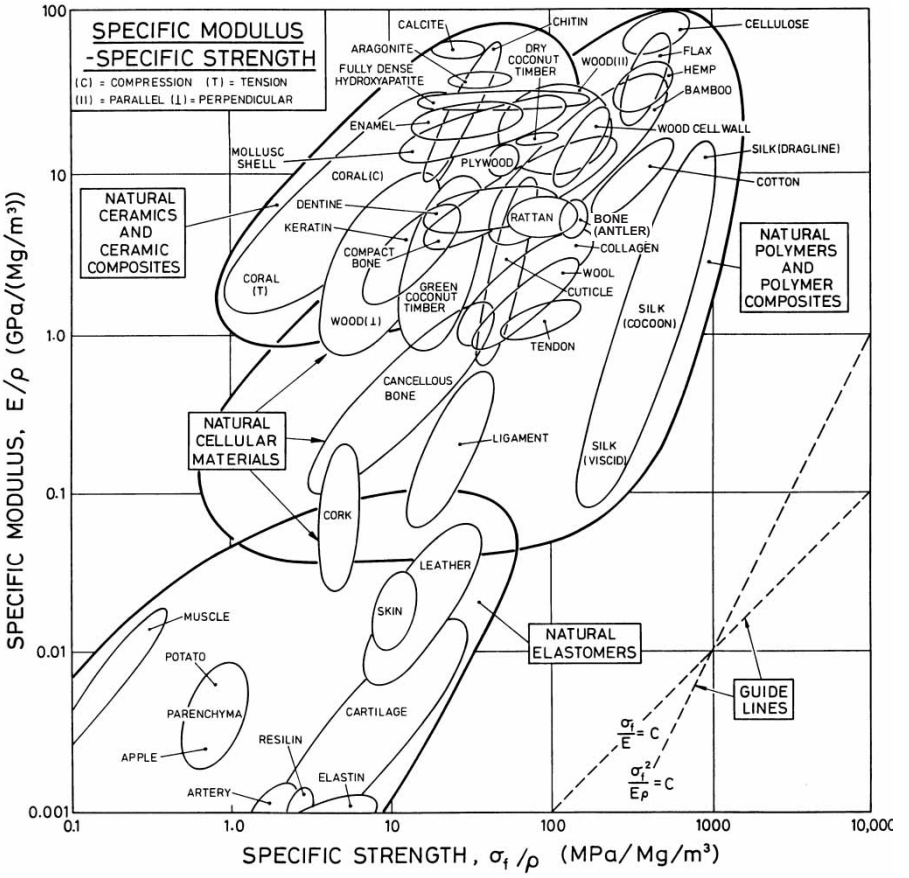

Figure 5. A material property chart for natural materials, plotting specific Young's modulus against specific strength. Guidelines identify materials that store the most elastic energy per unit weight and that make good elastic hinges.

Diagonal contours sloping from the upper left to lower right on figure 6 show values of this index. Nacre and enamel stand out. When the component must support a given *displacement* without failure, the material is measured by

$$M_{12} = \left(\frac{J_c}{E}\right)^{1/2}.$$

This is shown as a second set of diagonal contours sloping from the lower left to upper right in figure 6. Skin is identified as particularly good by this criterion.

Many engineering materials (steels, aluminium and alloys) have values of J_c and K_{1c} that are much higher than those of the best natural materials. However, the toughnesses of natural ceramics such as nacre, dentine, bone and enamel are an order of magnitude higher than those of conventional engineering ceramics such as alumina. Their toughness derives from their microstructure: platelets of ceramics such as calcite, hydroxyapatite or aragonite, bonded by a small volume fraction of polymer, collagen when the ceramic is a phosphate, and other proteins when it is

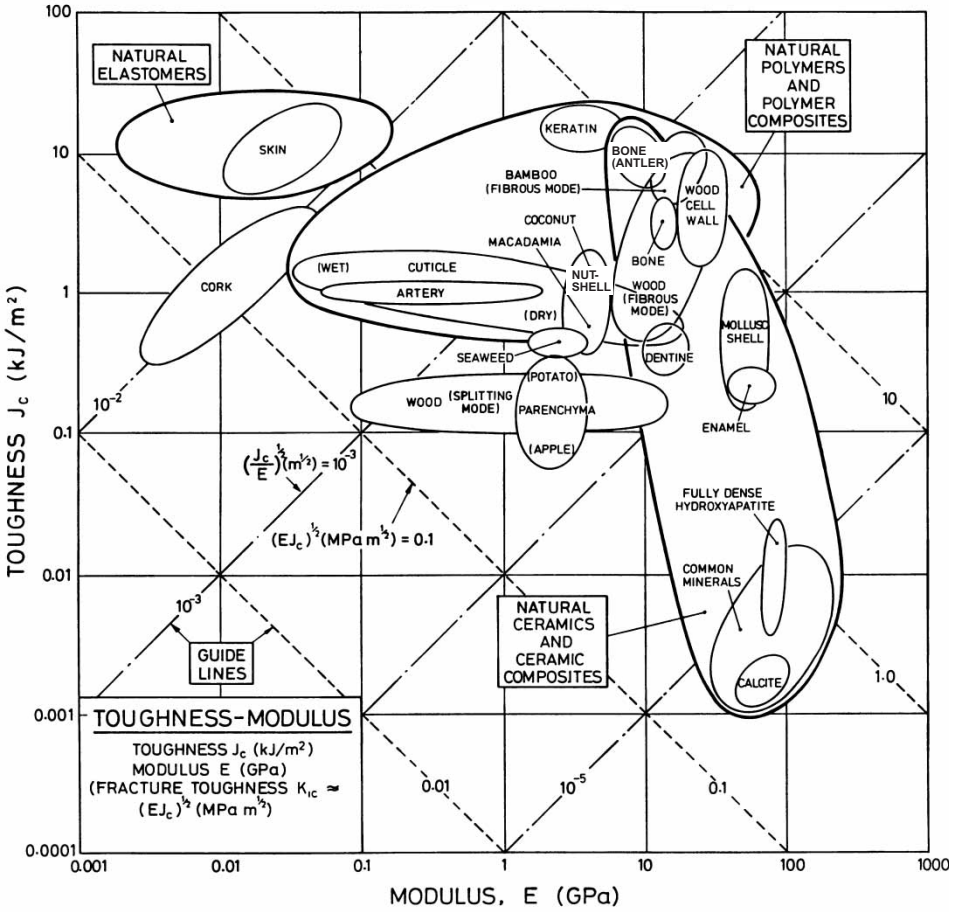

Figure 6. A material property chart for natural materials, plotting toughness against Young's modulus. Guidelines identify materials best able to resist fracture under various loading conditions.

a carbonate. Their toughness increases with decreasing mineral content and increasing collagen content.

§4. Conclusions

Natural materials perform many functions. One, commonly, is mechanical, providing stiffness, strength and toughness, allowing stretch and flexure or acting as a spring. They do so using a limited chemical palette—proteins, polysaccharides, and calcites and aragonites—arranged in elaborate interwoven or interlocking structures. The remarkable efficiency of natural materials (their performance per unit mass) has its origins in these structures. It can be explored by creating material property charts, of which five are presented here. The charts condense large bodies of data into single 'maps', showing the relationship between the properties of differing classes of materials and allowing ranking by a set of 'material indices' that measure performance. The results presented here confirm the high efficiency of natural materials and suggest that a number of them have evolved to meet specific mechanical requirements. The charts give perspective and, since equivalent charts already

exist for engineering materials, they allow a match to be sought between those of nature and those that are man made.

To what extent has the study of nature influenced engineering design? The most successful biomimetic designs are, arguably, based on nature-inspired *structures* rather than *materials* (Velcro, with the hook-like structure of burrs; dirt-repelling surfaces with the hydrophobic surface structure of the leaf of the lotus flower; anti-slip shoe soles with the wave-like grooves of dogs' paws; low-drag surfaces modelled on shark's skin, although it is not yet demonstrated that these last actually work). These structures succeed by exploiting one 'design' feature of a natural structure without attempting to reproduce the natural structure in its entirety. Attempts to make artificial wood, cork, bone and skin, reproducing not one, but all (or almost all) their physical, chemical and physiological functions are less successful for two reasons: their multiple-hierarchical structure is difficult to reproduce, and we do not yet know how to make structures that repair themselves when damaged.

Natural materials have many structural levels (molecular, molecular assembly, micro-composite, cellular, macrocomposite, etc.) and are, following Darwin's thinking, optimized for efficiency at each level. Defects at one level (a broken cell wall, for instance) could compromise the integrity of the levels above, leading to failure of the entire structure. Nature deals with this through the capacity for self-repair and healing but, in man-made materials, integrity is possible only through rigorous quality control during manufacture, and by meticulous inspection during use. Ensuring the integrity of man-made structures with multilevel structural hierarchy is exceptionally difficult.

From this we conclude that, since the constraints of industrial production and use have to be met, successful bionic design can only exploit some of the generic structural principles of optimization found in nature, and that it has to adapt them, often greatly. In doing so, something is lost, but it is nonetheless a profitable route for the development of novel and improved materials and structures.

Acknowledgements

We wish to thank Professor J. F. V. Vincent, Professor J. D. Currey and Professor L. J. Gibson for numerous helpful discussions and the provision of data.

References

Ashby, M. F., 1999, *Materials Selection in Mechanical Design*, second edition (Oxford: Butterworth–Heinemann).

Ashby, M. F., Gibson, L. J., Wegst, U. G. K., and Olive, R., 1995, *Proc. R. Soc.* A, **450**, 123.

Bappert, R., Benner, S., Hacker, B., Kern, U., and Zweckbronner, G., 1998, *Bionik, Zukunfts-Technik lernt von der Natur* (Landesmuseum für Technik und Arbeit in Mannheim).

Beukers, A., and Van Hinte, E., 1998, *Lightness. The Inevitable Renaissance of Minimum Energy Structures* (Rotterdam: 010 Publishers).

Sarikaya, M., and Aksay, I. A. (editors), 1995, *Biomimetics: Design and Processing of Materials* (Woodbury: AIP Press).

Thompson, D'A. W., 1992, *On growth and form* (London: Dover Publications).

Vincent, J. F. V., 1990, *Structural Biomaterials*, revised edition (Princeton University Press).

Vincent, J. F. V., and Currey, J. D., 1980, *The Mechanical Properties of Biological Materials*, Proceedings of the Symposia of the Society for Experimental Biology, Vol. 34 (Cambridge University Press).

Wainwright, S. A., Biggs, W. D., Currey, J. D., and Gosline, J. M., 1976, *Mechanical Design in Organisms* (Princeton University Press).

Wegst, U. G. K., 1996, PhD Thesis, Department of Engineering, University of Cambridge, Cambridge, UK.

Data and data sources

The data plotted in the natural materials selection chart are derived from a large number of sources listed after the references under the heading Data sources. Care has been taken to cross-check and compare values from more than one source, examining them for consistency with their composition, structure and physical rules. A typical range of values for each property of each material is shown by bubbles. A word of caution is needed here; natural materials show a large variability in properties. The value of a property varies within an organism, between organisms and between species, and with age and moisture content. Some of the properties plotted in the charts appear to show less variability than others, but this may simply be due to the lack of data; additional tests are likely to reveal a wider range.

Data sources

Natural materials in general

Alexander, R. M., 1983, *Animal Mechanics*, second edition (Oxford: Blackwell Scientific).
Brown, C. H., 1975, *Structural Materials in Animals* (London: Pitman).
Currey, J. D., Wainwright, S. A., and Biggs, W. D., 1982, *Mechanical Design in Organisms* (Princeton University Press).
Fung, Y. C., 1993, *Biomechanics: Mechanical Properties of Living Tissues*, second edition (New York: Springer).
Gibson, L. J., and Ashby, M. F., 1997, *Cellular Solids: Structure and Properties*, second edition (Cambridge University Press).
McMahon, T. A., 1984, *Muscles, Reflexes, and Locomotion* (Princeton University Press).
Silver, F. H., 1987, *Biological Materials: Structure, Mechanical Properties, and Modeling of Soft Tissues* (New York: University Press).
Vincent, J. F. V., and Currey, J. D., 1980, *The Mechanical Properties of Biological Materials*, Proceedings of the Symposia of the Society for Experimental Biology, Vol. 34 (Cambridge University Press).
Vogel, S., 1988, *Life's Devices: the Physical World of Animals and Plants*, illustrated by R. A. Calvert (Princeton University Press).
Yamada, H., 1970, *Strength of Biological Materials* (Baltimore, Maryland: Williams & Wilkins).

Wood and wood-like materials (Wood cell wall, wood, cork, bamboo, palm and rattan)

Amada, S., Munekata, T., Nagase, Y., Ichikawa, Y., Kirigai, A., and Yang, Z. F., 1996, *J. Composite Mater.*, **30**, 800.
Bhat, K., and Mathew, A., 1995, *Biomimetics*, **3**, 67.
Frühwald, A., Peek, R.-D., and Schulte, M., 1992, Mitt. Bundesforschungsanst. Forst-Holzwirt., **171**, 1.
Gibson, L. J., Easterling, K. E., and Ashby, M. F., 1981, *Proc. R. Soc.* A, **377**, 99.
Godbole, V. S., and Lakkad, S. C., 1986, *J. Mater. Sci. Lett.*, **5**, 303.
Janssen, J. J. A., 1991, *Mechanical Properties of Bamboo*, Forestry Sciences, Vol. 37 (Dordrecht: Kluwer).
Killmann, W., 1983, *Wood Sci. Technol.*, **17**, 167; 1993, PhD Thesis, Universität Hamburg, Germany.
Kloot, N., 1952, *Aust. J. appl. Sci.*, **3**, 293.
Lakkad, S. C., and Patel, J. M., 1981, *Fibre Sci. Technol.*, **14**, 319.

MARK, R. E., 1967, *Cell Wall Mechanics of Tracheids* (New Haven, Connecticut: Yale University Press).
RICH, P. M., 1987, *Bot. Gaz.*, **148**, 42.
ROSA, M. E., and FORTES, M. A., 1988a, *J. Mater. Sci.*, **23**, 35; 1988b, *ibid.*, **23**, 879; 1991, *ibid.*, **26**, 341.

Plant tissue (apple and potato parenchyma, fruit skins, seaweed and nuts)

BLAHOVEC, J., 1988, *J. Mater. Sci.*, **23**, 3588.
GIBSON, L. J., and ASHBY, M. F., 1997, *Cellular Solids: Structure and Properties*, second edition (Cambridge University Press).
GREENBERG, A. R., MEHLING, A., LEE, M., and BOCK, J. H., 1989, *J. Mater. Sci.*, **24**, 2549.
JENNINGS, J. S., and MACMILLAN, N. H., 1986, *J. Mater. Sci.*, **21**, 1517.
VENKATASWAMY, M. A., PILLAI, C. K. S., PRASAD, V. S., and SATYANARAYANA, K. G., 1987, *J. Mater. Sci.*, **22**, 3167.
VINCENT, J. F. V., 1989, *J. Sci. Food. Agric.*, **47**, 443; 1990, *Adv. bot. Res.*, **17**, 235.
WANG, C. H., and MAI, Y. W., 1994, *Int. J. Fracture*, **69**, 67.
WANG, C. H., ZHANG, L. C., and MAI, Y. W., 1994, *Int. J. Fracture*, **69**, 51.

Cellulose, cotton, flax, hemp, jute and ramie

CURREY, J. D., WAINWRIGHT, S. A., and BIGGS, W. D., 1982, *Mechanical Design in Organisms* (Princeton University Press).
GIBSON, L. J., and ASHBY, M. F., 1997, *Cellular Solids: Structure and Properties*, second edition (Cambridge University Press).
VINCENT, J. F. V., 1990, *Structural Biomaterials*, revised edition (Princeton University Press).
WAINWRIGHT, S. A., 1980, *The Mechanical Properties of Biological Materials*, Proceedings of the Symposia of the Society for Experimental Biology, Vol. 34, edited by J.F.V. Vincent and J. D. Currey (Cambridge University Press), p. 483.
WAINWRIGHT, S. A., BIGGS, W. D., CURREY, J. D., and GOSLINE, J. M., 1976, *Mechanical Design in Organisms* (Princeton University Press).
WAINWRIGHT, S. A., GOSLINE, J. M., and BIGGS, W. D., 1992, *Mechanical Design in Organisms* (Princeton University Press).

Silk

CALVERT, P., 1989, *Nature*, **340**, 266.
DENNY, M., 1980, *The Mechanical Properties of Biological Materials*, Proceedings of the Symposia of the Society for Experimental Biology, Vol. 34, edited by J. F. V. Vincent and J. D. Currey (Cambridge University Press), pp. 247–272.
GOSLINE, J. M., DEMONT, M. E., and DENNY, M. W., 1986, *Endeavour*, **10**, 37.

Elastin, resilin and abductin

GOSLINE, J., 1980, *The Mechanical Properties of Biological Materials*, Proceedings of the Symposia of the Society for Experimental Biology, Vol. 34, edited by J. F. V. Vincent and J. D. Currey (Cambridge University Press), pp. 331–357.
OXLUND, H., MANSCHOT, J., and VIIDIK, A., 1988, *J. Biomech.*, **21**, 213.

Collagen, ligament and tendon

ANDERSEN, K. L., PEDERSEN, E. H., and MELSEN, B., 1991, *Am. J. Orthod. Dentofac. Orthop.*, **99**, 427.
BENNETT, M. B., KER, R. F., DIMERY, N. J., and ALEXANDER, R. M., 1986, *J. Zool.*, **209**, 537.
BOSCH, U., DECKER, B., KASPERCZYK, W., NERLICH, A., OESTERN, H. J., and TSCHERNE, H., 1992, *J. Biomech.*, **25**, 821.
BUTLER, D. L., KAY, M. D., and STOUFFER, D. C., 1986, *J. Biomech.*, **19**, 425.
GRIESHABER, F. A., and FAUST, U., 1992, *Biomed. Technik*, **37**, 278.
KATO, Y. P., CHRISTIANSEN, D. L., HAHN, R. A., SHIEH, S. J., GOLDSTEIN, J. D., and SILVER, F. H., 1989, *Biomaterials*, **10**, 38.
KER, R. F., 1981, *J. exp. Biol.*, **93**, 283.

Ker, R. F., Alexander, R. M., and Bennett, M. B., 1988, *J. Zool.*, **216**, 309.
Park, J. B., and Lakes, R. S., 1992, *Biomaterials*, second edition (New York: Plenum).
Rogers, G. J., Milthorpe, B. K., Muratore, A., and Schindhelm, K., 1990, *Biomaterials*, **11**, 89.
Silver, F. H., Kato, Y. P., Ohno, M., and Wasserman, A. J., 1992, *J. Long Term Effects Med. Implants*, **2**, 165.
Vincent, J. F. V., 1990, *Structural Biomaterials*, revised edition (Princeton University Press).
Wainwright, S., 1980, *The Mechanical Properties of Biological Materials*, Proceedings of the Symposia of the Society for Experimental Biology, Vol. 34, edited by J. F. V. Vincent and J. D. Currey (Cambridge University Press), pp. 483–453.
Wang, X. T., and Ker, R. F., 1995, *J. exp. Biol.*, **198**, 831.
Wang, X. T., Ker, R. F., and Alexander, R. M., 1995, *J. exp. Biol.*, **198**, 847.

Muscle

Dobrunz, L. E., Pelletier, D. G., and McMahon, T. A., 1990, *Biophys. J.*, **58**, 557.
Yamada, H., 1970, *Strength of Biological Materials* (Baltimore, Maryland: Williams & Wilkins).

Skin

Bauer, A. M., Russell, A. P., and Shadwick, R. E., 1989, *J. exp. Biol.*, **145**, 79.
Manschot, J. F. M., and Brakkee, A. J. M., 1986a, *J. Biomech.*, **19**, 511; 1986b, *ibid.*, **19**, 517.
Oxlund, H., Manschot, J., and Viidik, A., 1988, *J. Biomech.*, **21**, 213.
Silver, F. H., Kato, Y. P., Ohno, M., and Wasserman, A. J., 1992, *J. Long Term Effects Med. Implants*, **2**, 165.
Swartz, S. M., Groves, M. S., Kim, H. D., and Walsh, W. R., 1996, *J. Zool.*, **239**, 357.

Leather

Attenburrow, G. E., and Wright, D. M., 1994, *J. Am. Leather Chem. Assoc.*, **89**, 391.
Kronick, P., and Maleef, B., 1992, *J. Am. Leather Chem. Assoc.*, **87**, 259.
Lin, J., and Hayhurst, D. R., 1993a, *Eur. J. Mech. A—Solids*, **12**, 471; 1993b, *ibid.*, **12**, 493.

Cartilage

Rains, J. K., Bert, J. L., Roberts, C. R., and Pare, P. D., 1992, *J. appl. Physiol.*, **72**, 219.
Silver, F. H., Kato, Y. P., Ohno, M., and Wasserman, A. J., 1992, *J. Long Term Effects Med. Implants*, **2**, 165.
Swanson, S., 1980, *The Mechanical Properties of Biological Materials*, Proceedings of the Symposia of the Society for Experimental Biology, Vol. 34, edited by J. F. V. Vincent and J. D. Currey (Cambridge University Press), pp. 377–395.

Bone (including antler)

Ashman, R. B., Corin, J. D., and Turner, C. H., 1987, *J. Biomech.*, **20**, 979.
Ashman, R. B., and Rho, J. Y., 1988, *J. Biomech.*, **21**, 177.
Currey, J. D., 1984, *The Mechanical Adaptions of Bones* (Princeton University Press); 1988, *J. Biomech.*, **21**, 439; 1990, *ibid.*, **23**, 837.
Dickenson, R. P., Hutton, W. C., and Stott, J. R. R., 1981, *J. Bone Jt Surg., Brit. Vol.*, **63**, 233.
Gibson, L. J., 1985, *J. Biomech.*, **18**, 317.
Goldstein, S. A., 1987, *J. Biomech.*, **20**, 1055.
Kitchener, A., 1991, *Biomechanics in Evolution*, Society for Experimental Biology Seminar Series, Vol. 36, edited by J. Rayner and R. Woolton (Cambridge University Press), pp. 229–253.
Linde, F., and Hvid, I., 1987, *J. Biomech.*, **20**, 83.
Lotz, J. C., Gerhart, T. N., and Hayes, W. C., 1991, *J. Biomech.*, **24**, 317.
Moyle, D. D., and Gavens, A. J., 1986, *J. Biomech.*, **19**, 919.
Moyle, D. D., and Walker, M. W., 1986, *J. Biomech.*, **19**, 613.

Sharp, D. J., Tanner, K. E., and Bonfield, W., 1990, *J. Biomech.*, **23**, 853.
Sun, J. J., and Geng, J., 1987, *J. Biomech.*, **20**, 815.
Swanson, S., 1980, *The Mechanical Properties of Biological Materials*, Proceedings of the Symposia of the Society for Experimental Biology, Vol. 34, edited by J. F. V. Vincent and J. D. Currey (Cambridge University Press), pp. 377–395.
Watkins, M., 1987, PhD Thesis, University of Reading, Reading, Berkshire, UK.

Dentine and enamel

Brear, K., Currey, J. D., Pond, C. M., and Ramsay, M. A., 1990, *Arch. Oral Biol.*, **35**, 615.

Coral

Chamberlain, J., 1978, *Paleobiology*, **4**, 419.
Kim, K., Goldberg, W. M., and Taylor, G. T., 1992, *Biol. Bull.*, **182**, 195.
Scott, P. J. B., and Risk, M. J., 1988, *Coral Reefs*, **7**, 145.
Vosburgh, F., 1982, *Proc. R. Soc.* B, **214**, 481.

Alpha-keratins

Bertram, J. E. A., and Gosline, J. M., 1986, *J. exp. Biol.*, **125**, 29; 1987, *ibid.*, **130**, 121.
Fraser, R., and Macrae, T., 1980, *The Mechanical Properties of Biological Materials*, Proceedings of the Symposia of the Society for Experimental Biology, Vol. 34, edited by J. F. V. Vincent and J. D. Currey (Cambridge University Press), pp. 211–246.
Kitchener, A., 1991, *Biomechanics in Evolution*, Society for Experimental Biology Seminar Series, Vol. 36, edited by J. Rayner and R. Woolton (Cambridge University Press), pp. 229–253.

Insect cuticle

Alexander, D. E., Blodig, J., and Hsieh, S. Y., 1995, *Invertebrate Biol.*, **114**, 169.
Gunderson, S., and Whitney, J., 1992, *Biomimetics*, **1**, 177.
Vincent, J., 1980, *The Mechanical Properties of Biological Materials*, Proceedings of the Symposia of the Society for Experimental Biology, Vol. 34, edited by J. F. V. Vincent and J. D. Currey (Cambridge University Press), pp. 183–210.

Mollusc shell

Jackson, A. P., Vincent, J. F. V., and Turner, R. M., 1988, *Proc. R. Soc.* B, **234**, 415; 1990, *J. Mater. Sci.*, **25**, 3173.

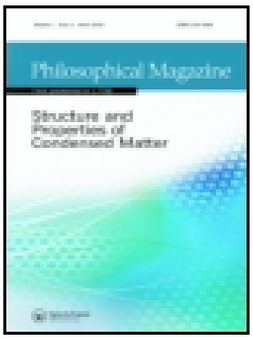

Philosophical Magazine

ISSN: 1478-6435 (Print) 1478-6443 (Online) Journal homepage: www.tandfonline.com/journals/tphm20

The influence of efficient atomic packing on the constitution of metallic glasses

D.B. Miracle, W.S. Sanders & O. N. Senkov

To cite this article: D.B. Miracle, W.S. Sanders & O. N. Senkov (2003) The influence of efficient atomic packing on the constitution of metallic glasses, Philosophical Magazine, 83:20, 2409-2428, DOI: 10.1080/14786430310000098828

To link to this article: https://doi.org/10.1080/14786430310000098828

Published online: 01 Feb 2008.

PHILOSOPHICAL MAGAZINE, 11 July 2003
VOL. 83, NO. 20, 2409–2428

Taylor & Francis
Taylor & Francis Group

The influence of efficient atomic packing on the constitution of metallic glasses

D. B. MIRACLE†, W. S. SANDERS

Air Force Research Laboratory, Materials and Manufacturing Directorate, Wright–Patterson Air Force Base, Ohio 45433-7817, USA

and O. N. SENKOV

UES, Inc., Dayton, Ohio 45432-1894, USA

[*Received 5 August 2002 and accepted in revised form 20 January 2003*]

ABSTRACT

Efficient atomic packing is shown to be a fundamental consideration in the formation of metallic glasses. A simple concept of packing efficiency, based on atom packing in the first coordination shell of solute-centred clusters, is proposed and developed. This model leads to the prediction that specific radius ratios, defined as the radius of the solute atom divided by the radius of the solvent atom, are preferred in the constitution of metallic glasses. Analysis of a large number of binary and complex metallic glasses shows that these specific critical radius ratios R^* are indeed preferred in known metallic glasses. The predictions of this model extend previous proposals to describe the influence of topology on the formation of metallic glasses. Although this model represents a simple idealization, the strong agreement with published metallic glasses suggests that efficient atomic packing, enabled by solute-centred clusters, forms a fundamental consideration in the constitution of metallic glasses.

§1. INTRODUCTION

A notable characteristic of metallic glasses is their high density relative to the crystalline state of the same alloy composition. Metallic glass alloys have densities that are typically 97% or more of the density in the crystalline state, and the best glass-forming alloys have densities that are 99.5% or more of the crystalline density (Dougherty *et al.* 1994, Yavari and Inoue 1999). Compare these values with relative densities of conventional metal alloys in the amorphous (molten) state that typically range from 92 to 94% of the density of the crystalline state (Egami 1997). This high relative density for metallic glasses requires that atomic packing is exceptionally efficient in the amorphous structure. Efficient atomic packing produces a relatively low system volume, which reduces the thermodynamic free volume and hence the energy of the amorphous structure. Efficiently packed atoms also produce a more viscous liquid, which can significantly decrease the kinetics of nucleation and growth of the competing crystalline state. It is known that the most stable metallic glass

† Author for correspondence. Email: daniel.miracle@wpafb.af.mil.

Philosophical Magazine ISSN 1478–6435 print/ISSN 1478–6443 online © 2003 US Government
http://www.tandf.co.uk/journals
DOI: 10.1080/1478643031000098828

compositions often coincide with a minimum in molar volumes (Ramachandrarao 1980, Jin *et al.* 2000).

Packing efficiency has been analysed for unary (Bernal 1964, Scott and Kilgour 1969, Finney 1970) and binary (Visscher and Bolsterli 1972, Clarke and Wiley 1987, Zheng *et al.* 1995) non-crystalline arrays of hard spheres. In general, a mixture of spheres of different sizes produces a more efficiently packed structure than can be achieved with separate constituents, and the increase in packing efficiency becomes greater as the disparity in sizes of the constituent spheres increases. This idea, coupled with the model of dense random packing (DRP), has been used to conceptualize the high relative density of amorphous metals. However, calculations of the increased packing fraction obtained by mixing spheres of relative sizes and numbers that might represent a binary metallic glass fall well below densities obtained experimentally (Visscher and Bolsterli 1972, Clarke and Wiley 1987). For example, metallic glasses typically have solute atoms with radius ratios R (the solute atom radius normalized by the solvent atom radius) that range from about 0.6 to 1.4, and solute atom fractions that generally range from about 5 to 30% (Egami and Waseda 1984, Miracle 2003). Using a recent analysis (Zheng *et al.* 1995), where the reference packing fraction of both small and large spheres is the DRP limit of about 0.64, the packing fraction of a binary mixture of spheres increases to a maximum value of only 0.661 for $R = 0.6$ (figure 1). This is well below the packing fraction expected for a typical crystalline array and is inconsistent with the high relative

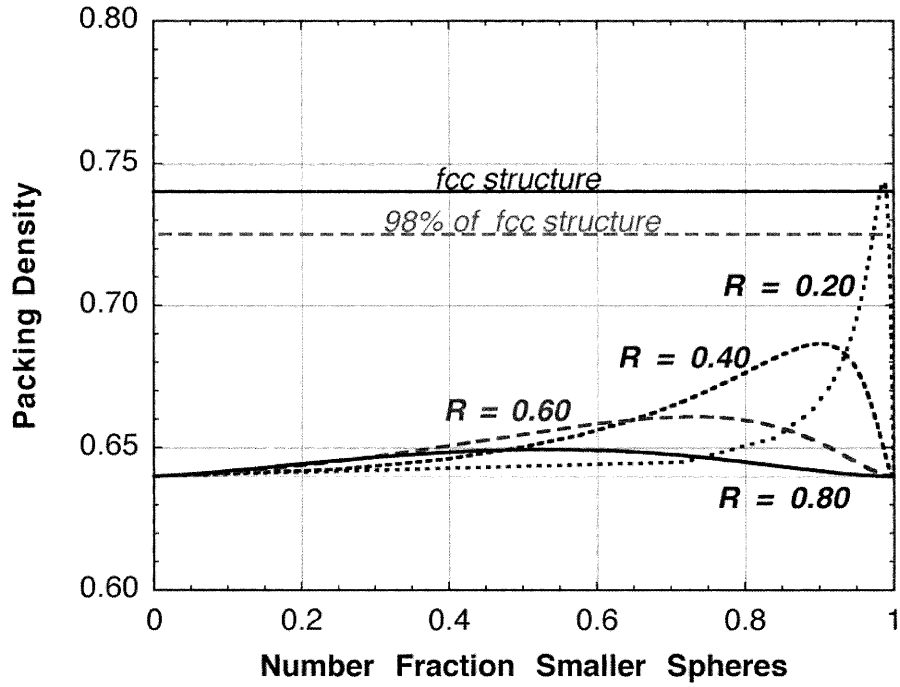

Figure 1. The relative packing density of a binary mixture of spheres with radius ratios from 0.2 to 0.8 from the Furnas model (Zheng *et al.* 1995). Only a small increase is predicted over the starting packing fraction of 0.64 for radius ratios that represent metallic glasses ($0.6 \leqslant R \leqslant 1$). The packing density of 0.74 for a fcc array is shown for reference.

density measured for metallic glasses (Visscher and Bolsterli 1972, Clarke and Wiley 1987). While the assumptions of this model seem to be inappropriate for systems with solute radii that are a significant fraction of the solvent, a similar increase has been calculated using a more rigorous three-dimensional computer simulation for binary mixtures of spheres (Clarke and Wiley 1987).

It has been suggested that metallic glasses are formed in systems where the solute atoms occupy interstices that exist in a DRP unary amorphous structure (Polk 1972). However, more rigorous analysis has concluded that the number and size of 'holes' that might accommodate solutes are insufficient, even for metal–metalloid glasses (Frost 1982). Thus, existing concepts based on the DRP of spheres of different sizes are unable to account for the high density of amorphous alloys relative to the crystalline state of the same composition. New ideas are required to explain this important feature, which has fundamental implications for understanding the atomic structure of metallic glasses.

The concept explored here for metallic glasses is the possibility of topologically ordered atomic configurations (i.e. clusters) with a high local packing efficiency. Clusters such as tetrahedra and octahedra have high local packing fractions that increase further if the interstice is filled. These are the familiar building blocks of many crystalline structures (Wells 1984), and the tetrahedron is also a fundamental building block of crystalline and amorphous silicate structures. Since tetrahedral and octahedral clusters require solutes that are much smaller than typically exist in metallic glass alloys, these are not likely in metallic glasses. By extension to solutes of sizes that are typically found in metallic glasses ($0.6 \leqslant R \leqslant 1.4$), different atomic clusters may exist that also possess high local packing efficiency. The capped trigonal prism, with $R = 0.732$ and a coordination number of 9, and icosahedra, with $R = 0.902$ and a coordination number of 12, are two such solute-centred clusters that are known to exist in metallic glass structures. Atomic configurations that represent different solute radius ratios and coordination numbers may also exist, but there has not been any significant systematic attempt to explore this possibility.

There is at present no evidence for the occurrence or the importance of other related clusters that may exist in the structure of amorphous metals. The nature of other potential, efficiently packed configurations and the rules for their occurrence are not, in general, established for metallic glasses. The objective of this work is to explore the role of topology in the formation of local atomic configurations with a high packing efficiency. The relative size of constituent atoms will be the primary topological parameter considered. The specific atomic configurations that produce a high local packing efficiency will not be addressed here but will be considered in detail in a subsequent study. Rather, the focus of this work will be to define the principles that control local packing efficiency, and to explore the impact of these principles on the constitution of metallic glasses. The predictions from this work will be compared against a broad range of known metallic glass systems and will be used to explain some of the phenomenological characteristics of atomic size distribution plots (ASDPs) which characterize marginal and bulk metallic glass systems (Miracle and Senkov 2001, Senkov and Miracle 2001).

§2. A MODEL FOR PACKING EFFICIENCY

It is well known that the atomic size of solute atoms relative to the solvent atoms exerts an important influence on the ability to form metallic glasses. An empirical guideline suggests that a size difference greater than 12% is required to form

amorphous metals (Inoue 2000). A more quantitative model based on local elastic strains introduced by solute atoms has shown that the critical solute concentration required to form a metallic glass is inversely proportional to the difference between the atomic volumes of the solvent and solute (Egami and Waseda 1984). ASDPs show two distinct profiles of solute size versus solute content; one profile is observed for marginal glass-forming metal alloys and a small number of bulk metallic glasses, and a second for the majority of bulk metallic glasses (Miracle and Senkov 2001, Senkov and Miracle 2001). The concepts discussed above to model the higher packing efficiency of binary mixtures of spheres possess an explicit dependence on the ratio of the radius of solute atoms to the radius of solvent atoms. These observations support the critical role of the relative size of solute and solvent atoms in the formation, stability and structure of metallic glasses.

2.1. *Two dimensions*

A simple illustration of the influence of radius ratio on packing efficiency in the first coordination shell is provided in two dimensions by considering binary clusters consisting of a central circle i of radius r_i, and its first-nearest neighbours j, all of equivalent radius r_j. For a radius ratio $R = r_i/r_j$, the theoretical coordination number N^T is given as (Egami 1997)

$$N^T = \frac{\pi}{\arcsin[1/(1+R)]}. \tag{1}$$

N^T is a real number representing the number of whole and fractional j circles that can be placed around a central i circle. In a physical system, the coordination number is constrained to be an integer number N of j spheres and the additional fractional component included in N^T accounts for the gaps between full circles. A simple representation of the local packing efficiency is obtained by truncating N^T to the nearest smaller integer N and dividing by N^T. The maximum possible value for this ratio is unity when $N^T\{R\}$ is an integer. This occurs for a specific set of radius ratios R_N^* where the subscript N specifies the particular coordination number obtained for the specific value of R^*. The packing efficiency decreases gradually as R increases from a given value of R_N^*, since N^T increases steadily, while N does not change for small increases in R. As R continues to increase, a discontinuous increase in packing efficiency (to unity) occurs; N becomes $N+1$ when the radius ratio becomes R_{N+1}^*. Conversely, a discontinuous decrease in packing efficiency occurs for a small decrease in R from a value of R_N^*, since a small decrease in N^T is accompanied by a decrease of 1 in N. The dependence of N^T and packing efficiency on R is shown in figure 2 for two dimensions.

2.2. *Three dimensions*

The definitions and discussion for circles in two dimensions can be extended to represent binary clusters of spheres in three dimensions, where i represents a central solute sphere and j represents solvent spheres. A simple estimate for the three-dimensional coordination number N^T, which is obtained for a radius ratio R, is (Egami 1997)

$$N^T = \frac{4\pi(1 - 3^{1/2}/2)}{1 - [R(R+2)]^{1/2}/(R+1)}. \tag{2}$$

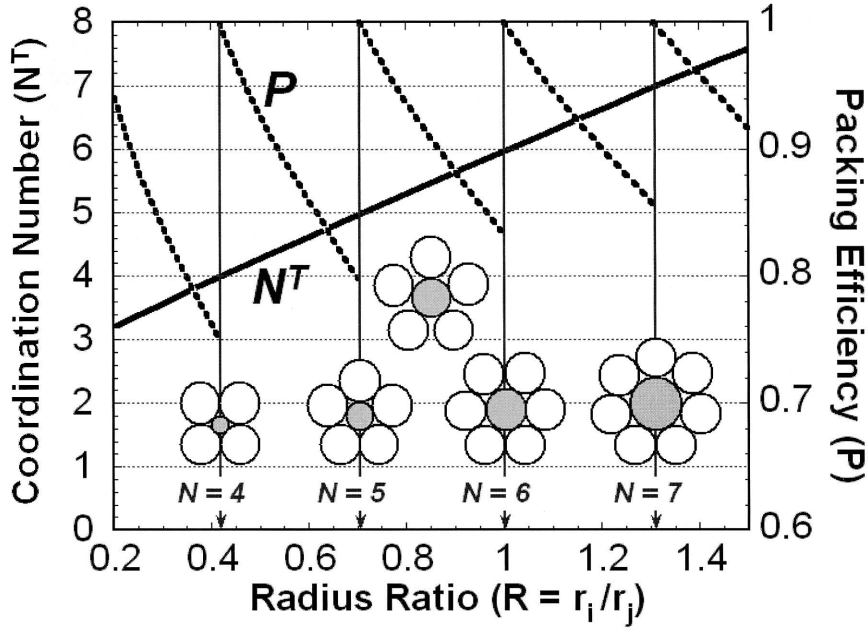

Figure 2. The theoretical coordination number N^T (——) and packing efficiency P (- - - -) as functions of radius ratio R for two-dimensional clusters of circles. Four two-dimensional configurations representing a packing efficiency of 1.0 are shown, with $R_4^* = 0.414$, $R_5^* = 0.701$, $R_6^* = 1.000$ and $R_7^* = 1.305$. A cluster with a packing efficiency less than one is also shown.

Since equation (2) represents an upper bound, $N(R)$ for known clusters should not exceed this bound. However, icosahedral clusters with $N = 12$ exist for $R = 0.902$, while equation (2) provides an N^T of only 11.27. An improved determination of $N^T\{R\}$ is thus required for a more accurate determination of the values R_N^* and is provided below.

The surface area of the central i sphere that is associated with a contacting specific reference j sphere j_{ref} in the first coordination shell is determined. A tessellation is performed on the curved surface of i. This requires a determination of the surface coordination number q (Frank and Kasper 1958) defined as the number of j spheres in the first coordination shell of i which also contact j_{ref}. The maximum value of q depends on the curvature of the surface upon which the coordination shell is arranged. For i of infinite radius (i.e. for a flat surface where $R = r_i/r_j = \infty$), a maximum of six j spheres may contact j_{ref} and i simultaneously. For $R \leqslant \infty$, the maximum number of j spheres in the first coordination shell that may simultaneously contact j_{ref} and i decreases to five. These five j spheres will, in general, be separated from one another and may be equally spaced about j_{ref}. As R decreases further, the five j spheres will become closer to one another until a critical value of R is reached where the five j spheres just touch one another in a continuous ring that girdles j_{ref} and i, while also contacting both j_{ref} and i. The radius ratio where this occurs will be shown later to be $R = 0.902$, producing a portion of an unstrained icosahedron.

As R decreases from this value, the maximum value of q drops to 4. Again, these four spheres all touch j_{ref} and i, but, if evenly spaced about j_{ref}, do not touch one another until a critical radius ratio $R = 0.414$ is reached, producing a portion of an

unstrained octahedron. Similarly, for $0.225 \leqslant R < 0.414$, a maximum of three spheres may contact any particular j_{ref} sphere; a value of $R = 0.225$ results in an unstrained tetrahedron. A further decrease in R produces a continued drop in q, resulting in planar or one-dimensional configurations that will not be considered here.

The surface coordination number q influences the area that is associated with j_{ref}, as illustrated in figure 3. The reference j sphere, j_{ref}, is shown directly above the smaller i (outlined by a broken circle), and q additional j spheres contact both j_{ref} and i, where $q = 3$ (figure 3 (*a*)), $q = 4$ (figure 3 (*b*)) or $q = 5$ (figure 3 (*c*)). The area on the curved surface of i that is associated with j_{ref} is obtained by constructing imaginary planes that are perpendicular bisectors of lines drawn from the centre of j_{ref} to the centres of each of the j spheres which contact j_{ref}. The intersections of these imaginary planes and the surface of i produce a series of great circles that bound the area on the curved surface that is associated with j_{ref}. This area, A_q, is illustrated on the expanded views of i in figure 3. The surface of i is wholly accounted for by the areas associated with each j atom thus determined. The maximum coordination number N^T is obtained from the minimum area associated with j_{ref}, which is obtained for the maximum possible value of q for the given radius ratio R.

N^T is determined by dividing the total surface area A_i of i by A_q. Assuming that the j spheres are symmetrically disposed about j_{ref}, A_q is given as $2q\ A_{triangle}$, where $A_{triangle}$ is the area of the spherical triangle bounded by the vertices O, B and C (figure 3). Thus

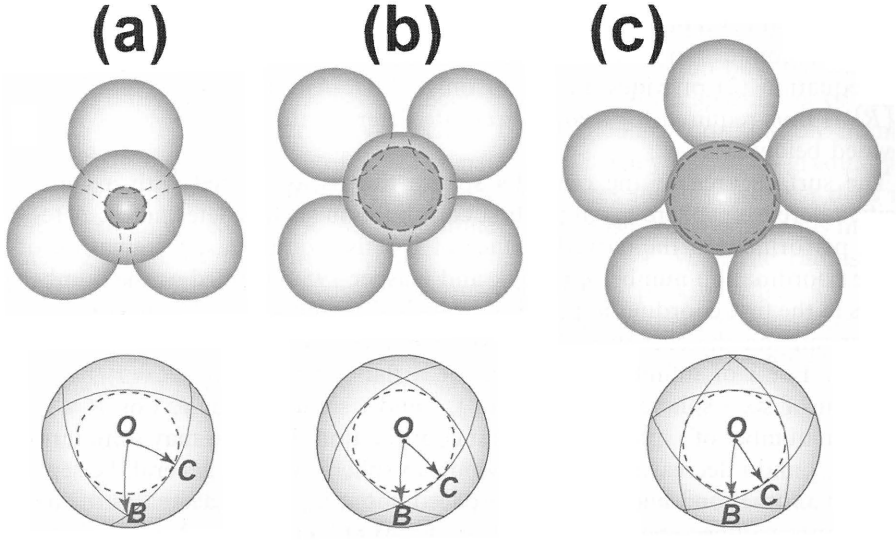

Figure 3. Images illustrating a reference j sphere j_{ref} in the first coordination shell that simultaneously contacts a smaller central i atom and (a) three, (b) four and (c) five other j spheres in the first coordination shell. The smaller i sphere defines the centre of the cluster and is shown directly below the semitransparent j_{ref}. The surface area A_q, on i that is associated with j_{ref} is illustrated in the enlarged images of i below each partial cluster. For a given radius ratio $R = r_i/r_j$ this area decreases as q increases from 3 to 5.

$$N^{\mathrm{T}} = \frac{2\pi}{q(\alpha_q + \beta_q - \pi/2)}, \tag{3}$$

where $\alpha_q = \pi/q$ is the angle at vertex O, and β_q, the angle at vertex B, is given as

$$\beta_q = \arccos\left[\sin(\alpha_q) \cdot \cos(\overline{\mathrm{OC}})\right] = \arccos\left[(\sin\alpha_q)\left(1 - \frac{1}{(R+1)^2}\right)\right], \tag{4}$$

so that the final relation is given as

$$N^{\mathrm{T}} = \frac{4\pi}{\pi(2-q) + 2q\arccos\{\sin\pi/q)[1 - 1/(R+1)^2]^{1/2}\}}. \tag{5}$$

The critical radius ratios where a change in the maximum possible q occurs can be determined by noting that the critical configuration is reached when all q of the j spheres that contact j_{ref} also contact each of their neighbours in the ring, thus forming q equilateral triangles with j_{ref}. Geometrical analysis of this configuration gives the critical radius ratios for transition from q-fold surface coordination to $q-1$;

$$R^*_{q\to(q-1)} = \left(\frac{1}{1 - 1/[4\sin^2\pi/q]}\right)^{1/2} - 1. \tag{6}$$

Thus, the transition from sixfold to fivefold surface coordination occurs for $R^*_{6\to5} < \infty$, the fivefold-to-fourfold transition occurs at $R^*_{5\to4} = 0.902$, the fourfold-to-threefold transition occurs at $R^*_{4\to3} = 0.414$, and the break from threefold to twofold coordination occurs at $R^*_{3\to2} = 0.225$.

Combining equations (3)–(5), together with the coordination transitions from equation (6), gives the following final dependence of N^{T} on R:

$$N^T = \begin{cases} \dfrac{4\pi}{6\arccos\{\sin(\pi/3)[1 - 1/(R+1)^2]^{1/2}\} - \pi} & \text{for } 0.225 \leqslant R < 0.414, \quad (7a) \\ \dfrac{4\pi}{8\arccos\{\sin(\pi/4)[1 - 1/(R+1)^2]^{1/2}\} - 2\pi} & \text{for } 0.414 \leqslant R < 0.902, \quad (7b) \\ \dfrac{4\pi}{10\arccos\{\sin(\pi/5)[1 - (1/(R+1)^2]^{1/2}\} - 3\pi} & \text{for } 0.902 \leqslant R. \quad (7c) \end{cases}$$

The results of equation (5) are plotted in figure 4 for $q = 3$, 4, and 5, together with the results from the work of Egami (1997). The final dependence of N^{T} on R (equations (7*a*)–(7*c*)), which shows that an explicit account of the surface coordination is required for a complete description of the relation between R and N^{T}, is shown by the bold curves. A discontinuous change in N^{T} occurs at the transitions from q-fold surface coordination to $q-1$. At $R = 0.902$, where the maximum surface coordination decreases from 5 to 4, a discontinuous decrease in N^{T} of about 0.8 occurs, and at $R = 0.414$, where the maximum surface coordination decreases from 4 to 3, a discontinuous decrease in N^{T} of about 0.6 results. Egami's estimate provides a good match with the current calculations below $R = 0.902$ but is lower than the current N^{T} values by nearly unity above this transition. The current calculation of N^{T} provides an exact solution for the

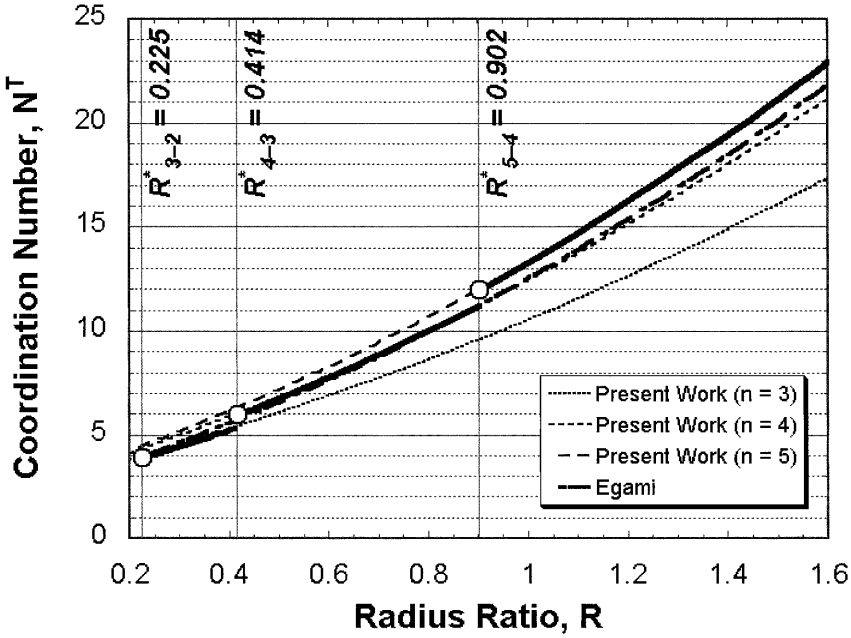

Figure 4. The dependence of the theoretical maximum coordination number N^{T} on the radius ratio $R = r_i/r_j$ as a function of the surface coordination number q of j spheres that contact a specific reference j sphere, j_{ref}, in the first coordination shell; the critical values of R where the maximum possible surface symmetry changes from R_N^* to R_{N-1}^* are shown: (——), expected dependence of N^{T} on R for actual three-dimensional sphere clusters, with discontinuities at these critical values of R; (○) known geometric clusters for icosahedra ($R = 0.902$), octahedra ($R = 0.414$) and tetrahedra ($R = 0.225$). The earlier relation from Egami (1997) is also shown.

known boundary values of coordination numbers for tetrahedra ($N = 4$ at $R = 0.225$), octahedra ($N = 6$ at $R = 0.414$) and icosahedra ($N = 12$ at $R = 0.902$).

The three-dimensional values of local packing efficiency, obtained by the simple representation N/N^{T} (figure 5), are generally higher than for two-dimensional clusters (figure 2). Further, packing becomes more efficient as R increases. This is consistent with the concept that higher packing efficiency can be achieved for clusters of smaller spheres around a larger sphere than for larger spheres around a smaller sphere. As for clusters in two dimensions, it is clear that the maximum local packing efficiency in three dimensions will be obtained only for a specific set of distinct radius ratios, R_N^*, where the value of N^{T} is an integer.

2.3. *Critical radius ratios for maximum packing efficiency*

As described in the previous section, a maximum packing efficiency in the first coordination shell is obtained at those specific values of R that produce an integer value of N^{T}, defined as R_N^*. These values, obtained from equation (7), are given in table 1. A clear asymmetry exists in the values of R^*. The slope of dN^{T}/dR increases as R and q increase, so that the separation between values of R^* is smaller above $R = 0.902$. The values of R_{11}^* and R_{12}^* occur near the transition from fourfold to fivefold coordination, and are similar in magnitude.

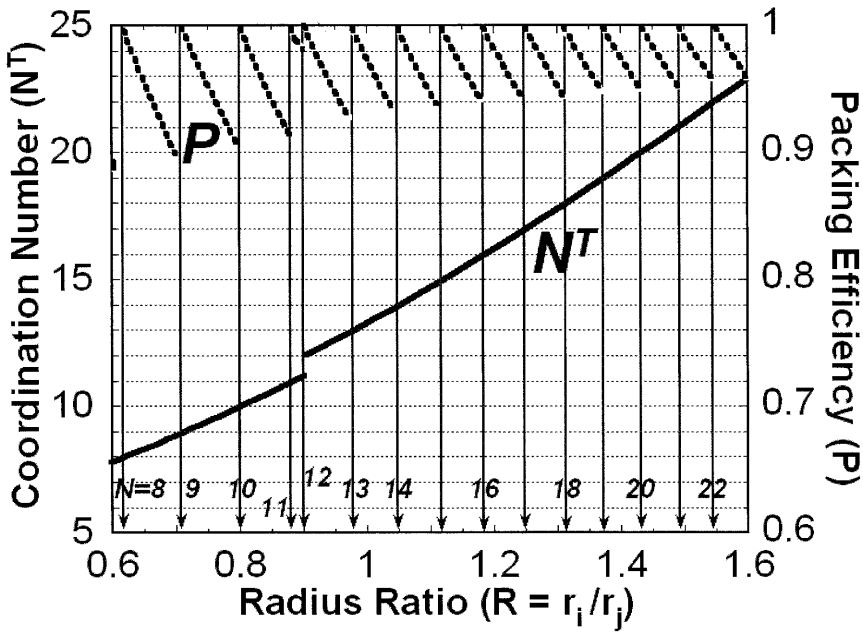

Figure 5. The theoretical coordination number N^T (——) and packing efficiency P (- - - -) as functions of radius ratio R for three-dimensional clusters of spheres. A discontinuity occurs where the maximum surface coordination increases from $q = 4$ for $R < 0.902$ to a maximum surface coordination of $q = 5$ for $R = 0.902$. A maximum packing efficiency occurs for discrete values of R^* where N^T is an integer. These specific radius ratios are shown by the vertical lines, and the associated coordination numbers are also shown.

Table 1. Values of R_N^* and corresponding values of N.

N	R_N^*	N	R_N^*
3	0.155[a]	14	1.047
4	0.225	15	1.116
5	0.362	16	1.183
6	0.414	17	1.248
7	0.518	18	1.311
8	0.617	19	1.373
9	0.710	20	1.433
10	0.799	21	1.491
11	0.884	22	1.548
12	0.902	23	1.604
13	0.976	24	1.659

[a] Calculated from equation (1).

§ 3. Packing efficiency in metallic glasses: experimental observations

The foregoing suggests that the local structure of metallic glasses may be efficiently packed in systems where the solutes occur at fixed radius ratios R^*. To determine whether metallic glasses display a preference for these specific values of R^*, the radius ratios $R = r_i/r_j$ (r represents atomic radius and the subscripts i and j used earlier and throughout the rest of the manuscript indicate the solute and solvent

atoms respectively) for a significant number of binary and complex (ternary or higher-order) metallic glasses are catalogued. We considered 76 binary alloys from a list provided by Egami and Waseda (1984), to which several metallic glasses based on Al, Au and Si have been added (table 2). Alloy composition is not important in the current comparison, and so only values of R are reported. Atomic radii are generally taken from the work of Egami and Waseda (1984); exceptions are noted in table 2. A discussion of the determination of r is provided in the following section.

Table 2. Binary metallic glass alloy systems. Atomic radii from Egami and Waseda (1984) except for Ce, Dy, Er, Na and Y from Inoue (2000).

System i–j	r_i (nm)	r_j (nm)	R	System i–j	r_i (nm)	r_j (nm)	R
Ag–Mn	0.142	0.132	0.930	Mg–Zn	0.160	0.138	0.863
–Si	0.142	0.102	0.718	–Zr	0.160	0.158	0.988
Al–Ce	0.143	0.182	1.273	Mn–Si	0.132	0.102	0.773
–Cu	0.143	0.127	0.888	Na–Ag	0.185	0.142	0.768
–Er	0.143	0.176	1.231	–Au	0.185	0.145	0.784
–Gd	0.143	0.174	1.217	–Cu	0.185	0.127	0.686
–La	0.143	0.187	1.308	–Ga	0.185	0.132	0.714
–Y	0.143	0.180	1.259	–Ge	0.185	0.114	0.616
Au–Ge	0.145	0.114	0.786	–Ni	0.185	0.128	0.692
–Pb	0.145	0.175	1.207	Nb–Ni	0.146	0.128	0.877
–Si	0.145	0.102	0.703	Ni–B	0.128	0.078	0.609
–Sn	0.145	0.162	1.117	–Dy	0.128	0.177	1.383
Ca–Ag	0.197	0.142	0.721	–Hf	0.128	0.167	1.305
–Al	0.197	0.143	0.726	–P	0.128	0.100	0.781
–Cu	0.197	0.127	0.645	–Ta	0.128	0.149	1.164
–Ga	0.197	0.132	0.670	–Zr	0.128	0.158	1.234
–Mg	0.197	0.160	0.812	Pb–Au	0.175	0.145	0.829
–Zn	0.197	0.138	0.701	Pd–Ge	0.141	0.114	0.809
Co–Au	0.128	0.145	1.133	–Si	0.141	0.102	0.723
–B	0.128	0.078	0.609	Pt–Ge	0.138	0.114	0.826
–Hf	0.128	0.167	1.305	–P	0.138	0.100	0.725
–P	0.128	0.100	0.781	–Si	0.138	0.102	0.739
–Ti	0.128	0.146	1.141	Rh–Si	0.134	0.102	0.761
–Zr	0.128	0.158	1.234	Th–Fe	0.180	0.128	0.711
Cu–Ti	0.127	0.146	1.150	Ti–Be	0.146	0.112	0.767
–Zr	0.127	0.158	1.244	–Ni	0.146	0.128	0.877
Fe–B	0.128	0.078	0.609	–Si	0.146	0.102	0.699
–C	0.128	0.077	0.602	U–Co	0.158	0.128	0.810
–Gd	0.128	0.174	1.359	–Fe	0.158	0.128	0.810
–Hf	0.128	0.167	1.305	–Mn	0.158	0.132	0.835
–P	0.128	0.100	0.781	–Ni	0.158	0.128	0.810
–Zr	0.128	0.158	1.234	–V	0.158	0.134	0.848
Gd–Al	0.174	0.143	0.822	Y–Ni	0.180	0.128	0.711
–Cu	0.174	0.128	0.736	Zr–Al	0.158	0.143	0.905
–Fe	0.174	0.128	0.736	–Be	0.158	0.112	0.709
Hf–Co	0.167	0.128	0.766	–Co	0.158	0.128	0.810
–Ni	0.167	0.128	0.766	–Cu	0.158	0.127	0.804
La–Al	0.187	0.143	0.765	–Fe	0.158	0.128	0.810
–Au	0.187	0.145	0.775	–Ni	0.158	0.128	0.810
–Ni	0.187	0.128	0.684	–Pd	0.158	0.141	0.892
Mg–Ca	0.160	0.197	1.231	–Rh	0.158	0.134	0.848
–Ga	0.160	0.132	0.825	–Si	0.158	0.102	0.646

The binary glasses include combinations of simple metals, noble metals, early and late transition metals and rare-earth metals, so that a wide range in chemical bonding is represented. Each binary alloy produces a single value of R, and a histogram of the resulting values is produced. Rather than reporting R values as delta functions and summing the occurrences within an interval ΔR, each value is represented as a Gaussian curve with a standard deviation of 1.5% and an area under the curve of unity. This distribution in R accounts for some uncertainty in r. The 76 individual Gaussian distributions are then summed to provide the final histogram.

The histogram of the frequency with which specific values of R are observed for the binary alloys in table 2 is shown in figure 6(*a*). The vertical axis indicates the frequency with which a given R occurs, and the vertical lines illustrate the values of R^* from table 1 for which efficient atomic packing is predicted. The coordination number N, which corresponds to each vertical line, is indicated by the subscript in the labelled value of R_N^*. A strong correlation is shown between the predicted values of

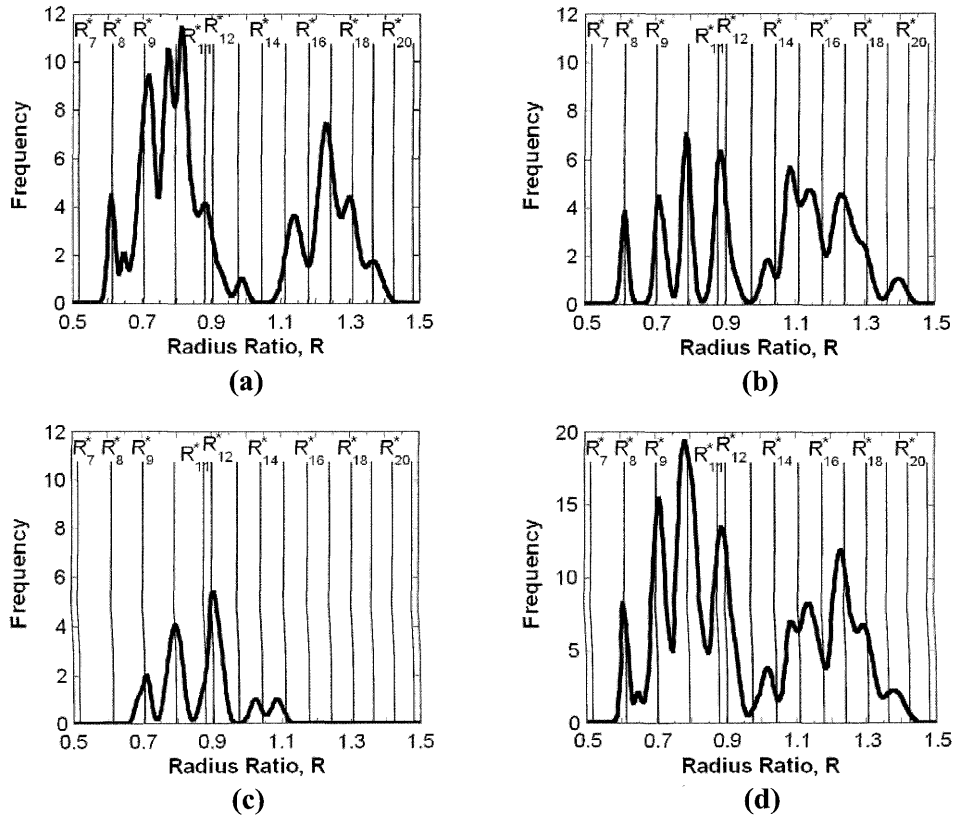

Figure 6. Histograms of the radius ratios R that occur in the metallic glass alloys in tables 2–4, superimposed on a graph illustrating the critical radius ratios, R_N^*, predicted for efficient atomic packing (as indicated by the vertical lines). The coordination numbers N which correspond to each value of R_N^* are indicated by the labelled subscripts. The histograms represent data for (*a*) binary metallic glasses from table 2, (*b*) complex marginal metallic glasses from table 3, (*c*) complex bulk metallic glasses from table 4 and (*d*) a composite of all metallic glasses studied here.

R^* and the values of R that exist for the wide range of binary metallic glasses considered. Deviations from the predicted values include an extra 'peak' at $R = 0.645$ and an anticorrelation for the peak at $R = 1.15$. The strongest peak is centred at $R = 0.80$, and this is split into two subpeaks which fall just on either side of the predicted value of $R^* = 0.799$.

Similar histograms generated for complex metallic glasses are shown in figures 6(*b*) and (*c*). The 16 metallic glass systems in table 3 and 4 include marginal (critical cooling rate, $10^3\,\mathrm{K\,s^{-1}}$ or greater) and bulk (critical cooling rate, $10^3\,\mathrm{K\,s^{-1}}$ or less) glasses. Alloy systems were selected from those cited by Inoue (2000). To prevent a bias toward specific values of R resulting from multiple citations of similar alloy compositions within a distinct alloy family, a particular combination of elements was

Table 3. Multinary metallic glass alloy systems. Atomic radii from Egami and Waseda (1984) and Inoue (2000)

System i–j	r_i (nm)	r_j (nm)	R
Fe–(Al, Ga)–(Ge, Si, P, B, C)			
Fe–Al	0.128	0.143	1.117
–Ga	0.128	0.132	1.031
–Ge	0.128	0.114	0.891
–Si	0.128	0.102	0.797
–P	0.128	0.100	0.781
–B	0.128	0.078	0.609
–C	0.128	0.077	0.602
(Fe, Ni)–Zr–Hf–Nb–Ta–Mo–Cr–P–B			
Fe–Zr	0.128	0.158	1.234
–Hf	0.128	0.167	1.305
–Nb	0.128	0.146	1.141
–Ta	0.128	0.149	1.164
–Mo	0.128	0.139	1.086
–Cr	0.128	0.130	1.016
–P	0.128	0.100	0.781
–B	0.128	0.078	0.609
Ni–Zr	0.128	0.158	1.234
–Hf	0.128	0.167	1.305
–Nb	0.128	0.146	1.141
–Ta	0.128	0.149	1.164
–Mo	0.128	0.139	1.086
–Cr	0.128	0.130	1.016
–P	0.128	0.100	0.781
–B	0.128	0.078	0.609
Mg–(Cu, Ni)–(Y, Gd, Ce, La)			
Mg–Cu	0.160	0.127	0.794
–Ni	0.160	0.127	0.794
–Y	0.160	0.174	1.088
–Gd	0.160	0.174	1.088
–Ce	0.160	0.182	1.138
–La	0.160	0.187	1.169
Al–(Fe, Ni)–(Y, Gd, Ce)			
Al–Fe	0.143	0.128	0.895
–Ni	0.143	0.128	0.895
–Y	0.143	0.174	1.217
–Gd	0.143	0.174	1.217
–Ce	0.143	0.182	1.273
Ti–Zr–(Co, Cu, Fe, Ni)–Sn			
Ti–Zr	0.146	0.158	1.082
–Co	0.146	0.128	0.877
–Cu	0.146	0.127	0.870
–Fe	0.146	0.128	0.877
–Ni	0.146	0.128	0.877
–Sn	0.146	0.162	1.110
Au–Ge–Si			
Au–Ge	0.145	0.114	0.786
–Si	0.145	0.102	0.703
Sm–(Co, Cu, Fe)–Al			
Sm–Co	0.181	0.128	0.707
–Cu	0.181	0.127	0.702
–Fe	0.181	0.128	0.707
–Al	0.181	0.143	0.790
Pt–Ni–P			
Pt–Ni	0.138	0.128	0.928
–P	0.138	0.100	0.725
Pd–Cu–Si			
Pd–Cu	0.141	0.127	0.901
–Si	0.141	0.102	0.723
Si–(Fe, Ni)–Al			
Si–Fe	0.102	0.128	1.255
–Ni	0.102	0.128	1.255
–Al	0.102	0.143	1.402

Table 4. Bulk metallic glass alloy systems. Atomic radii from Egami and Waseda (1984) and Inoue (2000).

System i–j	r_i (nm)	r_j (nm)	R	System i–j	r_i (nm)	r_j (nm)	R
Zr–Ti–Nb–Al–Pd–Ni–Cu–Be				*La–Al–Ni*			
Zr–Ti	0.158	0.146	0.924	La–Al	0.143	0.128	0.895
–Nb	0.158	0.146	0.924	–Ni	0.143	0.128	0.895
–Al	0.158	0.143	0.905				
–Pd	0.158	0.141	0.892	*Mg–Cu–Y*			
–Ni	0.158	0.128	0.810	Mg–Cu	0.160	0.127	0.794
–Cu	0.158	0.127	0.804	–Y	0.160	0.174	1.088
–Be	0.158	0.112	0.709				
				Nd–(Fe, Ni)–Al			
Pd–(Cu, Fe, Ni)–P				Nd–Fe	0.164	0.128	0.780
Pd–Cu	0.141	0.128	0.908	–Ni	0.164	0.128	0.780
–Fe	0.141	0.128	0.908	–Al	0.164	0.143	0.872
–Ni	0.141	0.128	0.908				
–P	0.141	0.100	0.709	*Mg–Ni–Nd*			
				Mg–Ni	0.160	0.128	0.800
				–Nd	0.160	0.164	1.025

counted only once, regardless of the number of alloy compositions reported within that family. Thus, although a significant number of distinct ternary compositions are reported for amorphous Al–Ni–Y alloys, the radius ratios r_Y/r_{Al} and r_{Ni}/r_{Al} were tabulated only once in the histograms in figures 6(*b*) and (*d*). Further, although a given solute, such as Ni, may occur in a number of similar alloys in a family of metallic glasses (such as Al–Ni–Y, Al–Ni–La and Al–Ni–Ce in the Al–transition-metal–rare-earth family), the radius ratio r_{Ni}/r_{Al} was only counted once. Although it may be argued that each chemically distinct permutation of elements should be counted separately for the purpose of the present comparison, the approach selected here will provide a conservative estimate of the frequency with which specific radius ratios occur in metallic glasses.

Excellent correlation is observed between the predicted values of R^* and observed values for marginal glasses, especially for $R < 1$ (figure 6(*b*)). The two major peaks for $R > 1$ are rather broad and are centred on values of R^*, while two minor peaks show less perfect correlation with predictions. The largest peak, centred on $R = 1.116$, shows one subpeak above and one subpeak below this central value. The three major peaks of bulk metallic glasses (figure 6(*c*)) agree very well with predicted values of R^*, while two minor peaks display a poor correlation. The radius ratios are typically less than 1, illustrating that solutes are generally smaller than the solute in the best metallic glasses (Miracle and Senkov 2001, Senkov and Miracle 2001). A summation of the histograms in figures 6(*a*)–(*c*) is shown in figure 6(*d*). The major peaks show very good agreement with predicted radius ratios. A major peak near $R = 1.116$ may be split into two subpeaks, and poor correlation is obtained for peaks near $R = 1.02$ and 1.38. A minor peak at $R = 0.645$ falls midway between two values of R^*.

An ASDP for six representative silicate and borosilicate glasses is provided to explore the generality of the model developed here (figure 7). The cation sizes were taken as the ionic radii determined at the appropriate coordination numbers

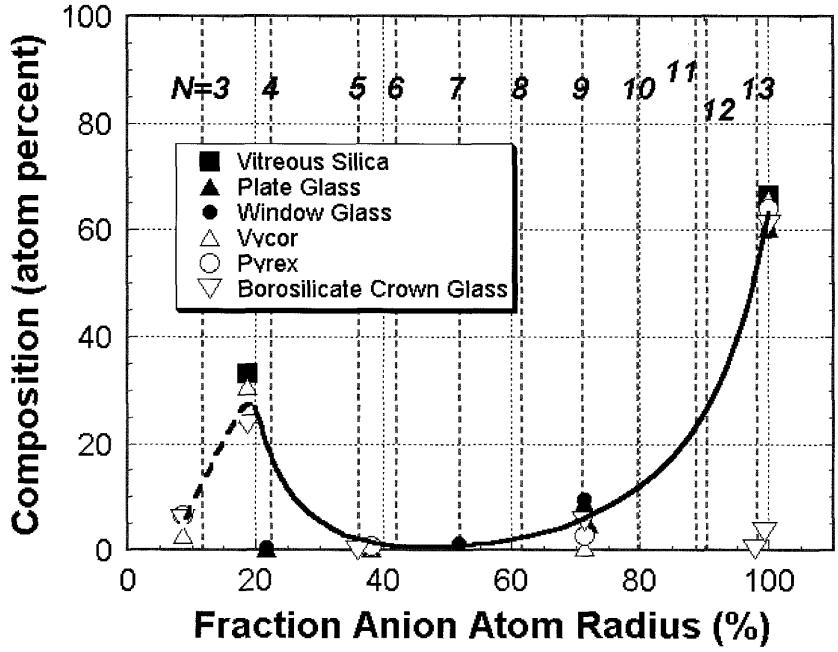

Figure 7. ASDP for six common silicate and borosilicate glasses, where the solute ion radius ratios closely match the values of R^*, shown by the vertical dotted lines in the figure, predicted for efficient atomic packing in the first coordination shell: (■), (▲), (●), silicate glasses; (△), (○), (▽), borosilicate glasses.

(Kingery *et al.* 1975). The anion radius was taken as 140 pm for $N > 4$, and a value of 130 pm was used for $N \leqslant 4$ (see table 3.3 in Varshneya (1993)). The methodology for constructing this plot has been described elsewhere (Miracle and Senkov 2001, Senkov and Miracle 2001). The solute ions occur very close to the predicted values of R^*, suggesting that the model of high packing efficiency developed here is a general feature of amorphous solids and is not restricted to metallic glasses alone. This view is supported by earlier analysis of atomic packing in ionic amorphous solids (Lines 1979, Hannemann *et al.* 2002).

§4. Discussion

Overall, the correlation is very strong between the predicted radius ratios for high packing efficiency in the first coordination shell and the histograms of R in metallic glasses. The metallic glasses from which this agreement is obtained span a broad range in metal types, so that chemical effects are not expected to produce the trends observed here. Further, good agreement is obtained for binary and complex glasses and for marginal and bulk metallic glasses. Finally, these alloys were discovered using different, empirically based exploration strategies from different research groups, spanning nearly four decades of research. Given these variations, the current agreement is remarkable and provides strong support for the unifying concept that a high atom packing efficiency is a fundamental principle in the formation of metallic glasses. The agreement between the predicted values of R^* and the ionic radius ratios observed in a range of common silicate and borosilicate glasses

further strengthens support for this model and shows that the model may be broadly relevant to ionic and covalent amorphous solids.

Efficient atomic packing produces a smaller system volume, reducing the volume energy associated with an atomic ensemble and providing a physical basis for this concept. From a kinetic perspective, efficiently packed atoms are expected to produce a highly viscous melt. Mass transport, required for nucleation and growth of critical crystalline clusters, is dramatically reduced, since diffusivity is inversely related to viscosity through the Stokes–Einstein relation. It has been suggested (Gaskell 1983) that particular atomic configurations that conserve, or minimize, space will be preferred in the structure of a metallic glass, consistent with the predictions here. Analysis of 35 binary alloys has shown that the minimum in molar volume invariably occurred within the experimentally observed composition range of glass formation (Ramachandraro 1980). In more recent work on Pd-based metallic glasses, it has also been shown that the best glass-forming compositions coincide with the minimum system molar volume (Jin *et al.* 2000). Each of these observations supports the present view that efficient atomic packing is a fundamental consideration in the formation of metallic glasses.

The prediction of a set of distinct radius ratios R^*, preferred for the formation of metallic glasses, is an important extension of earlier efforts to describe the role of topology. The widely cited requirement that solutes must be larger or smaller than the solvent atoms by at least 12% (Inoue 2000) shows good agreement with the model developed here. The values of $R^* = 0.884$ $(N = 11)$ and $R^* = 1.116$ $(N = 15)$ accurately represent bounds of $\pm 12\%$. The value of $R^* = 0.902$ $(N = 12)$ is in marginal agreement with this guideline. Uncertainties in the radii of constituent elements introduce some ambiguity in the precise value of R (see the discussion below and in appendix A of the paper by Egami and Waseda (1984)) and may explain this narrow discrepancy. Although two values of R^* are significantly smaller than the 12% bound ($R^* = 0.976$ for $N = 13$ and $R^* = 1.047$ for $N = 14$), the model described by Egami and Waseda (1984) suggests that the critical concentration of solutes for these sizes would be too large to be observed experimentally as a solute addition. Both the model by Egami and Waseda (1984) and the ASDPs of Senkov and Miracle (2001, 2003) provide relationships between atom radius ratios and solute concentrations. The current result of specific preferred radius ratios is consistent with both of these models, but provides a more specific criterion. Close observation of ASDPs (see, for example, figure 7 in the present work and figures 1 and 4 in the paper by Senkov and Miracle (2001)) illustrates the preference for values of R^*.

The present model relies upon an idealization that considers the structure of amorphous metals to be represented by solute-centred clusters, where the first coordination shell is occupied only by solvent atoms. This condition is satisfied in silicate glasses, where Si cations are surrounded by O anions in tetrahedral clusters, and in metal–metalloid glasses, where solvent atoms surround metalloid solutes in a capped trigonal prismatic cluster. Metalloid–metalloid bonding is rare (Gaskell 1983), although infrequent metalloid–metalloid bonding may occur (Cowlam 1996). The strong covalent Si—O bond and the strong preference for metal–metalloid bonding favour solute-centred clusters surrounded only by solvent atoms. Diffraction data also suggest that transition-metal solutes are rarely first-nearest neighbours in Al-based metallic glasses (Matsubara *et al.* 1989). However, it is not expected that this will generally be the case in metallic glasses, especially in alloys with predominantly

metallic bonding. Solute–solute nearest-neighbour bonding is reported for Ti–Ni (Fukunaga *et al.* 1984), Cu–Zr (Lamparter *et al.* 1983), Zr–Ni (Lee *et al.* 1984), Zr–Be (Maret *et al.* 1984), Tb–Fe (Fukunaga *et al.* 1984) and Fe–Gd (Cargill 1974). Solute–solute bonding is also observed in Al–Y alloys, but drops to within experimental error for Al–Y–Ni alloys (Matsubara *et al.* 1989), which have better glass-forming ability. Partial coordination numbers obtained from high-quality diffraction data are not widely available to determine nearest-neighbour occupancy in complex metallic glass alloys. An approach for exploring the degree of short-range chemical ordering in amorphous metals has been described previously (Cargill and Spaepen 1981), and additional work in this area may provide useful insights into the importance of this feature in the formation and structure of metallic glasses.

Some care is required in the selection of atomic radii, since these values can vary with local structure and chemistry. This effect is significant in ionically bonded structures but is not a major factor in systems where metallic bonding dominates. A critical analysis of atom radii has been conducted (see appendix A in the paper by Egami and Waseda (1984)), and the values thus obtained are generally quite similar to handbook values. Significant differences between handbook and assessed values are noted in the covalent metals Si and Ge, and in early transition metals with significant d-orbital bonding. In addition, an element may display a range of radii depending on the bond formed with other elements in the alloy. For example, a portion of the Al—Ni bond is of covalent character, resulting in bond shortening relative to the metallic radii. It is difficult to ascribe a specific portion of this Al—Ni bond to Al and to Ni. In the present analysis, radius ratios were represented as a Gaussian distribution rather than a delta function to acknowledge and account for this possible variation.

The use of hard spheres provides a simplification for the determination of R^*, and the excellent agreement between the predicted and observed values in a wide range of metallic glasses strengthens this assumption. However, soft spheres may accommodate local contacts more effectively, leading to more efficiently packed configurations. Computer simulations using soft atomic potentials have shown good agreement with experiment (Finney 1977), and it is likely that such a representation is broadly applicable in amorphous metals. The use of hard spheres is not a required feature of this model, and extension to soft atomic spheres is conceptually straightforward. It is likely that values of R^* obtained for soft spheres will be slightly different than those provided by hard spheres.

In general, there are $x(x-1)$ radius ratios in an alloy with x elements, neglecting ratios of unity for the coordination of an element around itself. There are two radius ratios in a binary alloy, but r_i/r_j will dominate, since it is far more likely to obtain a solute atom surrounded by solvent atoms than it is to have a solvent atom surrounded by solutes. There are six distinct radius ratios for a ternary alloy, which reduce to a smaller number of statistically probable ratios, depending upon the atomic concentration of each element in the alloy. Efficiently packed configurations can certainly be obtained with multiple atomic species in the first coordination shell; in principle, this can be achieved with combinations of atom ratios that do not match values of R^*. Nevertheless, the fact that this simple model provides such a striking correlation with complex systems suggests that the basic assumption of solvent atoms only in the first coordination shell is a valid simplification.

This model imposes a crude relationship between solute and solvent concentrations. Assuming that each solvent atom is coordinated with two solute atoms, the

solvent concentration C_j, is roughly half the product of the solute concentration and the coordination number N_{ij} of solvent atoms around a solute atom:

$$C_j \approx \frac{N_{ij} C_i}{2}. \tag{8}$$

This bound is satisfied for silica glass, where $C_i = 0.33$ and $N_{ij} = 4$ and is roughly approximated in metal–metalloid glasses, where $C_i \approx 0.18$–0.2 and $N_{ij} \approx 8.5$–9.

Although the present work provides insight into the local atomic configurations that may exist, it is not the purpose here to propose a structural model for metallic glasses. Nevertheless, some comments relating to features expected in such a structure may be made. As an idealization, it is unlikely that the structure will consist primarily of well-defined specific atomic clusters. Rather, significant distortions from idealized positions are expected as a result of atomic substitutions in the first coordination shell and displacements to accommodate the local structure of adjacent atoms and clusters. Soft atoms may help to accommodate these elastic and inelastic displacements. This model focuses on efficient packing of solvent atoms around solute atoms. The first coordination shell around solvent atoms, however, will in general contain both solvent and solute atoms, so that efficiently packed configurations may be more difficult to achieve. This is consistent with analysis of diffraction data for Al–Y–Ni (Miracle and Senkov 2003) and with positron annihilation studies in Zr-based glasses (Flores *et al.* 2002), which both show that packing around the solvent atoms can be notably less efficient than elsewhere in the structure. While it is tempting to consider structure beyond the first coordination shell to be described by a simple linking of atomic clusters, an alternative viewpoint is one of interpenetrating clusters. Since the intersolute spacing is about 2 atoms centre to centre, two nearest-neighbour solutes will in general be separated by common solvent atoms. The first coordination shell around a solvent atom will include these two solutes. Thus, analysis of the local environments obtained from (globally averaged) diffraction data will provide redundant information that must be viewed from this perspective. Experimental data of sufficiently high information content are in general not available, but careful analysis of atomic configurations obtained via computations may provide an approach for exploring these possibilities.

The concepts developed here for the efficient packing in amorphous solids are in consonance with a great deal of earlier work regarding the packing of atoms in crystalline solids (for example Frank and Kasper (1958) and Nelson and Spaepen (1989)). The most relevant work is a description of complex crystalline structures in transition-metal compounds based on efficient sphere packing (Frank and Kasper 1958). However, the constraint in that work of atomic clusters that form polyhedra with only triangular faces is relaxed in the current work, so that additional, relatively less efficiently packed configurations may be considered.

The overall packing efficiency in silicate glasses is low, since adjacent SiO_4 tetrahedral clusters are joined by vertices. Nevertheless, packing is very efficient on a length scale that encompasses the first coordination shell of Si ions. Thus, the radius ratio for the primary solute (Si) is close to that required for an ideal tetrahedral interstice ($R^* = 0.225$). In fact, network-forming elements are generally understood to stabilize tetrahedral and planar trigonal clusters of solvent ions depending upon the cation-to-anion radius ratios as stated in Zachariasen's rules and Pauling's rules (Wells 1984, Hannemann *et al.* 2002). Although other network-forming, intermediate and network-modifying elements are often too large to stabilize tetra-

hedral or octahedral clusters, they nevertheless exist at radius ratios predicted very well in the current model. For example, Na and Ca ions ($R^* \approx 0.715$) represent capped trigonal prism clusters with $N = 9$. Structural models for silicate glasses are well established from chemical, topological and electrostatic perspectives. Thus, in addition to topology, structures depend explicitly on ion valency, preferred bond angles (for covalent bonding) and minimization of electrostatic interactions (Pauling 1960, Wells 1984). Although the topological concepts discussed here may not be fully consistent with the accepted roles of solutes in the structure of silicate glasses, the excellent agreement with the current model provides an intriguing alternate perspective from a topological viewpoint.

§ 5. Summary

The high density of amorphous alloys, relative to the crystalline form of the same alloy, leads to the proposal that efficient atomic packing is a fundamental consideration in the constitution of metallic glasses. Previous efforts to explain the high relative density of amorphous metals based on dense random packing of atoms of different sizes have been unsuccessful. The approach taken here has been to explore the concept of efficient atomic packing based on atomic clusters consisting of a central solute atom surrounded by solvent atoms in the first coordination shell. The ratio R of the solute atom radius to the solvent atom radius is the only topological parameter considered. A simple analysis of this model leads to the conclusion that specific atomic radius ratios R^* provide efficient atomic packing over a length scale defined by these atomic clusters. This result extends earlier descriptions of the influence of topology on the formation of metallic glasses by providing a more specific set of conditions for metallic glass formation.

The values of R^* are calculated for solute-centred clusters using an analytical expression for the coordination number N^T of solvent atoms as a function of the radius ratio R. This expression is based on the packing of spheres on the curved surface defined by the solute atom and explicitly accounts for breaks in surface coordination with variation in R. The resulting expression provides an exact solution for well-known clusters such as tetrahedra ($R^* = 0.225$, $N^T = 4$), octahedra ($R^* = 0.414$, $N^T = 6$) and icosahedra ($R^* = 0.902$, $N^T = 12$). Values of R^* are provided for solute-centred clusters with between three and 24 solvent atoms in the first coordination shell. A large number of binary, ternary and higher-order metallic glasses have been analysed to explore the validity of the prediction of preferred radius ratios in the constitution of metallic glasses. The results show a clear preference for the predicted critical radius ratios R^* for all major classes of metallic glasses analysed. In addition, analysis of selected silicate glasses also shows strong support for the critical radius ratios predicted on the basis of efficient atomic packing in the first coordination shell. Neither the specific atomic configurations that produce these efficiently packed local atomic clusters nor the structural features of metallic glasses on a length scale beyond the first coordination shell are specified in this work.

The following major results and conclusions are drawn from this work.

(1) Efficient atomic packing in the first coordination shell is a fundamental consideration in the constitution of metallic glasses.
(2) Specific critical radius ratios R^* are predicted to provide efficient atomic packing in the first coordination shell of solute-centred atomic clusters.

(3) Analysis of a large number of metallic glass systems and a selected number of silicate glasses show a strong preference for these predicted critical radius ratios.

ACKNOWLEDGEMENTS

The authors would like to acknowledge encouraging comments by Professor W. Johnson and Professor T. Egami. This research was supported under the Defense Advanced Research Projects Agency Structural Amorphous Metals Initiative (Dr L. Christodoulou, Program Manager) and US Air Force Office of Scientific Research Task 01ML05-COR (Dr C. Hartley, Program Manager).

REFERENCES

BERNAL, J. D., 1964, *Proc. R. Soc.* A., **280**, 299.
CARGILL, G. S., 1974, *Magnetism and Magnetic Materials—1973,* AIP Conference Proceedings, Vol. 18 (New York: American Institute of Physics), p. 631.
CARGILL, G. S., and SPAEPEN, F., 1981, *J. non-crystalline Solids,* **43**, 91.
CLARKE, A. S., and WILEY, J. D., 1987, *Phys. Rev.* B, **35**, 7350.
COWLAM, N., 1996, *J. non-crystalline Solids,* **205–207**, 567.
DOUGHERTY, G. M., HE, Y., SHIFLET, G. J., and POON, S. J., 1994, *Scripta metall mater.,* **30**, 101.
EGAMI, T., 1997, *Mater. Sci. Engng*, **A226–A228**, 261.
EGAMI, T., AND WASEDA, Y., 1984, *J. non-crystalline Solids,* **64**, 113.
FINNEY, J. L., 1970, *Proc. R. Soc.* A, **319**, 479; 1977, *Nature,* **266**, 309.
FLORES, K. M., SUH, D., and DAUSKARDT, R. H., 2002, *J. Mater. Res.,* **17**, 1153.
FRANK, F. C., and KASPER, J. S., 1958, *Acta crystallogr.*, **11**, 184.
FROST, H. J., 1982, *Acta metall.,* **30**, 889.
FUKUNAGA, T., WATANABE, N., and SUZUKI, K., 1984, *J. non-crystalline Solids,* **61–62**, 343.
GASKELL, P. H., 1983, *Glassy Metals* II, edited by H. Beck and H.-J. Guntherodt (Berlin: Springer), p. 5.
HANNEMANN, A., SCHÖN, J. C., and JOHNSEN, M., 2002, *Computer Physics Comm.*, **144**, 284.
INOUE, A., 2000, *Acta mater.,* **48**, 279.
JIN, O., SCHWARZ, R. B., ALAMGIR F. M., and JAIN, H., 2000, *Materials Research Society Symposium Proceedings* Vol. 580, edited by A. Gonis, P. E. A. Turchi and A. J. Ardell (Pittsburgh, Pennsylvania: Materials Research Society), p. 277.
KINGERY, W. D., BOWEN, H. K., and UHLMANN, D. R., 1975, *Introduction to Ceramics* (New York: Wiley).
LAMPARTER, P., STEEB, S., and GRALLATH, E., 1983, *Z. Naturf.* (a), **38**, 1210.
LEE, A., ETHERINGTON, G., and WAGNER, C. N. J., 1984, *J. non-crystalline Solids,* **61–62**, 349.
LINES, M. E., 1979, *Phys Rev.* B, **20**, 3729.
MARET, M., SOPER, A., ETHERINGTON G., and WAGNER, C. N. J., 1984, *J. non-crystalline Solids,* **61–62**, 313.
MATSUBARA, E., WASEDA, Y., INOUE, A., OHTERA, H., and MASUMOTO, T., 1989, *Z. Naturfor.* (a), **44**, 814.
MIRACLE, D. B., 2003, *J. non-crystalline Solids*, **317**, 40.
MIRACLE, D. B., and SENKOV, O. N., 2001, *Proceedings of the Fourth Pacific Rim International Conference on Advanced Materials and Processing* Vol. II, edited by S. Hanada and N. Masahashi (Tokyo: Japan Institute of Metals), p. 2893; 2003, *J. non-crystalline Solids*, **319**, 174.
NELSON, D. R., and SPAEPEN, F., 1989, *Solid St. Phys.,* **42**, 1.
PAULING, L., 1960, *The Nature of the Chemical Bond,* third edition (Ithaca, New York: Cornell University Press).
POLK, D. E., 1972, *Acta metall.,* **20**, 485.
RAMACHANDRARAO, P., 1980, *Z. Metallk.,* **71**, 172.
SCOTT, G. D., and KILGOUR, D. M., 1969, *J. appl. Phys.* D, **2**, 863.
SENKOV, O. N., and MIRACLE, D. B., 2001, *Mater. Res. Bull.,* **36**, 2183; 2003, *J. non-crystalline Solids,* **317**, 34.

VARSHNEYA, A. K., 1993, *Fundamentals of Inorganic Glasses* (San Diego, California: Academic Press).

VISSCHER, W. M., and BOLSTERLI, M., 1972, *Nature,* **239**, 504.

WELLS, A. F., 1984, *Structural Inorganic Chemistry*, Fifth edition (Oxford, UK: Clarendon Press).

YAVARI, A. R., and INOUE, A., 1999, *Materials Research Society Symposium Proceedings* Vol. 554, edited by W. L. Johnson, A. Inoue and C. T. Liu (Pittsburgh, Pennsylvania: Materials Research Society), pp. 21–30.

ZHENG, J., CARLSON, W. B., and REED, J. S., 1995, *J. Eur. Ceram Soc.,* **15**, 479.

Philosophical Magazine

ISSN: 1478-6435 (Print) 1478-6443 (Online) Journal homepage: www.tandfonline.com/journals/tphm20

Quantized fracture mechanics

Nicola M. Pugno & Rodney S. Ruoff

To cite this article: Nicola M. Pugno & Rodney S. Ruoff (2004) Quantized fracture mechanics, Philosophical Magazine, 84:27, 2829-2845, DOI: 10.1080/14786430412331280382

To link to this article: https://doi.org/10.1080/14786430412331280382

Published online: 21 Feb 2007.

PHILOSOPHICAL MAGAZINE, 21 SEPTEMBER 2004
VOL. 84, NO. 27, 2829–2845

Taylor & Francis
Taylor & Francis Group

Quantized fracture mechanics

NICOLA M. PUGNO†

Department of Structural Engineering, Politecnico di Torino, Corso Duca degli Abruzzi 24, 10129, Italy

and RODNEY S. RUOFF‡

Department of Mechanical Engineering, Northwestern University, Evanston, IL 60208-3111, USA

[*Received 28 May 2004 and accepted 30 May 2004*]

ABSTRACT

A new energy-based theory, quantized fracture mechanics (QFM), is presented that modifies continuum-based fracture mechanics; stress- and strain-based QFM analogs are also proposed. The differentials in Griffith's criterion are substituted with finite differences; the implications are remarkable. Fracture of tiny systems with a given geometry and type of loading occurs at 'quantized' stresses that are well predicted by QFM: strengths predicted by QFM are compared with experimental results on carbon nanotubes, β-SiC nanorods, α-Si_3N_4 whiskers, and polysilicon thin films; and also with molecular mechanics/dynamics simulation of fracture of carbon nanotubes and graphene with cracks and holes, and statistical mechanics-based simulations on fracture of two-dimensional spring networks. QFM is self-consistent, agreeing to first-order with linear elastic fracture mechanics (LEFM), and to second-order with non-linear fracture mechanics (NLFM). For vanishing crack length QFM predicts a finite ideal strength in agreement with Orowan's prediction. In contrast to LEFM, QFM has no restrictions on treating defect size and shape. The different fracture Modes (opening I, sliding II and tearing III), and the stability of the fracture propagations, are treated in a simple way.

§ 1. INTRODUCTION

The phenomenon of fracture is of great interest. Two classic treatments are Griffith's criterion (1920), an energy-based method, and a method based on the stress-intensity factor (Westergaard 1939); these present a well-known paradox. For a linear elastic structural element containing a crack of infinitesimal length, both these methods of continuum-based linear elastic fracture mechanics (LEFM), shown to be equivalent (Irwin 1957), incorrectly predict an infinite load at failure. Conversely from elasticity, a singularity in the stress field at the crack tip (Westergaard 1939) is derived also for infinitesimal crack length; combined with the classical assumption that failure occurs when the maximum stress equals or exceeds the material strength, failure must occur at the physically unreasonable zero load. We choose to modify

† Author for correspondence. Email: n-pugno@northwestern.edu
‡ Author for correspondence. Email: r-ruoff@northwestern.edu

Philosophical Magazine ISSN 1478–6435 print/ISSN 1478–6443 online
http://www.tandf.co.uk/journals
DOI: 10.1080/14786430412331280382

fracture mechanics, by accounting for the discontinuous nature of matter at the atomic scale. By substituting the differentials in Griffith's criterion with finite differences, the paradoxes mentioned above are overcome, and a much more flexible theory, without *ad hoc* assumptions, results. We call this analytic theory quantized fracture mechanics (QFM) and show that QFM includes LEFM and NLFM as limiting cases.

QFM is particularly relevant to the fracture of tiny structures, such as of nanotubes, nanowires, and nanoplates that play, and will play, a central role in nanotechnology applications.

§ 2. Derivation of QFM

We assume a quantization of Griffith's criterion to account for discrete crack propagation, and thus in the continuum hypothesis, differentials are substituted with finite differences, i.e. $\mathrm{d}\rightarrow\Delta$. According to the principle of conservation of energy, Griffith's energy criterion implies a crack propagation when the variation of the total potential energy $\mathrm{d}W$, corresponding to a virtual increment of the crack surface $\mathrm{d}A$, becomes equal to the energy spent to create the new free crack surface, i.e., $\mathrm{d}W+G_{IC}\,\mathrm{d}A=0$, where $G_{IC}=2\gamma_{IC}$ is the fracture energy (per unit area created) of the material. The factor of 2 accounts for the creation of two surfaces during crack formation. The energy release rate is defined as $G_I=-\mathrm{d}W/\mathrm{d}A$ (where the derivation is evaluated at constant displacement), and Griffith's criterion is simply $G_I=G_{IC}$. If the fracture equilibrium state is stable the crack cannot propagate by itself (unless there were a change of loading, that is, the applied force or prescribed displacement). If the fracture equilibrium state is unstable, the crack will propagate by itself without any change of applied load or boundary displacement. The stability of the fracture equilibrium can be evaluated by the sign of the second derivative of the energy at the incipient crack propagation: if $(\mathrm{d}^2W/\mathrm{d}A^2)$ is positive, the fracture equilibrium is stable, if negative, unstable. It is well known that Griffith's criterion (1920) is equivalent to the stress-intensity factor-based criterion (Westergaard 1939) for brittle crack propagation, if the stress-intensity K_I and its critical value K_{IC} (the fracture toughness of the material) are assumed to be equal (Irwin 1957). According to LEFM (for details, see Bazant and Cedolin 1991, Hellan 1985, Carpinteri 1997), $G_I=K_I^2/E'$, with $E'=E$ (for plane stress) or $E'=E/(1-\nu^2)$ (for plane strain), where E is Young's modulus and ν is Poisson's ratio of the material. Because $G_{IC}=K_{IC}^2/E'$, the criterion $G_I=G_{IC}$ is equivalent to $K_I=K_{IC}$. Generalizing for opening (I), sliding (II), and tearing (III) crack modes, from LEFM $G=(K_I^2/E')+(K_{II}^2/E')+((1+\nu)/E)K_{III}^2$. LEFM is thus summarized as:

$$G\equiv-\mathrm{d}W/\mathrm{d}A=G_C;\ (\mathrm{d}G/\mathrm{d}A)_C<0 \text{ stable, if } >0 \text{ unstable, (LEFM)} \tag{1a}$$

$$K_{I,II,III}=K_{I,II,IIIC};\ (\mathrm{d}K_{I,II,III}^2/\mathrm{d}A)_C<0 \text{ stable, if } >0 \text{ unstable (LEFM)} \tag{1b}$$

On the other hand, in QFM ($\mathrm{d}\rightarrow\Delta$) equations (1) become:

$$G^*\equiv-\Delta W/\Delta A=G_C;\quad (\Delta G^*/\Delta A)_C<0 \text{ stable, if } >0 \text{ unstable (QFM)} \tag{2a}$$

$$K_{I,II,III}^*\equiv\sqrt{\left\langle K_{I,II,III}^2\right\rangle_A^{A+\Delta A}}=K_{I,II,IIIC};$$

$$\left(\Delta K_{I,II,III}^{*2}/\Delta A\right)_C<0 \text{ stable, if } >0 \text{ unstable (QFM)} \tag{2b}$$

where $\langle\cdot\rangle_A^{A+\Delta A} \equiv (1/\Delta A)\int_A^{A+\Delta A} \cdot \mathrm{d}A$. QFM assumes 'dissipation energy' in quanta $G_C \Delta A$ where ΔA is a *virtual* quantity that satisfies the condition that $\Delta A > 0$. Equations (1b) and (2b) are valid only for pure modes of crack propagation. For mixed modes, equations (1a) and (2a) can in principle be applied; the crack should propagate in the direction (that at nanoscale could be quantized) that maximizes the energy release rate G (LEFM; Wu 1978) or correspondingly G^* (QFM).

Values for the stress intensity factors $K_{I,II,III}$ are available (Murakami 1986) for the most interesting cases. QFM involves simply evaluating $K^*_{I,II,III}$ according to equation (2b), which also allows the stability of the process to be predicted. We thus propose QFM as a useful method for studying the strength of solids containing any shape or size defects. The hypothesis on which QFM is based is for discrete crack propagation in a linear elastic continuum medium.

2.1. *The stress analog of the energy-based QFM*

To our knowledge, only Seweryn (1998) has proposed a discrete energy release failure criterion. However, its mathematical formulation is completely different from QFM and of difficult application, since it involves the integration of the product of the complete (not only asymptotic) stress and displacement fields (which are *a priori* unknown) at the tip of the considered defect. Seweryn notes in his 'Concluding Remarks' that applying the non-local stress criterion is simpler for actual applications. The non-local stress criterion was introduced by Novozhilov (1969), who proposed a discrete fracture criterion based on stresses. He gave the condition of the brittle crack propagation in Mode I as:

$$\sigma^* \equiv \langle \sigma_y(x) \rangle_0^a = \sigma_C \tag{3a}$$

where $\sigma_y(x)$ is the complete (not only asymptotic) stress field around the defect tip ($x = 0$), σ_C is the ideal strength of the material, and a is the fracture quantum. This criterion can only be used if the complete expression of the stress-field, and not only its asymptotic term, is known; but the complete expression is rarely known. Note that this criterion could be extended for Modes II and III by replacing the normal stress with the corresponding shearing stress. Novozhilov assumed the fracture quantum to be the atomic spacing. We will show below, in the discussion of fracture strength of thin polysilicon films with self-similar holes of different sizes, the importance of relaxing this restriction by Novozhilov. For these reasons, the QFM approach of equations (2) is more powerful and at the same time, complementary to equation (3a). Novozhilov's approach, modified as stated (fracture quantum not restricted to be the atomic spacing), can be considered the stress version of QFM.

2.2. *The strain analog of the energy-based QFM*

An equivalent strain-based criterion is formulated simply by replacing the stress σ in equation (3a) with the strain ε, i.e.:

$$\varepsilon^* \equiv \langle \varepsilon_y(x) \rangle_0^a = \varepsilon_C \tag{3b}$$

The results of the discrete energy (QFM), stress- and strain-based criteria are in general expected to be close, but not identical. QFM is in general easier to apply because, as mentioned, LEFM provides the values of the stress-intensity factors for an enormous number of cases (Murakami 1986). As an example, we will compare

QFM, stress- and strain-based analogs and molecular dynamics simulations in predicting the strength of nanotubes with holes.

§ 3. Griffith's case

Consider Griffith's case of a linear elastic infinite plate in tension, of uniform thickness t, with a crack of length $2l$ orthogonal to the applied far field (crack opening Mode I). The material is described by the fracture toughness K_{IC} and by the fracture quantum at the considered size-scale $\Delta A \equiv at$. From LEFM, $K_I(l) = \sigma\sqrt{\pi l}$, where σ is the applied far field stress. According to LEFM the crack will propagate when $K_L = K_{IC}$; in contrast, for QFM the crack will propagate when

$$K_I^*(l) = \sqrt{\frac{1}{a}\int_l^{l+a} K_I^2(l)\,\mathrm{d}l} = K_{IC}.$$

The corresponding predictions for the failure strength of the plate are:

$$\sigma_{f-LEFM}(l) = \frac{K_{IC}}{\sqrt{\pi l}}, \tag{4a}$$

$$\sigma_{f-QFM}(l) = \frac{K_{IC}}{\sqrt{\pi(l + a/2)}} \tag{4b}$$

For $a/(2l) \to 0$ (i.e., large cracks) LEFM and QFM converge, whereas for $a/(2l) \to \infty$ (i.e., short cracks) they diverge. LEFM incorrectly predicts an infinite strength, whereas QFM predicts a reasonable finite strength: assuming that at the atomic scale the fracture quantum corresponds to the atomic size, the strength predicted by QFM is identical to Orowan's prediction (1948) if multiplied by a factor of $\sqrt{\pi/4}$. (Note that the prediction of QFM for vanishing crack length corresponds to the ideal strength of the material for the type of crack propagation analysed; see the Appendix). We note that equation (4b) has been previously used, but only as an empirical rule with a considered as a best fit parameter to achieve a good fit to experimental data, for predicting the behavior of short cracks for brittle fracture (Suo and Gong 1993) and fatigue (Haddad *et al.* 1980). This clearly shows that QFM also well describes the deviations from LEFM that are experimentally observed in brittle fracture and in fatigue growth of short cracks.

Note that the 'Quasi' or 'Equivalent' LEFM proposed by Irwin, which '*a priori*' considers an equivalent length of the crack (the real crack length plus the size of the 'plastic zone') is different from our approach (e.g., yields different predictions). In addition, in contrast to QFM, 'Irwin suggested (rather than provided a conclusive argument)' such an assumption (see Hellan 1985, p. 87).

For Griffith's case, brittle crack propagation is predicted to be unstable for both LEFM and QFM theories, i.e., $(\mathrm{d}K_I^2/\mathrm{d}l)_C = K_{IC}^2/l > 0$ and, $(\Delta K_I^{*2}/a)_C = K_{IC}^2/(l + a/2) > 0$.

Extending the result of equation (4b) from sharp to blunt-cracks (Creager and Paris 1967, Drory *et al.* 1995), we find an asymptotic correction (small tip radii; see Appendix) in the following form:

$$\sigma_f(l,\rho) = K_{IC}\sqrt{\frac{1 + \rho/2a}{\pi(l + a/2)}} = \sigma_C\sqrt{\frac{1 + \rho/2a}{1 + 2l/a}} \tag{5}$$

where ρ is the tip radius and $\sigma_C = \sigma_f$ ($l = 0$, $\rho = 0$). Note that if the continuum hypothesis is made (a/ρ, $a/l \to 0$), equation (5) yields practically the same result as the classical tensional approach (maximum stress equal to material strength), for which the stress concentration σ_C/σ_f is $1 + 2\sqrt{l/\rho} \approx 2\sqrt{l/\rho}$ (small radii) as given by elasticity. On the other hand, equation (5) reduces to the correct prediction of QFM for a sharp crack, equation (4b). Thus, equation (5) clarifies and quantifies in a very simple manner the link between concentration and intensification factors. The result is simple but surprising: it predicts a finite (in contrast with LEFM) strength that is size-dependent (in contrast with the continuum tensional approach coupled with elasticity) for geometrical self-similar defects in an infinite plate.

§ 4. Quantized strength levels

The fracture quantum, as suggested by equation (4b), is expected to be of the order of $2K_{IC}^2/(\pi\sigma_C^2)$, where σ_C and K_{IC} are the strength and the fracture toughness of the material at the considered size scale, respectively. For nanostructures (vanishing pre-existing defects), σ_C should be the ideal strength and the fracture quantum is expected to be close to the atomic size (distance between adjacent bonds that break during crack propagation). The length of the defects should be an integer multiple of the lattice spacing, assumed as a constant. We assume that this length is equal to the fracture quantum a, and use this assumption to make predictions for the nanoscale. Moreover, we assume defects are like blunt cracks (e.g., adjacent vacancies), so that for an n-atom defect $2l \approx na$. The final assumption is that there are negligible interactions between defect and boundary (short defect). With these hypotheses, we can apply equation (5), and the strength is expected to be quantized as:

$$\sigma_f(n) \approx \sigma_C \sqrt{1 + \frac{\rho}{2a}} (1+n)^{-1/2}, \quad n > 0 \tag{6}$$

This quantization should be experimentally detectable in nanostructures, for which a small number for n ($\approx 1-10$) should be realistic and when the number n of missing atoms is small compared with the number of atoms of the resisting cross section area adjacent to the crack (the ligament).

According to equation (6), for a linear chain of n removed atoms, $2\rho \approx a$ and the quantized strengths are, σ_C ($n = 0$, $\rho = 0$), $0.79\sigma_C$ ($n = 1$), $0.65\sigma_C$ ($n = 2$), $0.56\sigma_C$ ($n = 3$), and so on. Similar quantization is expected for different types of defects (e.g., with different values of ρ; see also section below on circular holes). This discussion shows that a forbidden band exists, such that nanostructure strengths between σ_C and $\sim 0.8\sigma_C$ should not be observed for vacancy defects. It should find use in assessing whether the ideal strength has been observed by experiment and for evaluating when n is small.

§ 5. QFM predicted strengths compared with experimental values

5.1. *β-SiC nanorods*

The theses of Sheehan (1998) and Wong (1998) report fracture bending strengths (Table 1, first row) for β-SiC nanorods oriented along the [111] direction; the maximum fracture strength, 53.4 ± 5.6 GPa was also published in (Wong *et al.* 1997), and if we assume this is the ideal strength σ_C, as suggested in the literature (Wong *et al.* 1997); note that Weixue and Tzuchiang (1999) report a calculated value of

Table 1. Clustering of experimental strength [GPa] of β-SiC nanorods, α-Si_3N_4 whiskers and MWCNTs.

β-SiC	53.4 ± 5.6	32.9 ± 3.7	$13.8 \pm 2.2, 11.6 \pm 2.9, 10.2 \pm 2.1$			
α-Si_3N_4	59	38	28	24	21	17
MWCNT	63	43	39,37,37,35,34	28,26,24,24	21,20,20,19,18,18	12,11

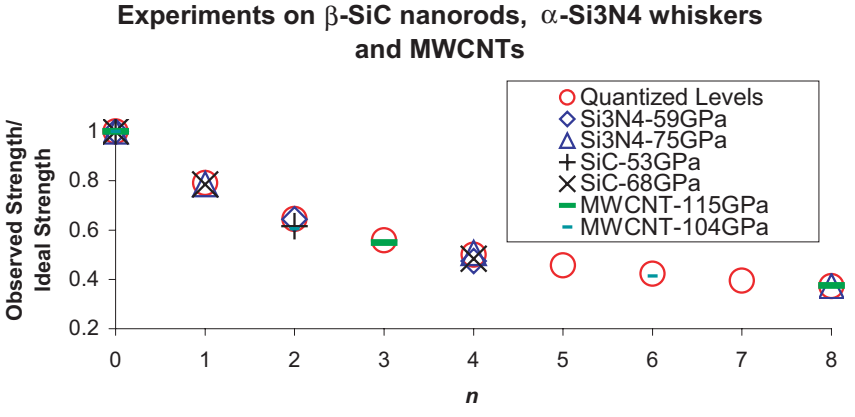

Figure 1. Quantized strength levels (observed fracture strength over ideal strength) from experiments on β-SiC nanorods, α-Si_3N_4 whiskers and MWCNTs, and QFM predicted values.

$\sigma_C = 50.8$ GPa for the [111] direction of β-SiC), QFM yields 30.8 GPa (equation (6), $n = 2$), close to the experimental value for the second highest strength measured 32.9 ± 3.7 GPa (note that equation (6) is valid also in bending, see Murakami (1986), where the failure stress is the maximum stress of the part of the nanorod in tension, and n is based on the quantized height of a small surface defect). The next value, 13.8 ± 2.2 GPa, can be interpreted by assigning $n = 4$. On the other hand, assuming 53.4 ± 5.6 GPa as $n = 1$, then 32.9 ± 3.7 GPa is best fit by $n = 4$, and the ideal strength ($n = 0$) would be $\sigma \approx 68 \pm 7.2$ GPa (we have simply multiplied the quoted error of ± 5.6 GPa by the same scaling factor of 68/53). The results are summarized in figure 1 for the two different hypotheses (β-SiC: 53 GPa $= \sigma_C$ and 68 GPa $= \sigma_C$). Fracture resulted from bending in these experiments (Wong *et al.* 1997). The probability of observing the ideal strength in bending might be greater than in pure tensile loading experiments. For bending, the volume near the clamp (where the stresses are highest) is only a small fraction of the total specimen volume.

5.2. *α-Si_3N_4 whiskers*

Experimental fracture strengths of $\alpha - Si_3N_4$ whiskers varying in diameter from 0.34 to 0.55 μm are reported by Iwanaga and Kawai (1998; Table 1, second row). Lengths were not provided in that paper (Iwanaga and Kawai 1998), but elsewhere the authors (Iwanaga and Kawai 2004, private communication) report that the typical lengths of the whiskers measured were about 1–2 mm; these $\alpha - Si_3N_4$ whiskers thus contained $\sim 10^{13}$ atoms. The observed maximum value was 59 GPa. The direction of growth for the tested whiskers was stated to be $[10\bar{1}1]$; 59 GPa can be

compared with recently calculated ideal strength values along similar (but not identical) crystal directions, which lie in the range of 51–60 GPa (Ogata *et al.* 2004); a recently calculated value for the ideal strength for loading along the $[10\bar{1}1]$ direction using identical methods to that of the previous reference, is 54 GPa (Ogata, private communication).

Assuming the highest experimental value of 59 GPa as the ideal strength; 38 GPa is well fit for $n=2$ and 28 GPa would correspond to $n=4$ (see table 1). If 59 GPa corresponds to $n=1$, the ideal strength ($n=0$) would be close to 75 GPa; 38 GPa would correspond to $n=4$, and 28 GPa to $n=8$. The results are summarized in figure 1 for the two different hypotheses (α-Si_3N_4: 59 GPa $=\sigma_C$ and 75 GPa $=\sigma_C$).

5.3. *Carbon nanotubes*

Tensile-loading experiments on the outer shell of multi-walled carbon nanotubes (MWCNTs) (Yu *et al.* 2000) show distinct clusters about a series of decreasing values of strength, with the maximum 63 GPa, and the other values 'quantized' at 43, 36–37, 25–26, 19–20 and 11–12 GPa (table 1, third row). As mentioned above, recent density functional theory (DFT) calculated values of ideal strength (Weixue and Tzuchiang 1999, Ogata *et al.* 2004) are close to the highest experimental strengths reported for β-SiC nanorods and α-Si_3N_4 whiskers. We distinguish the current dataset for experimental fracture strengths (Yu *et al.* 2000) of carbon nanotubes (CNTs) because 63 GPa is not in agreement with the ideal tensile strength of small diameter CNTs recently obtained with density functional theory. The tensile strength of an (8,8), thus armchair, CNT was calculated to be 114.6 GPa; calculated tensile strengths of 107.5, 109.0 and 107.4 GPa, respectively, were reported (Ogata and Shibutani, 2003) for three zig-zag CNTs: (8,0), (9,0) and (10,0). Another group has calculated the tensile strength of the (8,8) CNT and the (14,0) zig-zag CNT (23); these two CNTs have close to the same diameter, namely 1.09 nm (8,8) and 1.10 nm (14,0). The authors presented curves of the loading force versus tensile strain (Umeno *et al.* 2003); we used the maximum force quoted, namely 122 nN (8,8) and 128 nN (14,0); with the assumption of a 0.34-nm shell width, these correspond to tensile strengths of 104 GPa (8,8) and 110 GPa (14,0). We have simply used the two values of 115 and 104 GPa (the tensile strength values obtained by Ogata and Shibutani (2003) and Umeno *et al.* (2003) for the (8,8) CNT) as example tensile strengths of a defect-free CNT, in the analysis below. We note that the outer shell chiral angle was unknown for the 19 MWCNTs whose fracture strength was measured (Yu *et al.* 2000). With 115 (104) GPa for σ_C the measured value of 63 GPa is fit with $n=3$ ($n=2$) and the next highest experimental value of 43 GPa is fit with $n=8$ ($n=6$), as summarized in figure 1 (MWCNT 115 GPa $=\sigma_C$ and 104 GPa $=\sigma_C$). Note that these 19 outer shells, of different dimensions, were composed of between 4 and 54 million atoms. From comparison with the recent DFT and tight-binding calculations, it appears that none of the 19 MWCNTs had defect-free outer shells.

We therefore turn to comparison of QFM predicted strengths with a molecular mechanics (MM) simulation of large-diameter CNT fracture strengths where known defects were introduced, as well as comparison with molecular dynamics (MD) models of graphene sheet fracture strength as a function of an introduced crack in the side of the sheet. We also compare with a statistical mechanics treatment of fracture of one other type of two-dimensional sheet, a two-dimensional triangular lattice of springs. In these three cases one knows the defect type for treating with QFM.

§6. QFM predicted strengths compared with molecular mechanics of CNT, molecular dynamics of graphene, and statistical mechanics of 2-d spring lattices

6.1. *MM of CNT*

It has been argued that the experimental fracture strengths of the outer shell of MWCNTs (Yu *et al.* 2000) discussed above are well understood through MM analysis (Belytschko *et al.* 2002), which we here compare with QFM.

The simulations (Belytschko *et al.* 2002; MM, 0 K) on a large diameter zig-zag (80,0) CNT, which has a diameter of 6.3 nm, treated the reduction in strength due to missing pairs of carbon atoms. In the simulations, an n-atom defect was created by removing n adjacent atoms along the circumference of the nanotube; two-, four-, six- and eight-atom defects were treated. The comparison between these MM simulations and equation (6) is summarized in table 2: the MM-calculated strengths clearly follow the $(1+n)^{-1/2}$ dependence predicted by QFM. (The same quantized trend was reflected in the critical strains.) This suggests identifying the fracture quantum with the distance between two adjacent bonds, i.e., $a \approx \sqrt{3} r_0$, with $r_0 \approx 1.42$ Å, for the more likely (Appendix) 'zig-zag' fracture. The comparison using QFM, equation (6), is appropriate because of the large diameter of the experimentally investigated (Yu *et al.* 2000) and numerically modelled (Belytschko *et al.* 2002) nanotubes; the ratio between crack and circumferential lengths can be considered as negligible. We have noted the close fit to a $(1+n)^{-1/2}$ dependence; this is the fit, of course, for two-, four-, six- and eight-atom defects, with $\sigma_C \sqrt{1+\rho/2a} = 111$ GPa. For the value of the ideal strength calculated in (Belytschko *et al.* 2002), $\sigma_C = 93.5$ GPa, equation (6) gives the reasonable value of $\rho \approx 0.8a \approx 2.0$ Å.

Treating these adjacent vacancies as sharp short cracks, we can also compare our predictions with the Griffith-Inglis short crack theory, described by Weertman (1986, 1996). Details are given in the *Appendix*. The comparison is reported in table 2, showing an interesting agreement.

6.2. *MD of grapheme*

We next consider MD simulation of a cracked graphene sheet of width 9.63 nm and with four adjacent atoms missing, which resulted in a calculated failure of 52 GPa (Belytschko and Xiao 2003). By using the QFM strength values from the analysis on CNTs presented above (a relevant comparison with a graphene sheet because of the large diameter CNTs experimentally measured (Yu *et al.* 2000) and also treated by MM (Belytschko *et al.* 2002), from equation (6) we estimate $n \approx \left(\frac{111}{52}\right)^2 - 1 \approx 4$ (evaluated as 'the nearest integer') identical to the number of atoms removed in the simulation. Conversely, $\sigma_f(n=4) \approx 111/\sqrt{5} \approx 50$ GPa,

Table 2. Comparison between molecular mechanics (MM) simulations, theoretical QFM predictions (equation (6)) and Griffith–Inglis short crack theory (GI), for the strength (GPa) of nanotubes with blunt-cracks (adjacent vacancies of n atoms).

n-atom defect	2	4	6	8
MM	64.1	50.3	42.1	36.9
QFM	64.1	49.6	42.0	37.0
GI	67.9	51.7	43.3	37.9

close to 52 GPa. This example again shows that the fracture quantum is expected to be close to the 'straight line' distance between two atoms, $a = \sqrt{3}r_0$.

6.3. *Two-dimensional spring lattices*

The influence of one-, two- and three-adjacent vacancies in a two-dimensional triangular Lennard–Jones crystal was investigated by using a statistical-mechanics formulation (Selinger *et al.* 1991); the results for the strength at 0 K were 0.78, 0.69 and 0.62 of the defect-free strength, respectively. The authors noted that they expected these values to become somewhat larger with increasing temperature. By equation (6) a good fit is again given by the plausible value of $\rho \approx 0.8\,a$: 0.83, 0.69 and 0.59. In another treatment (Beale and Srolovitz 1987), that considered a two-dimensional triangular lattice with harmonic springs, the strength due to one vacancy in a two-dimensional lattice was estimated as ~0.8 the ideal strength. A reduction factor of 0.77 is again found in Hashimoto (1999) in which tight binding molecular dynamics was used to model the uniaxial tensile strength of diamond with one vacancy. Equation (6) thus represents the asymptotic behaviour in which as $n \to 0$ the ideal strength is approached, if vacancies are assumed as the defect. The detailed statistical mechanics treatment (Selinger *et al.* 1991) of the influence of defects on strength thus agrees with QFM. Note that by simply assuming $2\rho \approx a$, as in the section on quantized strength levels, the predicted strength scaling factors are, respectively, 0.79, 0.65 and 0.56 (and so on, see figure 2).

We now turn to discussing a classic problem in mechanics, that of a hole in a plate. We show that QFM can well treat recent experimental data on small circular holes in polysilicon thin films.

§ 7. Circular holes

As an example of comparison between QFM and its stress- and strain-based analogs, we derive the strength σ_f of an infinite plate with a circular hole of radius ρ, a classical problem in mechanics.

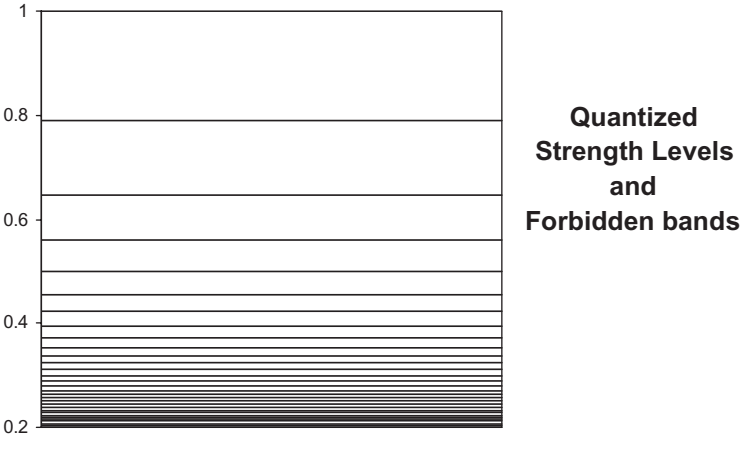

Figure 2. Example of quantized strength levels (fracture strength over ideal strength) and forbidden bands (n-atom defects, $2\rho \approx a$, equation (6)). Similar quantization is expected for different defect geometries.

QFM can be easily applied considering the expression of the stress-intensity factor at the tip of a crack emanating from a hole in a direction perpendicular to the far field stress (Tada *et al*. 1985), and then integrating according to equation (2b). On the other hand, starting from the expression of the stress-field around the hole (Kirsch 1898; see Carpinteri 1997), we find the predictions according to the strain-based QFM analog of equation (3b) (see Appendix) as:

$$\sigma_f = 2\sigma_C \Bigg/ \Bigg\{ 1 - \nu + \left(\rho^* - \rho^{*2}/(\rho^*+1)\right)(1+\nu) + \left(\left(1 - \rho^{*4}/(\rho^*+1)^3\right)(1+\nu) + 4\nu\rho^{*2}/(\rho^*+1) + \rho^* - 3\nu\rho^* \right) \cos 2\vartheta \Bigg\},$$
$$\rho^* = \frac{\rho}{a} \tag{7}$$

where ϑ is the angle describing the direction of the crack propagation with respect to the direction perpendicular to the far field. Equation (7) can be used to predict the strength of graphene sheet or 'large' nanotubes with pinhole defects. Usually $\vartheta = 0$, but for a chiral nanotube ϑ represents the chiral angle, the direction of the broken bonds (see Appendix for details) and ν is Poisson's ratio. The predictions according to the stress-based QFM analog can be obtained applying equation (3a). The result is formally equal to equation (7) in which $\nu = 0$ (here we assume plane stress and, by definition, $\varepsilon_C \equiv \sigma_C/E$, where E is Young's modulus; for plane strain $E \to E/(1-\nu^2)$, $\nu \to 1/(1-\nu)$). Below we compare QFM results with experimental results on micron-scale holes in polysilicon thin films, and also with recent MM and MD simulations of nanotubes with nanometer-scale holes.

The quantization yields the interesting result previously discussed: the strength is a function of the radius of the hole ρ and becomes equal to the classical case of $\sigma_C/3$ only by assuming the continuum hypothesis ($a/\rho \to 0$, i.e., $\rho^* \to \infty$, $\vartheta = \nu = 0$). For $\rho^* \to 0$ the hole is predicted to have no effect on the strength. Note that at small scale, we expect a minimum value for $\rho^* \sim 1/2$, which corresponds to one vacancy and to a reduction of the strength by a factor of $\sim$0.7 (this prediction is slightly different than that of 0.8 mentioned above, since they are based on different criteria).

7.1. *Experiments on polysilicon thin films with holes*

Chasiotis and Knauss (2003) present results on micro-testing experiments for different notch radii in polysilicon thin films. For circular holes of radii 1, 2, 3 and 8 μm, strength reductions, respectively, of 0.69, 0.63, 0.66, and 0.45 were measured. Noting that for polysilicon (at the considered size-scale) $\sigma_C \approx 0.85$ GPa, $K_{IC} \approx 1.5$ MPa$\sqrt{\text{m}}$ (Chasiotis and Knauss 2003), we expect $a \approx 2K_{IC}^2/(\pi\sigma_C^2) \approx 2$ μm, clearly different from the value at nanoscale. For example, with equation (7) with $\vartheta = \nu = 0$, for circular holes of radii 1, 2, 3 and 8 μm, reductions, respectively, of 0.71, 0.59, 0.53 and 0.42, are obtained. The agreement is reasonably good (although the 0.66 reduction for the 3-μm hole is off the expected trend) and shows how the classical prediction of $\sigma_C/3$ is clearly violated.

Similar experimental results are discussed in a recent paper (Bagdahn *et al*. 2003). The fracture strengths of polysilicon thin films with and without holes of radius 2.5 μm for two different film widths (20 and 50 μm) were measured; deviations from the classical value, $\sigma_C/3$, were found (note that for these finite plates, $\sigma_C/3.23$ is expected from finite element analysis for the 20-μm width, and $\sigma_C/3.04$ for the

50-μm width) (Bagdahn *et al.* 2003). In particular, we focus attention on the average values (the distribution of strengths follows a classical Weibull distribution) reported (Bagdahn *et al.* 2003), and obtain a ratio for the experimental strength of the films with and without the hole of 0.54 (20-μm width) and 0.69 (50-μm width); from equation (7) ($a \approx 2\,\mu m$, $\vartheta = \nu = 0$) we obtain 0.56.

This comparison emphasizes that at larger size scales a larger fracture quantum is expected, so that a much smaller hole would have little effect on the strength (here, a vacancy practically does not reduce the strength!); the reason is that at larger scales the materials typically have other larger defects besides the much smaller hole and such pre-existing defects are more critical than the investigated hole.

7.2. *MD simulations of carbon nanotubes with pinhole defects*

A further example is the strength of defective nanotubes with holes. Holes might be more stable than crack-like defects at the nanoscale. Nanotubes with "pinhole" defects, involving removal of 6 (defect $m = 1$) or 24 (defect $m = 2$) carbon atoms have been recently investigated in a (10,10) nanotube by MD simulation (Hirai *et al.* 2003). We estimate the radius of curvature of each hole as $\rho_m \approx (2m - 1)r_0$. Since the ratio $2\rho_m/\pi D$, with D nanotube diameter, is small (0.09 and 0.18 respectively for pinhole defects $m = 1$ and $m = 2$ in a (10,10) nanotube), we treat the nanotube as an infinite graphene sheet.

We also investigate larger values of m, where the next larger hole is generated from the previous one by removing the "next perimeter" of carbon atoms ($m = 3$, 56 atoms removed; $m = 4$, 96 atoms removed; $m = 5$, 150 atoms removed; $m = 6$, 216 atoms removed). Quantum mechanical calculations using DFT, semi-empirical quantum mechanical methods, and MM calculations, have recently been performed (Mielke *et al.* 2004) on much larger nanotubes, such as the (50, 0) and (100, 0) zig-zag tubes, with $m = 1$–6 holes (thus the ratio $2\rho_m/\pi D$ remains relatively small also for the $m = 3$, 4, 5, and 6 cases for these larger nanotubes). Applying QFM and its stress and strain analogs and using the value of $a \approx \sqrt{3}r_0$ previously deduced yields the results reported in Table 3; there is close agreement with the MM calculations on nanotubes by Mielke *et al.* (2004). Even though there is reasonable agreement for the numerically computed strength reductions of 0.80 ($m = 1$) and 0.55 ($m = 2$) for the (10, 10) nanotube by (Hirai *et al.* 2003) in our opinion these numerical results, which include

Table 3. Predicted reductions in strength of nanotubes for the presence of pinholes defects (defect $m = 1$, 6 atoms removed, $m = 2$, 24 atoms; $m = 3$, 56 atoms; $m = 4$, 96 atoms; $m = 5$, 150 atoms; $m = 6$, 216 atoms). Comparison between QFM, stress- and strain-based QFM analogs and molecular mechanics (MM) calculations on (50,0) and (100,0) zig-zag nanotubes ($\sigma_C \approx 89\,GPa$).

		QFM stress-analog (strain-analog with $\nu = 0$)	QFM strain-analog ($\nu = -0.5$)	QFM strain-analog ($\nu = +0.5$)	MM calculations on nanotubes	
σ/σ_C	QFM				(50,0)	(100,0)
$m = 1$	0.68	0.69	0.63	0.76	0.64	0.65
$m = 2$	0.48	0.51	0.47	0.55	0.51	0.53
$m = 3$	0.42	0.45	0.42	0.48	0.44	0.47
$m = 4$	0.39	0.42	0.40	0.44	0.40	0.43
$m = 5$	0.37	0.40	0.39	0.42	0.37	0.41
$m = 6$	0.36	0.39	0.38	0.40	0.34	0.39

a calculated ideal strength of ~300 GPa, do not consider an important factor. The very large computed ideal strength (as compared to the DFT calculated values of ~110 GPa (Ogata and Shibutani 2003, Umeno *et al*. 2003) suggests that there was a problem in the cut-off of the Brenner potential used (as has been discussed by Belytschko *et al*. (2002)). Thus, we consider as more relevant the comparison with the MM calculations by Mielke *et al*. (2004).

Finally, we note that in the paper by Mielke *et al*. (2004), strength reductions due to one atomic vacancy by factors of 0.81 for (10, 0) and 0.74 for (5, 5) nanotubes are close to our QFM-based prediction of 0.79.

7.3. *Experiments on carbon nanotubes*

We note that if one assumes an ideal strength of 115 GPa (as computed by DFT simulation (Ogata and Shibutani 2003) for the (8,8) nanotube) for the 20 to 40 nm diameter MWCNTs experimentally investigated (Yu *et al*. 2000) the corresponding strength (equation (7), $\vartheta = \nu = 0$) for a pinhole $m = 2$ defect is 59 GPa (measured value of 63 GPa, Table 1) and for an $m = 8$ defect is 43 GPa (measured value of 43 GPa, Table 1). This could represent another plausible scenario compared to the assumed linear defects that were previously treated by MM (Belytschko *et al*. 2002) and discussed above in Section 6.1. Indeed, Mielke *et al*. (2004) have pointed out the likelihood of large holes in the outer shells of the MWCNTs for which 19 experimental strength values (Yu *et al*. 2000) were obtained, based on the oxidation treatment used to remove extraneous carbonaceous material from the samples.

§ 8. LEFM and NLFM as limit cases of QFM

We show here that LEFM and NLFM are limit cases of QFM. In NLFM the material property G_C is replaced by an *ad hoc* resistance R (known as the R-curve) that increases, tending to G_C, by increasing the crack length. NLFM can be summarized as (for details see Hellan 1985):

$$G \equiv -\mathrm{d}W/\mathrm{d}A = R;\ (\mathrm{d}G/\mathrm{d}A)_C - (\mathrm{d}R/\mathrm{d}A)_C < 0 \text{ stable, if } > 0 \text{ unstable (NLFM)} \tag{8}$$

(Dynamic crack propagation is characterized by an excess of energy $G-R$, which is converted into kinetic energy.) Combining the conditions for crack propagation in equation (2a) and equation (8), it follows that $R = G_C + \Delta W/\Delta A - \mathrm{d}W/\mathrm{d}A$. Applying the operator $\Delta/\Delta A$ to the previous equation, it is clear that the conditions for stability in equation (2a) and equation (8) are equivalent if $\Delta G/\Delta A \equiv \mathrm{d}G/\mathrm{d}A$ and $\Delta R/\Delta A \equiv \mathrm{d}R/\mathrm{d}A$. It corresponds to a second-order expansion of W, i.e., $\Delta W \approx (\mathrm{d}W/\mathrm{d}A)\Delta A + (1/2)(\mathrm{d}^2W/\mathrm{d}A^2)(\Delta A)^2$. Consequently, equation (2a) corresponds to equation (1) (first-order approximation of QFM; QFM $\rightarrow$ LEFM), and to equation (8) (second-order approximation of QFM; QFM $\rightarrow$ NLFM), so that $R \approx G_C + (1/2) \times (\mathrm{d}^2W/\mathrm{d}A^2)_C \Delta A$. For example, applying the previous equation to the Griffith's case we find $R = G_{IC}/(1 + a/2l)$, exactly of the expected form. The classical limit of applicability of the R-curve in the NLFM treatment is that the R-curve is found as a function of the structure's geometry and not as a material property (see Bazant and Cedolin 1991); until now, it has been considered an experimental parameter. In contrast, QFM clarifies and quantifies in a very simple way the meaning of the R-curve.

§ 9. Concluding remarks

A new energy-based theory of fracture mechanics involving a modification of the well known continuum-based model has been developed that properly accounts for the discrete nature of matter (or energy release). The proposed quantized fracture mechanics (QFM) of equations (2) is self-consistent, and yields in its first-order approximation linear elastic fracture mechanics (LEFM) and in its second-order approximation non-linear fracture mechanics (NLFM). The predictions of LEFM and QFM were shown to converge for large sharp cracks, while for short cracks they diverge and only QFM correctly gives Orowan's estimate. In contrast to LEFM, which is applicable only to large sharp cracks, QFM can treat any defect shape and size. The condition for brittle crack propagation as well the stability of the process, can be evaluated for different structures, crack geometries, and modes of propagation. The application of QFM is extremely simple, allowing the prediction of the strength for any crack geometry through available stress-intensity factors that have been catalogued (Murakami 1986, Tada *et al*. 1985; i.e., an enormous number of cases). Stress- and strain-based QFM analogs have been also proposed and some examples of applications presented. Experimental results and numerical simulations for nanoscale structures agree well with QFM and its stress- and strain-based analogs.

The concept of forbidden bands for quantized strength was introduced, and should serve as a measure of whether experimental values include those close to the ideal strength.

Acknowledgements

The authors would like to thank S. Mielke, S. Zhang, D. Troya, G. Schatz, T. Belytschko, J. Achenbach, J. Weertman, B. Crist, A. Carpinteri and P. Cornetti, for many insightful discussions and A. L. Ruoff for critically reading and commenting on the manuscript prior to submission. RSR appreciates support from the NSF grant no. 0200797 ''Mechanics of Nanoropes'' (Ken Chong and Oscar Dillon, program managers), from the Office of Naval Research grant no. N00014-02-1-0870 ''Mechanics of Nanostructures'' (Mark Spector and John Pazik, program managers) and from the NASA University Research, Engineering and Technology Institute on Bio Inspired Materials (BIMat) under award No. NCC-1-02037 (Jeff Jordan, program manager).

APPENDIX A

§ A1. *Ideal strength*

Note that the prediction of QFM, for vanishing crack length, corresponds to the ideal strength of the material for the crack propagation analysed. Changing the crack propagation analysed (e.g., edge crack in a finite plate versus the Griffith's case of an (interior) crack in an infinite plate) leads to slightly different values for the 'ideal strength'. For an edge crack in a finite plate the QFM strength is 1.12 times smaller than the predicted QFM strength for the interior crack in an infinite plate (Murakami 1986). This shows that the strength, in the limiting case of vanishing defect size, cannot be considered (by QFM) separately from the analysed structure. It is plausible (certainly from an engineering perspective!) to assign the 'engineering

strength of the defect-free structure' as the smallest value resulting from analysis of the possible crack propagations leading to fracture (e.g., for a finite plate the crack would be likely to start from an edge, thus at a strength level 1.12 times smaller than as predicted by equation (4b)).

From equation (4b) the fracture quantum is expected to be of the order of $a \approx 2K_{IC}^2/(\pi\sigma_C^2)$ (neglecting the corrections, e.g., the factor 1.12 for a finite plate), where σ_C is the strength of the material (without pre-existing defects) at the considered size scale (at atomic scale, where the pre-existing defects vanish σ_C represents the ideal strength of the material). Thus the fracture quantum typically becomes larger at larger size scale. Note that the fracture quantum at larger scale sizes could be several orders of magnitude larger than the atomic size (if definable), so that a 'finite crack extension' might be a more appropriate terminology than 'fracture quantization'. (Of course, one of the goals of nanotechnology is to create defect-free materials even at large length scale.)

§ A2. *Blunt cracks*

We apply equation (3a) to predict the strength of nanostructures containing defects like chains of removed atoms, more similar to blunt-cracks (involving an atom removal, i.e., adjacent vacancies) rather than to ideal sharp nano-cracks (broken bonds, which we, and others schooled in *ab initio* calculations (Mielke *et al*. 2004), find to be less likely). Defects such as holes are also investigated (section V below).

For a blunt notch the asymptotic stress field around the tip (Creager and Paris 1967) is

$$\sigma_{asy}(x) = \frac{K_I'}{\sqrt{2\pi x}}\left(1 + \frac{\rho}{2x}\right),$$

where the origin of the reference system is in the middle between the tip and the center of the circular blunt notch, so that $x > \rho/2$, where ρ is the root notch radius and K_I' is the corresponding stress-intensity factor (the 'prime' distinguishes the case of a sharp crack). Applying equation (3a) and comparing the result with its limiting case of a sharp crack ($\rho/a = 0, K_I' = K_{IC}$) gives the asymptotic correction $K_{IC}' \approx \sqrt{1 + (\rho/2a)}\, K_{IC}$ of the critical stress-intensity factor due to the presence of the blunting (for not too large values of ρ/a, since this analysis neglects the far field with respect to the asymptotic one). As a limit case, we can consider the correction derived in (Drory *et al*. 1995) starting from the form of $\sigma_{asy}(x)$ and noting that $x > \rho/2$, i.e., $K_{IC}' \approx K_{IC}/2$.

The derived correction for the critical value of the stress-intensity factor, can be applied also for the study of nano-defects of general shape. If the profile of a defect is described by a function $y(x)$, the radius of the blunt is $\rho = (1 + (y')^2)^{3/2}/y''$, where the primes represent the derivation with respect to x (orthogonal to the applied stress). For example, for an ellipse having half-axes of length l (orthogonal to σ) and t, the radius of the blunt is $\rho = t^2/l$. In addition, since $\sigma_y(x) \approx \sigma + \sigma_{asy}(x)$, assuming an infinite plate, $K_I' = \sigma\sqrt{\pi l}$, and evaluating the stress concentration at the tip of an elliptical hole, gives $\sigma_y(x = \rho/2, K_I' = \sigma\sqrt{\pi l}, \rho = t^2/l) = \sigma(1 + 2l/t)$, thus the correct value from Elasticity.

§ A3. *Zig-zag and armchair fracture*

Even if it is clear that the fracture toughness tends to decrease with decreasing specimen size, we note that to match MM simulations (Belytschko *et al.* 2002) with equation (5), a low value of fracture toughness of $K_{IC} \approx 2\,\mathrm{MPa}\sqrt{\mathrm{m}}$ for a 'zig-zag' crack has to be assumed. A simple estimation of the fracture toughness could be obtained considering the bond dissociation energy from the Brenner potential (124 kcal/mole of C–C bonds), yielding $\gamma \approx 4.46\,\mathrm{N/m}$. Defining a 'straight line' for the edge, this value has to be multiplied by the factor $2/\sqrt{3}$ for zig-zag cracks or by the factor 4/2 for armchair cracks, so that $\gamma^{ZZ} \approx 2/\sqrt{3}\gamma$ and $\gamma^{AC} \approx 4/3\gamma$, respectively. Simply considering these values to evaluate the stress-intensity factor in Mode I as γ_{IC} (or in general $\gamma_{I,II,IIIC}$, since we expect that the fracture toughness for the different crack propagation Modes I, II and III tend to coincide at nanoscale), yields respectively $K_{IC}^{ZZ} \approx 3.21\,\mathrm{MPa}\sqrt{\mathrm{m}}$ and $K_{IC}^{AC} \approx 3.45\,\mathrm{MPa}\sqrt{\mathrm{m}}$ ($E \approx 1\,\mathrm{TPa}$).

For a zig-zag crack $a^{zz} \equiv a$, whereas for an armchair crack $a^{AC} \approx \sqrt{3}/2a^{zz}$, since the ratio of the strength corresponding to zig-zag and armchair cracks

$$\frac{\sigma^{ZZ}}{\sigma^{AC}} \approx \frac{1}{\cos\vartheta}\sqrt{\frac{\gamma^{ZZ}a^{AC}}{\gamma^{AC}a^{ZZ}}}$$

is larger than 1 for each $\vartheta < \pi/6$, zig-zag cracks are more likely than armchair cracks, as numerically observed (Belytschko *et al.* 2002) in both zig-zag and armchair, as well as chiral, nanotubes. The case of $\vartheta < \pi/6$ corresponds theoretically to $\sigma^{ZZ}/\sigma^{AC} \approx 1$, even if practically a small perturbation should lead to a 'zig-zag' crack.

Thus for a 'chiral' nanotube, we expect a zig-zag fracture, and consequently higher values of strength than for the zig-zag tubes, due to the reduction of the component of the external force acting on the bonds. Roughly, the ratio between the stress acting on the breaking bonds and the applied external stress should be close to $\cos(\vartheta)$, where ϑ is the chiral angle (note that considering the tensor nature of the stress $\cos^2(\vartheta)$ would appear instead of $\cos(\vartheta)$. Equation (7) agrees with this tensor nature of the stress, i.e., $\sigma_f(\rho = \nu = 0) = \sigma_C/\cos^2(\vartheta)$, with σ_C the strength of the bonds). The expected larger strength of chiral vs. zig-zag nanotubes agrees with MM and MD simulations (Belytschko *et al.* 2002). For example, for a zig-zag nanotube ($\vartheta = 0$) a strength of 93.5 GPa was computed, whereas for an armchair nanotube ($\vartheta = \pi/6$) 112 GPa was obtained (and for a chiral (16, 8) nanotube an intermediate value of 106 GPa was computed). The ratio 93.5/112 is equal to 0.83, between $\cos^2\pi/6 = 0.75$ and $\cos\pi/6 \approx 0.87$. Note that the same trend was numerically observed in (Ogata and Shibutani 2003).

§ A4. *Griffith–Inglis short crack theory*

According to the Griffith–Inglis short crack theory (see Weertman 1996, 1986), the prediction for the failure stress of a structure containing sharp short cracks is

$$\sigma_f = \frac{2\sigma_C}{\pi}\cos^{-1}\left(\exp\left(\frac{-\pi G\delta_C}{4(1-\nu)\sigma_C l}\right)\right),$$

where G and ν are respectively the shear elastic modulus and Poisson's ratio (that formally has to be set equal to zero for Mode III crack propagation) and δ_C is the critical tip displacement (on which the method is based). From Belytschko *et al.* (2002) $\sigma_C = 93.5\,\mathrm{GPa}$ and $E \approx 0.8\,\mathrm{TPa}$; since for nanotubes $\nu \approx 0.2$, $G \approx 0.333\,\mathrm{TPa}$. Using δ_C as a best fit parameter, we have $\delta_C \approx a/4$ (a reasonable value); the

corresponding predictions for the strength of nanotubes with short cracks of length $2l \approx 2a, 4a, 6a, 8a$ are reported in table 2 and compared with QFM and MM simulations.

§ A5. *Circular holes*

The stress near a hole of radius ρ (center at $x, y = 0$) in an infinite plate subjected to a remote stress field σ is (Kirsch 1898; see Carpinteri 1997)

$$\sigma_r = \frac{\sigma}{2}\left(1 - \frac{\rho^2}{r^2}\right) - \frac{\sigma}{2}\left(1 + 3\frac{\rho^4}{r^4} - 4\frac{\rho^2}{r^2}\right)\cos 2\vartheta,$$

$$\sigma_\vartheta = \frac{\sigma}{2}\left(1 + \frac{\rho^2}{r^2}\right) + \frac{\sigma}{2}\left(1 + 3\frac{\rho^4}{r^4}\right)\cos 2\vartheta$$

(the shearing stress does not affect our predictions). Assuming isotropic linear elastic constitutive laws and applying equation (3b) by integration, we obtain the result of equation (7), that gives the ratio between the strength σ of the element with a hole, with dimensionless radius $\rho^* = \rho/a$, and the ideal strength of the element (i.e., the strength of the element without the hole). On the other hand, applying equation (3a) we obtain the result of equation (7) if $\nu \to 0$. Assuming $\nu = \vartheta = 0$, three limit cases are interesting: (i) for $\rho^* \to 0$, $\sigma/\sigma_C \to 1$; (ii) for $\rho^* \to \infty, \sigma/\sigma_C \to 1/3$ (case of elasticity and classical tensional criterion, that assumes the continuum hypothesis, i.e., $a \to 0$); for $\rho^* \to 1/2$ (one vacancy in an ideal two-dimensional lattice), $\sigma/\sigma_C \to 0.71$.

References

Bagdahn, J., Sharpe, W. N., and Jadaan, O., 2003, *J. Microelectromech. Syst.*, **12**, 302.

Bazant, Z. P., and Cedolin, L., 1991, *Stability of Structure*: *Elastic*, *Inelastic*, *Fracture and Damage Theories* (Oxford University Press).

Beale, P. D., and Srolovitz, D. J., 1986, *Phys. Rev.* B, **37**, 5500.

Belytschko, T., and Xiao, S., 2003, *Int. J. Multiscale Comput. Engng*, **1**, 115.

Belytschko, T., Xiao, S. P., and Ruoff, R., 2002, Effects of defects on strength of nanotubes: experimental-computational comparison, *Los Alamos National Laboratory*, *Preprint Archive*, *Physics*, 1–6.

Belytschko, T., Xiao, S. P., Schatz, G. C., and Ruoff, R. S., 2003, *Phys. Rev.* B, **65**, 235430.

Blumberg Selinger, R. L., Wang, Z.-G., and Gelbart, W.M., 1991, *J. Chem. Phys.*, **95**, 9128.

Carpinteri, A., 1997, *Structural Mechanics*: *A Unified Approach* (London: Chapman & Hall).

Chasiotis, I., and Knauss, W. G., 2003, *J. Mech. Phys. Solids*, **51**, 1551.

Creager, M., and Paris, P. C., 1967, *Int. J. Fract. Mech.*, **3**, 247.

Drory, M., Dauskardt, R. H., Kant, A., and Ritchie, R. O., 1995, *J. appl. Phys.*, **78**, 3083.

El Haddad, M., Dowling, N. F., Topper, T. H., and Smith, K. N., 1980, *Int. J. Fract.*, **6**, 15.

Griffith, A. A., 1920, *Phil. Trans. Roy. Soc.*, **A221**, 163.

Hashimoto, T., 1999, *Molecular Simulation*, **23**, 143.

Hellan, K., 1985, *Introduction to Fracture Mechanics* (New York: McGraw-Hill).

Hirai, Y. *et al.*, 2003, *Jpn. J. appl. Phys.*, **42**, 4120.

Irwin, G. R., 1957, *Trans. ASME, J. appl. Mech.*, **E24**, 361.

Iwanaga, H., and Kawai, C., 1998, *J. Am. Ceram. Soc.*, **81**, 773.

Kirsch, R., July 1898, Die Theorie der Elastizitat und Die Bedurfnisse der Festigkeitslehre, *Zeitschrift Verein Duetscher Ingenieure*.

Mielke, S. L., Troya, D., Zhang, S., Li, J.-L., Xiao, S., Car, R., Ruoff, R. S., Schatz, G. C., and Belytschko, T., 2004, *Chem. Phys. Lett.*, **390**, 413.

Murakami, H., 1986, *Stress Intensity Factors Handbook* (Oxford: Pergamon).

Novozhilov, V., 1969, *Prik. Mat. Mek.*, **33**, 212.
Ogata, S., and Shibutani, Y., 2003, *Phys. Rev.* B, **68**, 165409-1/4.
Ogata, S., Hirosaki, N., Kocer, C., and Shibutani, Y., 2004, *Acta mater.*, **52**, 233.
Orowan, E., 1948, *Rep. Progr. Phys.*, **12**, 185.
Seweryn, A., 1998, *Engng. Fract. Mech.*, **59**, 737.
Sheehan, P. E., 1998, Mechanical and tribological studies at the nanometric scale, Ph.D. Thesis, *Diss. Abstr. Int., B*, **59**, 246.
Suo, Z., Ho, S., and Gong, X., 1993, *J. Engng. Mat. Tech.*, **115**, 319.
Tada, H., Paris, P. C., and Irwin, G. R., 1985, *The Stress Analysis of Cracks–Handbook*, Second Edition (Paris: Productions Incorporated).
Umeno, Y., Kitamura, T., and Matsui, E., 2003, *J. Soc. Mat. Sci. Japan*, **52**, 219.
Weertman, J., 1986, *J. appl. Phys.*, **60**, 1877; 1996, *Dislocation Based Fracture Mechanics* (Singapore: World Scientific).
Weixue, L., and Tzuchiang, W., 1999, *Phys. Rev.* B, **59**, 3993.
Westergaard, H. M., 1939, *J. appl. Mech*, **6**, 49.
Wong, E. W., 1998, Nanorods and nanotubes: synthesis, manipulation and properties, Ph.D. Thesis, *Diss. Abstr. Int. B*, **59**, 2225.
Wong, E. W., Xiao, S. P., Sheehan, P. E., Lieber, and C. M., 1997, Nanobeam mechanics: elasticity, strength and toughness of nanorods and nanotubes, *Science*, **277**, 1971.
Wu, C. H., 1978, *J. Appl. Mech.*, **45**, 553.
Yu, M.-F., Lourie, O., Dyer, M. J., Moloni, K., Kelly, T. F., and Ruoff, R. S., 2000, *Science*, **287**, 637.

Philosophical Magazine

ISSN: 1478-6435 (Print) 1478-6443 (Online) Journal homepage: www.tandfonline.com/journals/tphm20

Fullerene-related structure of commercial glassy carbons

P. J. F. Harris

To cite this article: P. J. F. Harris (2004) Fullerene-related structure of commercial glassy carbons, Philosophical Magazine, 84:29, 3159-3167, DOI: 10.1080/14786430410001720363

To link to this article: https://doi.org/10.1080/14786430410001720363

Published online: 22 Aug 2006.

Philosophical Magazine, 11 October 2004
Vol. 84, No. 29, 3159–3167

Taylor & Francis
Taylor & Francis Group

Fullerene-related structure of commercial glassy carbons

P. J. F. Harris†

Centre for Advanced Microscopy, J. J. Thomson Physical Laboratory, University of Reading, Whiteknights, Reading RG6 6AF, UK

[*Received 17 December 2003 and accepted 30 March 2004*]

Abstract

Glassy carbon is a technologically important material widely used in products such as electrodes and high-temperature crucibles. However, the properties which make glassy carbon so valuable in these applications are poorly understood, since its detailed atomic structure is not known. A model for the structure of glassy carbon put forward many years ago has gained wide acceptance, but appears to suffer from serious shortcomings. In particular, it fails to account for the chemical inertness of the carbon, and for its high proportion of closed porosity. Here I show, using high-resolution transmission electron microscopy, that glassy carbons obtained from commercial suppliers contain a high proportion of fullerene-related structures. On the basis of these observations, models are put forward for the structures of 'low-temperature' and 'high-temperature' glassy carbons which incorporate non-six-membered rings.

§ 1. Introduction

Glassy carbon is an example of a non-graphitizing carbon, that is a carbon which cannot be transformed into crystalline graphite even at temperatures of 3000°C and above (Franklin 1951, Harris 1997). In addition to very high thermal stability, its distinguishing properties include its extreme resistance to chemical attack: it has been demonstrated that the rates of oxidation of glassy carbon in oxygen, carbon dioxide or water vapour are lower than those of any other carbon (Jenkins and Kawamura 1976). It is also highly resistant to attack by acids. Thus, while normal graphite is reduced to a powder by a mixture of concentrated sulphuric and nitric acids at room temperature, glassy carbon is unaffected by such treatment, even after several months. This property makes glassy carbon a useful material for crucibles. It is also used widely as an electrode material in electrochemistry, and its biocompatibility makes it a potential component of prosthetic devices.

The structure of glassy carbon has been the subject of research since it was first produced in the early 1960s. Some of the earliest structural models assumed that both sp^2- and sp^3-bonded atoms were present (e.g. Ergun and Tiensuu 1959). Graphitic domains were envisaged to be interspersed with tetrahedral domains, perhaps linked by short oxygen-containing bridges. These models were based primarily on an analysis of X-ray diffraction measurements and such measurements can be open to a number of interpretations. It should be noted that neutron diffraction data have shown a complete absence of tetrahedrally bonded domains in glassy

† E-mail: p.j.f.harris@reading.ac.uk.

Philosophical Magazine ISSN 1478–6435 print/ISSN 1478–6443 online
http://www.tandf.co.uk/journals
DOI: 10.1080/14786430410001720363

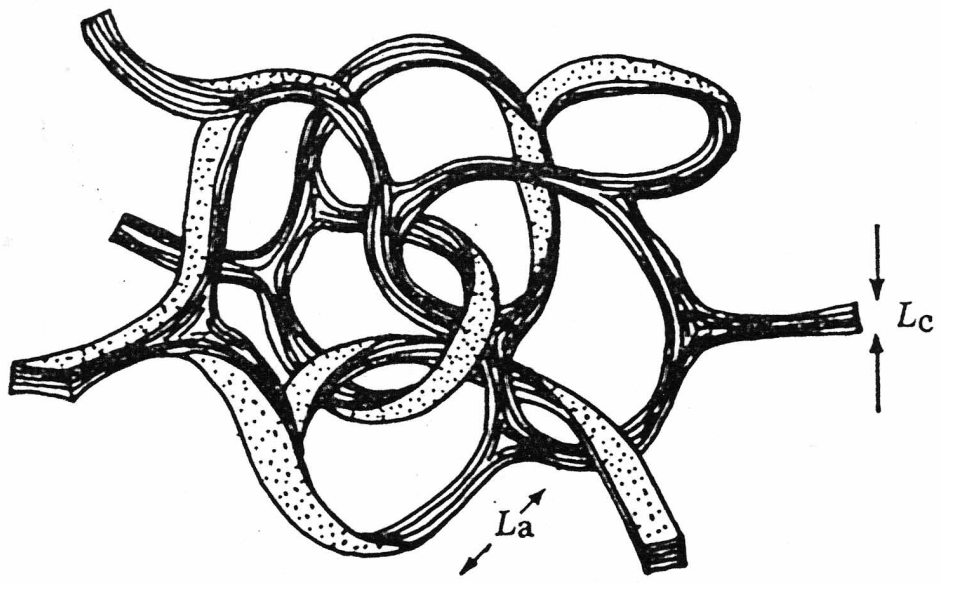

Figure 1. The Jenkins–Kawamura model of glassy carbon. L_a and L_c are the lengths of the graphitic domains perpendicular and parallel to the graphite c axis. Reproduced from Jenkins, G. M., and Kawamura, K., 1971, *Nature*, **231**, 175, with permission of Nature Publishing Group.

carbon heat treated at 2000°C (Mildner and Carpenter 1982). A different model for the structure of glassy carbon was put forward by Jenkins and colleagues (Jenkins and Kawamura 1971, 1976, Jenkins *et al.* 1972). This model, illustrated in figure 1, is based on the assumption that the molecular orientation of the polymeric precursor material is memorized to some extent after carbonization. Thus, the structure bears some resemblance to that of a polymer, in which the 'fibrils' are very narrow, curved and twisted ribbons of graphitic carbon. The Jenkins–Kawamura model has been quite widely accepted, but appears to be deficient in a number of aspects. For example, a structure such as that shown in figure 1, with many conjoined micropores, would be expected to be permeable to gases, whereas we know that glassy carbons are highly impermeable. The structure also has a high proportion of edge atoms, which are known to have a relatively high reactivity compared with 'in-plane' carbon atoms. This is inconsistent with the known low reactivity of glassy carbon, mentioned above. Recently, Russian workers have proposed a model for glassy carbon which incorporates carbyne-like chains (Pesin 2002, Pesin and Baitinger 2002). This model was based partly on a consideration of the electronic properties of glassy carbon but, as the authors themselves accept, there is no direct experimental support for their structure.

The discovery of the fullerenes (Kroto *et al.* 1985, Krätschmer *et al.* 1990) and subsequently of related structures such as carbon nanotubes (Iijima 1991) and nanoparticles (Harris 1999) has demonstrated that sp^2-bonded carbons containing non-six-membered rings can be highly stable. This led the present author and colleagues to explore the possibility that non-graphitizing carbons may have structures related to those of the fullerenes. Detailed studies of non-graphitizing carbons prepared by

pyrolysis of sucrose and polyvinylidene chloride (Harris and Tsang 1997) were carried out using high-resolution transmission electron microscopy (HRTEM). These provided evidence for completely closed fullerene-like carbon nanoparticles, together with other features strongly suggestive of a fullerene-related structure. As a result of these observations, a model was proposed for the structure of non-graphitizing carbons which consisted of discrete fragments of curved carbon sheets, in which pentagons and heptagons were dispersed randomly throughout networks of hexagons. Subsequent work using HRTEM and other techniques provided confirmation for these ideas (Burian and Dore 2000, Harris *et al.* 2000, Burian *et al.* 2002). The aim of the present study was to examine some typical glassy carbons using HRTEM, to see whether there is evidence to support the idea that fullerene-related structures are present.

§ 2. Experimental

Four samples of commercially available glassy carbon were studied: Sigradur K and Sigradur G, supplied by Hochtemperatur-Werkstoffe GmbH, Germany, and GL-100 and GL-200, supplied by Toyo Tanso, Japan. The Sigradur carbons were prepared from phenolic resins by controlled pyrolysis in an inert atmosphere at temperatures up to 1000°C (Sigradur K) and 2800°C (Sigradur G). The Toyo Tanso carbons were also prepared from thermosetting resins, heated to 1000°C (GL-100) and 2000°C (GL-200). A further heat treatment at 3000°C was carried out on the GL-200 carbon by Iwashita *et al.* (2002) – this carbon is given the code GL-200-3000.

Samples were prepared for transmission electron microscopy by grinding gently in an agate pestle and mortar under iso-propyl alcohol, depositing the suspension onto 'lacey' carbon support films and allowing the solvent to evaporate. The purpose of grinding was simply to disperse the carbon in the solvent, and did not result in disruption of the carbon nanostructure or contamination. Although much of the carbon deposited in this way was too thick for detailed imaging, sufficiently thin regions around the edges of particles could readily be found. The microscopes employed were a Philips CM20 and a JEOL 2010FX, both operated at 200 kV.

§ 3. Results and discussion

Typical high-resolution electron micrographs of Sigradur glassy carbon K and G are shown in figures 2 (*a*) and 2(*b*), respectively. In the case of the 'low-temperature' carbon, Sigradur K, the microstructure is disordered and isotropic, with little obvious formation of graphitic layer planes. Close examination of such images shows that the microstructure consists of tightly curled single carbon layers which enclose micropores of the order of 1 nm in diameter. In the 'high-temperature' carbon, Sigradur G, larger pores, around 5 nm in size, are present. These are bounded by faceted or curved graphitic walls typically containing two to four layer planes. An example of an apparently closed carbon nanostructure from the Sigradur G carbon is shown in figure 3 (*a*). This resembles a rather imperfect multilayered giant fullerene. There was evidence that much smaller fullerenes, similar in size to C_{60}, were also present; two such particles can be seen in figure 3 (*b*), attached to the end of a structure which resembles a carbon nanotube.

The low-temperature Toyo Tanso carbon, GL-100, was very similar in appearance to Sigradur K, and is not shown here. An image of the high-temperature Toyo Tanso carbon (GL-200-3000) is shown in figure 4. Here the graphitic structures

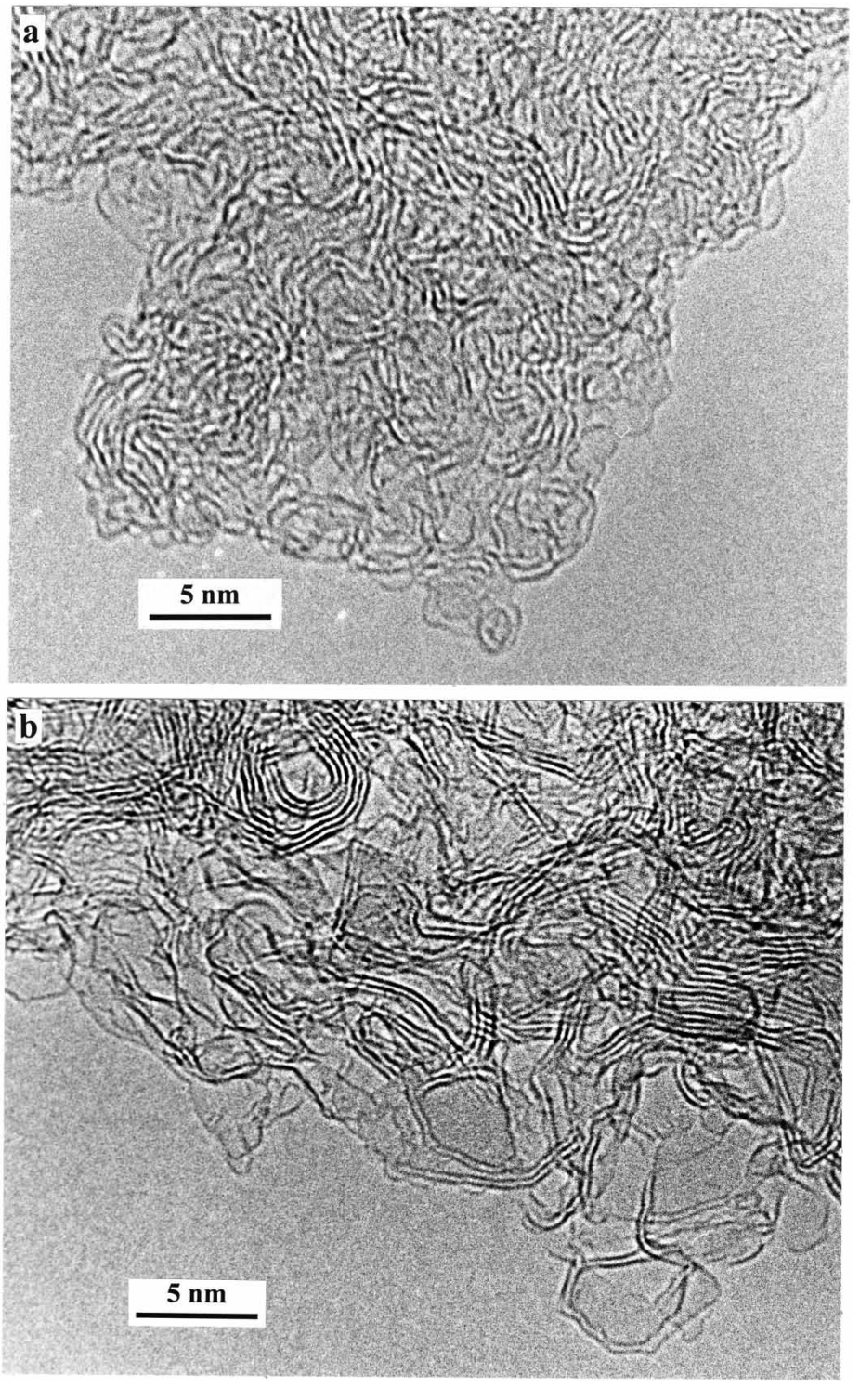

Figure 2. TEM images of (*a*) Sigradur K glassy carbon (prepared at 1000°C), (*b*) Sigradur G glassy carbon (prepared at 2800°C). The magnification is the same for both images.

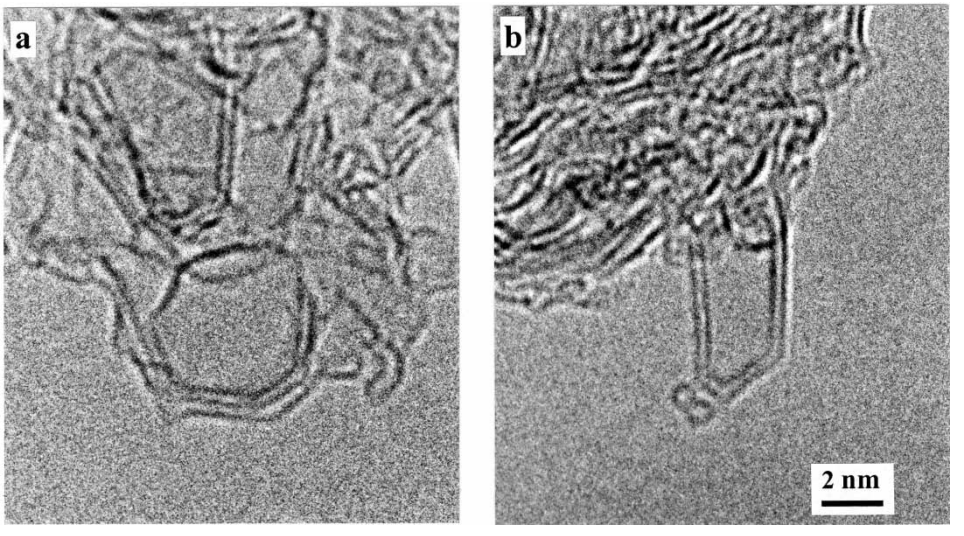

Figure 3. Nanostructures in Sigradur G carbon. (*a*) Imperfect nanoparticle, (*b*) nanotube-like structure with small fullerene particles at tip.

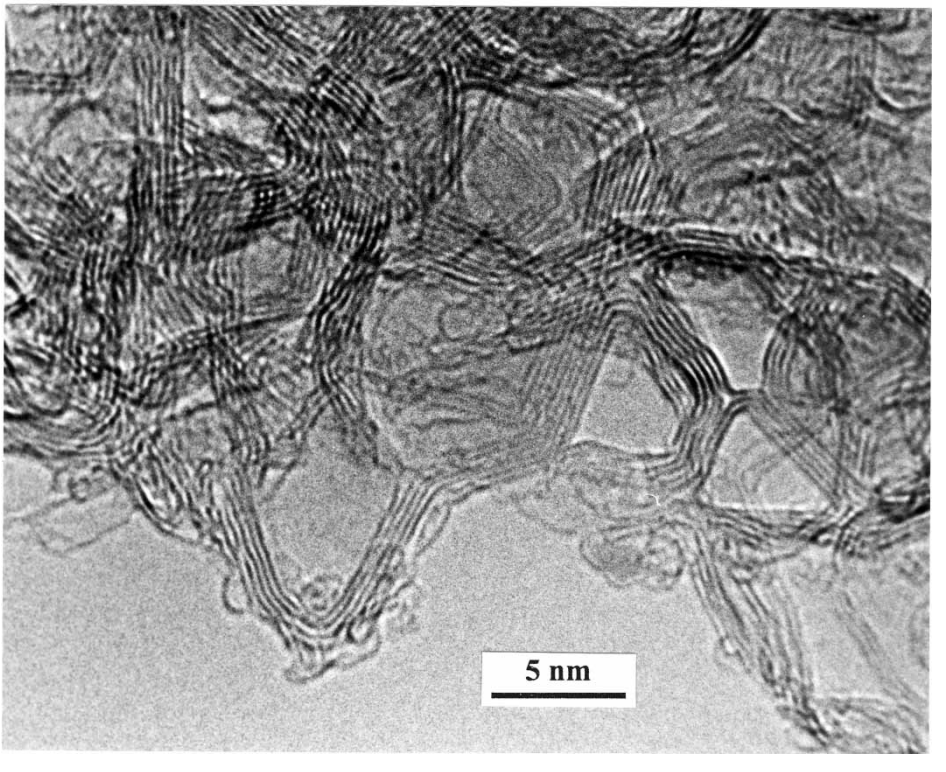

Figure 4. Image of Toyo Tanso glassy carbon GL-200 heated to 3000°C.

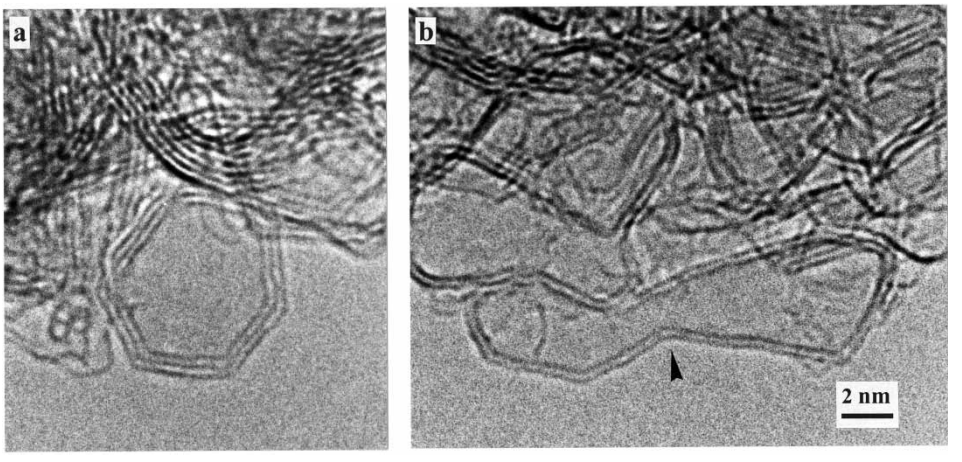

Figure 5. Nanostructures in Toyo Tanso glassy carbon. (*a*) Hexagonal nanoparticle, (*b*) closed structure with re-entrant feature indicative of heptagonal carbon ring. The magnification is the same for both images.

contain rather more layers than in the Sigradur G, reflecting the slightly higher temperature that the carbon has experienced. Completely closed particles could be found quite easily in this carbon; an example is shown in figure 5 (*a*). These nanoparticles are rather similar to particles which can be produced by arc-evaporation in a fullerene generator (e.g. Harris 1999), although in the latter case the particles usually contain many more layers. As in the Sigradur G carbon, there was some evidence for smaller fullerenes – a possible cluster of these can be seen to the left of the hexagonal particle in figure 5 (*a*). In addition to the closed particles, there were other features which were indicative of a fullerene-related structure. Re-entrant features were quite commonly seen, as in figure 5 (*b*). These structures are evidence for the presence of seven-membered rings, which produce negatively curved structures, or saddle-points (Iijima *et al*. 1992).

The presence of fullerene-like structures in the high-temperature carbons suggests that glassy carbons, like other non-graphitizing carbons, may have fullerene-related microstructures. As mentioned in the Introduction, the present author and colleagues have proposed a model for the structure of non-graphitizing carbons which consists of fragments of curved carbon sheets, containing pentagons and heptagons as well as hexagons (Harris and Tsang 1997). It seems likely that the low-temperature glassy carbons studied here may have structures like that shown in figure 6 (*a*). A distinguishing feature of glassy carbon, compared with some other non-graphitizing carbons, is low reactivity. This may result from a higher proportion of completely closed particles, or a more tightly packed microstructure, than in other carbons, making the material impermeable with lower reactivity. A model for the structure of high-temperature glassy carbon is shown in figure 6 (*b*). This can be thought of as mainly consisting of broken or imperfect fullerene-related nanoparticles, most of which are multilayered, enclosing pores which are much larger than in the low-temperature glassy carbons. The presence of seven-membered rings produces some saddle-points in the structure. A few completely closed nanoparticles will also be present.

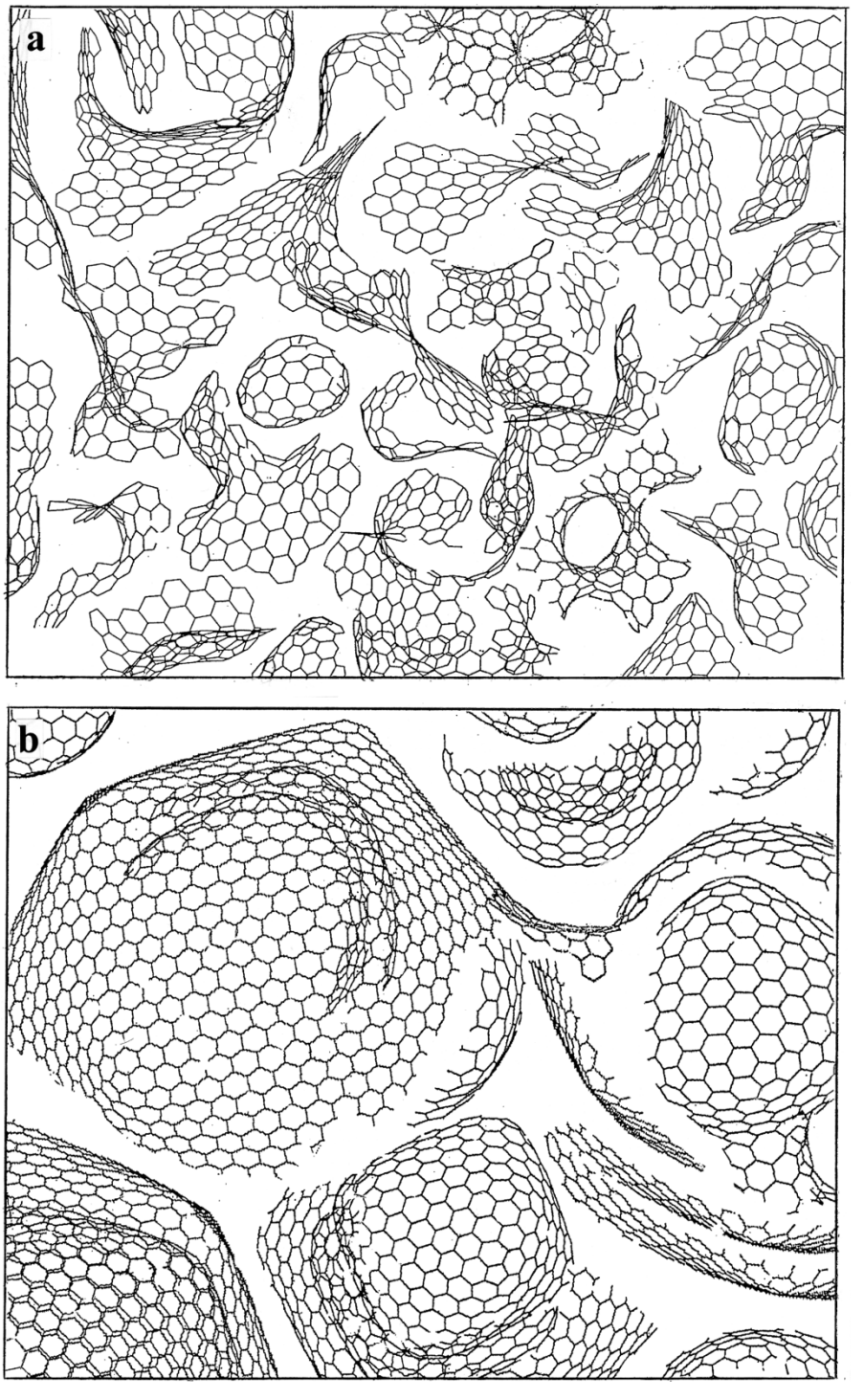

Figure 6. Models for the structure of (*a*) low-temperature and (*b*) high-temperature glassy carbon. These simulations were produced on a PC using the simple molecular modelling programme Desktop Molecular Modeller (Polyhedron Software Ltd.).

A model of heat-treated glassy carbon which also involves cage-like components was put forward by Shiraishi (1984). In this structure the particles are multilayered and have inner cavities approximately 5 nm in diameter. This model was put forward before the discovery of C_{60}, and the possibility that the cages might contain non-six-membered rings was not considered.

§ 4. Conclusions

The discovery of C_{60} prompted much speculation that well-known forms of carbon may have fullerene-related structures (Harris 2003). Initially, most of this speculation centred on spheroidal structures such as soot and carbon black particles. However, there are now good reasons to believe that fullerene-related structures may be present in other well-known carbon materials such as non-graphitizing carbon. In this paper, it has been shown that glassy carbons contain many features which are indicative of a fullerene-related structure. These include faceted structures, completely closed particles and negatively curved features. As a result of these observations, new fullerene-related models have been put forward for low-temperature and high-temperature glassy carbons. These appear to have significant advantages over earlier ideas about the structure of these carbons, such as those put forward by Jenkins and Kawamura. The fullerene-related models provide a more realistic explanation for the low reactivity, hardness and impermeability of glassy carbons. It should be stressed, however, that there is no *direct* proof that glassy carbons contain pentagonal rings, and achieving such evidence will not be easy. Diffraction methods do not provide unequivocal evidence that pentagons or other non-hexagonal rings are present. In principle, modern high-resolution transmission electron microscopes should be capable of imaging individual pentagonal rings, but this would be pushing their capability to the limits. Recent work by Colliex and colleagues has suggested that electron energy loss spectroscopy might be capable of detecting individual pentagons (Stephan *et al*. 2002), but as yet there is no clear evidence for this. The apparent presence of small fullerenes in some of the carbons suggests that it may be possible to extract C_{60} from commercial glassy carbons: this would provide strong evidence that the carbons have a fullerene-related structure. It is also worth mentioning interesting work by Gogotsi *et al*. (2000), which has shown that that Toyo Tanso glassy carbon can contain polyhedral graphite crystals, some of which resemble giant nanotubes. Such crystals were not seen in the present study, but their presence in glassy carbon is a further indication that it may have a fullerene-like structure.

Despite the progress which is being made in understanding their structure, there remain many unanswered questions about glassy carbons. In particular, it would be of great interest to know more about the mechanism whereby 'low-temperature' glassy carbon is transferred into the 'high-temperature' structure. The high-temperature carbons appear to have many fewer pentagons and other non-six-membered rings than the low-temperature carbons. Thus, during heat treatment, some pentagons must be converted into hexagons, or destroyed, while others migrate to the vertices of nanoparticle-like structures. The mechanism of pentagon migration may involve the Stone–Wales rearrangement (Stone and Wales 1986), which has been invoked to explain fullerene isomerization, but more work on the mechanisms whereby pentagons and other non-hexagonal rings can migrate is needed. It is also interesting to note that the pore sizes in the glassy carbons do not grow continuously with increasing heat treatment, but reach a constant size of approximately 5–10 nm, suggesting that fullerene-related nanostructures of this size range may have

a special stability. This is another area where more theoretical work would be of value.

Acknowledgement

The author is grateful to Rainer Dübgen and Norio Iwashita for supplying samples of glassy carbon and for helpful comments.

References

Burian, A., and Dore, J. C., 2000, *Acta Phys. Polon.*, A, **98**, 457.
Burian, A., Szczygielska, A., Koloczek, J., Dore, J. C., Honkimaki, V., and Duber, S., 2002, *Acta Phys. Polon.*, A, **101**, 751.
Ergun, S., and Tiensuu, V. H., 1959, *Nature*, **183**, 1668.
Franklin, R. E., 1951, *Proc. Roy. Soc.*, A, **209**, 196.
Gogotsi, Y., Libera, J. A., Kalashnikov. N., and Yoshimura, M., 2000, *Science*, **290**, 317.
Harris, P. J. F., 1997, *Int. Mater. Rev.*, **42**, 206.
Harris, P. J. F., and Tsang, S. C., 1997, *Phil. Mag.*, A, **76**, 667.
Harris, P. J. F., 1999, *Carbon Nanotubes and Related Structures* (Cambridge: Cambridge University Press), p. 102.
Harris, P. J. F., Burian, A., and Duber, S., 2000, *Phil. Mag. Lett.*, **80**, 381.
Harris, P. J. F., 2003, *Chemistry and Physics of Carbon*, Vol. 28, edited by L. R. Radovic (New York: Marcel Dekker), p. 1.
Iijima, S., 1991, *Nature*, **354**, 56.
Iijima, S., Ichihashi, T., and Ando, Y., 1992, *Nature*, **356**, 776.
Iwashita, N., Field, J. S., and Swain, N. V., 2002, *Phil. Mag.*, A, **82**,1873.
Jenkins, G. M., and Kawamura, K., 1971, *Nature*, **231**, 175; 1976, *Polymeric Carbons – Carbon Fibre, Glass and Char* (Cambridge: Cambridge University Press).
Jenkins, G. M., Kawamura, K., and Ban, L. L., 1972, *Proc. Roy. Soc.*, A, **327**, 501.
Kroto, H. W., Heath, J. R., O'Brien, S. C., Curl, R. F., and Smalley, R. E., 1985, *Nature*, **318**, 162.
Krätschmer, W., Lamb, L. D., Fostiropoulos, K., and Huffman, D. R., 1990, *Nature*, **347**, 354.
Mildner, D. F. R., and Carpenter, J. M., 1982, *J. non-crystalline Solids*, **47**, 391.
Pesin, L. A., 2002, *J. Mater. Sci.*, **37**, 1.
Pesin, L. A., and Baitinger, E. M., 2002, *Carbon*, **40**, 295.
Shiraishi, M., 1984, *Introduction to Carbon Materials* (in Japanese) (Tokyo: Carbon Society of Japan).
Stephan, O., Taverna, D., Kociak, M., Suenaga, K., Henrard, L., and Colliex, C., 2002, *Phys. Rev.*, B, **66**, 155422.
Stone, A. J., and Wales, D. J., 1986, *Chem. Phys. Lett.*, **128**, 501.

PHILOSOPHICAL MAGAZINE

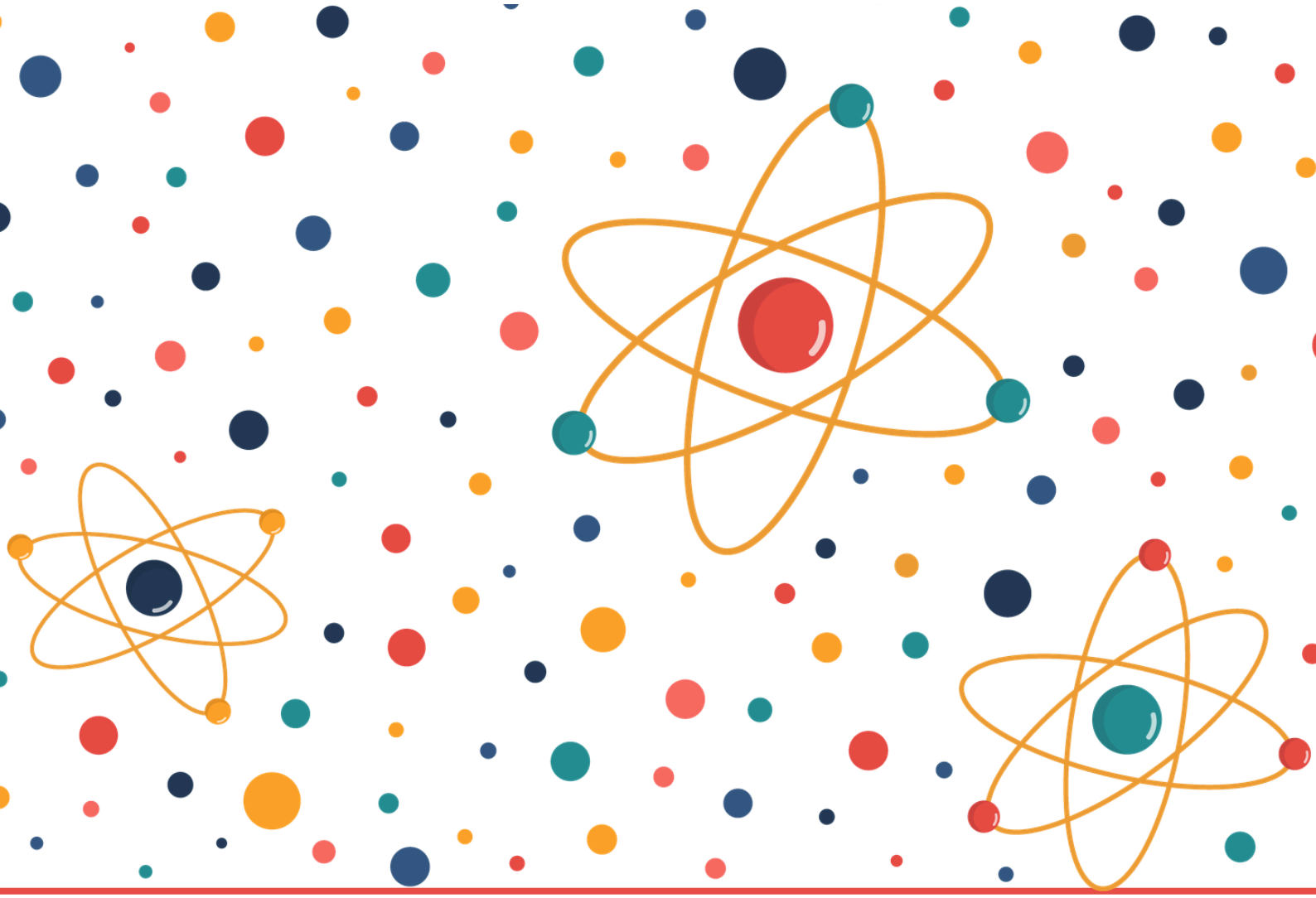

Contact us

Editorial Department | digitaleditor@philosophicalmagazine.com

Taylor & Francis
by informa